Off-the-Shelf Vision Based Mobile Robot sensing

A Dissertation
Presented to
the Graduate School of
Clemson University

In Partial Fulfillment
of the Requirements for the Degree
Doctor of Philosophy
Electrical Engineering

by
Zhichao Chen
August 2010

Abstract

The goal of this research is to enable a mobile robot using vision sensing technology to navigate in both outdoor and indoor environments, following such as a specified path, following a specified person, and detecting doorways to enter a room. The focus is upon real-time algorithm using off-the-shelf cameras.

First, a simple approach for vision-based path following for a mobile robot is presented. Based upon a novel concept called the *funnel lane*, the coordinates of feature points during the replay phase are compared with those obtained during the teaching phase in order to determine the turning direction. The system requires a single off-the-shelf, forward-looking camera with no calibration (either external or internal, including lens distortion). The algorithm is qualitative in nature, requiring no map of the environment, no image Jacobian, no homography, no fundamental matrix, and no assumption about a flat ground plane.

Second, by fusing motion and stereo information, Binocular Sparse Feature Segmentation (BSFS) algorithm is proposed for vision-based person following with a mobile robot. BSFS uses Lucas-Kanade feature detection and matching in order to determine the location of the person in the image and thereby control the robot. Matching is performed between two images of a stereo pair, as well as between successive video frames. We use the Random Sample Consensus (RANSAC) scheme for segmenting the sparse disparity map and estimating the motion models of the person and background. This system is able to reliably follow a person in complex dynamic, cluttered environments in real time.

Third, a vision-based door detection algorithm is developed based on Adaboost and Data-Driven Markov Chain Monte Carlo (DDMCMC). Doors are important landmarks for indoor mobile robot navigation. Models of doors utilizing a variety of features, including color, texture, and intensity edges are presented. The Bayesian formulations are constructed and a Markov chain is designed to sample proposals. The features are combined using Adaboost to ensure optimal linear weighting. Doors are detected based on the idea of maximizing a posterior probability (MAP). Data-Driven techniques are used to compute importance proposal probabilities, which drive the Markov Chain dynamics and achieve speedup in comparison to the traditional jump diffusion methods.

Dedication

I would like to dedicate my dissertation to my beloved parents, Yanfang Chen and Xunquan Chen, who made all of this possible through the endless words of encouragement and undoubted confidence in me. Particularly, to my wife, Huibbin Liu, whose love, support, and inspiration have enlightened and entertained me throughout the course of this journey.

Acknowledgments

First I would most like to acknowledge and express my appreciation for the immeasurable support and guidance contributed by Dr. Stan Birchfield, my advisor, who guided me through hurdles, and provided constant support that made my journey completed lot easier than it would have been. His wit and humor brightened hours of fascinating discussion about computer vision and the nature of reality. He is a fabulous resource, always able to provide deep insight and sparkling ideas on researches.

Additionally, I also want to express my gratitude to Dr. Ian D. Walker, Dr. John N. Gowdy, and Dr. Damon L. Woodard, not only for their input in the preparation of this dissertation, but also for the many hours of quality instruction they have provided to me in my graduate studies leading up to this point.

I would like to thank all the members of the Birchfield group who directly and indirectly provided helpful discussion, and assistance. My thanks also go to the numerous individuals in ECE Department of Clemson University. Also I would like to thank all my friends at clemson supporting me all the time.

Finally, I gratefully acknowledge financial supports from the Ph.D. fellowship from the National Institute for Medical Informatics.

Table of Contents

List of Tables

List of Figures

Chapter 1

Introduction

Autonomous robot systems are designed to operate in uncertain, cluttered, highly dynamic environments. They are widely used in industrial, medical, domestic, and difficult to reach or hazardous environments. A robot has to perceive its surroundings in order to interact with it. A variety of sensors, including sonar, laser range finder, radar, and camera provide the perception capability. However, the sonar sensor suffers from wide beam problems and poor angular resolution. The laser and radar provide better resolution but are more expensive, and have difficulty detecting small or flat objects on the ground. Vision sensing is one of the most powerful perception mechanisms. It identifies and describes objects in the environment by extracting, characterizing, and interpreting information from images. It naturally mimic human vision and is able to give the information "what" and "where" most completely for the objects a robot is likely to encounter. Vision sensing and human-computer interfaces are largely developed for industrial process control, medical applications and robot navigation, environment monitoring, and rescue missions during the last decades because of the low cost, low power, passive nature, and rich capturing ability of camera sensors. For example, SmartPal V, a slim service robot designed by Yaskawa Electric

Corporation is able to assist human beings in daily life. Equipped with four cameras, it can measure location of objects by a vision recognition system, even knowing how to sort laundry by color and type or just wander around and keep things cleaned up on its own.

Currently, the major challenge to robot vision-based sensing is the ability to function autonomously, learning useful models of environmental features, recognizing environmental changes, and adapting the learned models in response to such changes [88]. For example, the changes in illumination can quickly yield a failure of the robot-vision program. And also real-time and robust object segmentation from cluttered environments are highly demanded.

1.1 Principal objectives and key contributions

The long term goal of our research is to develop a vision-based mobile robot system which can be used as a personal digital assistant in the both indoor and outdoor environments. As part of this goal, this dissertation focuses on three specific topics: path following, person following, and door detection, to support vision-based sensory processing for a mobile robotic toolkit.

1.1.1 Path following

Route-based knowledge, in which the spatial layout of an environment is recorded from the perspective of a ground-level observer, is an important component of human and animal navigation systems [83]. In this representation, navigating from one location to another involves comparing current visual inputs with a sequence of views captured along the path in a previous instance. Among the many applications that would benefit from such a capability are the following: Courier robots that need to deliver items from one office to another, perhaps in a different building [30]; delivery robots that transport parts from one machine to another in an industrial setting; robot tour guides that repeat the same general path each time [16]; and a team of robots that follow the path of a scout robot in a reconnaissance mission [26]. Furthermore, a solution to this problem would be useful for the general problem of navigating between two arbitrary locations in an environment by following a sequence of such paths.

A popular approach in recent years is visual servoing, in which the robot is controlled by comparing the current image with a reference image. Such an approach generally requires the camera to be calibrated, and even uncalibrated systems require lens distortion to be removed. Calibration is a time-consuming process, and re-calibration is often needed. Mis-calibration can occur at setup, or can result from a gradual or dramatic degradation (for example, when the cameras get banged up in the course of the robot moving on uneven terrain or when the focal length of the camera changes due to zooming). Uncalibrated systems are becoming increasingly important as robots are moved into unstructured environments. Alternative vision-based algorithms make strong assumptions about the environment or the sensor, such as a flat ground plane[54, 18, 19, 59, 39, 79], a man-made environment in which vertical straight lines are present[54, 50, 6, 39, 79], or an omnidirectional camera[3].

Our goal is to develop a mobile robot navigation system that uses a single, off-the-shelf camera and lens, with no prior calibration whatsoever. We demonstrate the robot's ability to follow a long distance (hundreds of meters) path autonomously, without requiring any modification of the environment. In this dissertation, we have developed a simple algorithm that enables a mobile robot to autonomously repeat the path that it encountered during the teaching run. Using a teach-replay approach, the robot is manually led along a desired path in a teaching phase, and then the robot

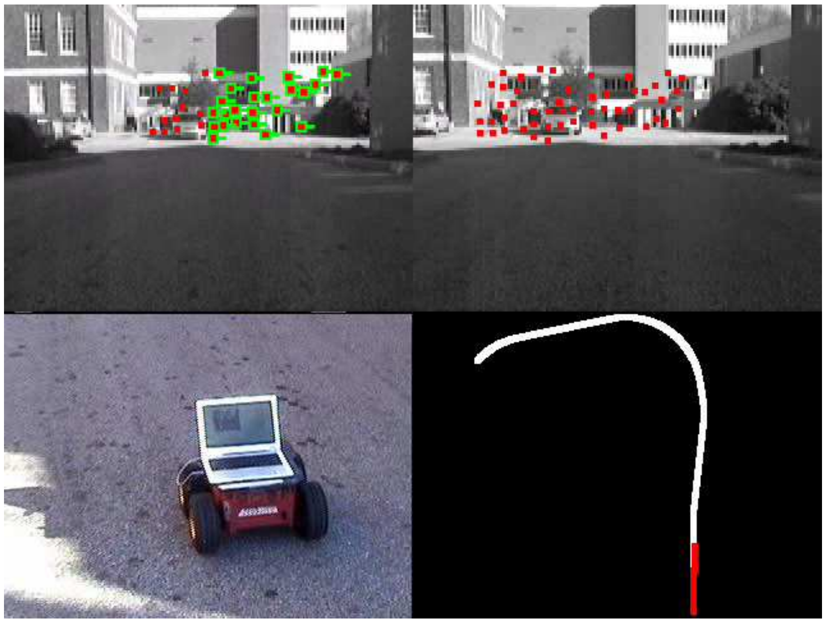

Figure 1.1: A typical example of path following. Top-left: The coordinates of feature points during the replay phase are compared with those obtained during the teaching phase in order to determine the turning direction. Top-right: Features obtained in the teaching phase. Bottom-left: The robot following a path. Bottom-left: Comparison of teaching and replay path.

autonomously follows that path in a replay phase. The coordinates of feature points during the replay phase are compared with those obtained during the teaching phase in order to determine the turning direction. Experimental results demonstrate the capability of autonomous navigation in both indoor and outdoor environments, on both flat and slanted surfaces, for distances over 200 meters. The technique requires a single off-the-shelf, forward-looking camera with no calibration (either external or internal, including lens distortion). The algorithm is entirely qualitative in nature, requiring no map of the environment, no image Jacobian, no homography, no fundamental matrix, and no assumption about a flat ground plane. A typical example is shown in Figure 1.1.

1.1.2 Person following

The ability to automatically follow a person is a key enabling technology for mobile robots to effectively interact with the surrounding world. Numerous applications would benefit from such a capability, including security robots that detect and follow intruders, interactive robots, and service robots that must follow a person to provide continual assistance [75, 86, 90]. In our lab, we are particularly interested in developing personal digital assistants for medical personnel in hospital environments, providing physicians with ready access to charts, supplies, and patient data. Another related application is that of automating time-and-motion studies for increasing the clinical efficiency in hospitals [9].

Tracking people from a mobile platform is one of the least developed and more difficult areas of machine vision. People are non-rigid objects and are difficult to model geometrically; plus, the occlusions and distractions from the environment, including other people, can confuse the tracker. And the foreground segmentation is more difficult from a moving platform than from a fixed viewpoint because the background undergoes motion relative to the platform, making static background subtraction is not applicable. To keep up with a walking person in real-time, the detection and tracking algorithm must be fast enough and require very quick focus of attention. The most popular approach utilizes appearance properties, such as color, that distinguish the target person from the surrounding environment. This method requires the person to wear clothes that have a different color from the background. In addition, lighting changes tend to cause serious problems for color-based techniques. Other researchers have applied optic flow to the problem. These techniques are subject to drift as the person moves about the environment, particularly with rotation, and are therefore limited to short paths.

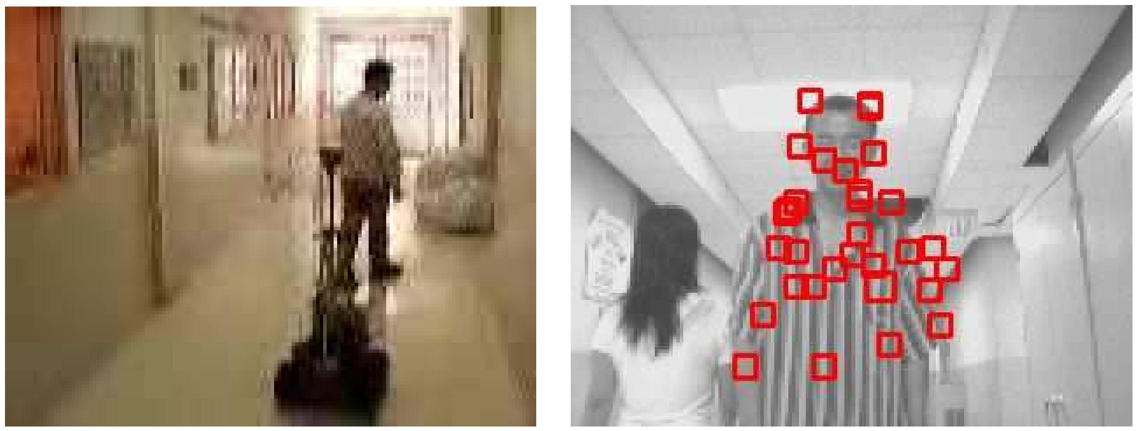

Figure 1.2: A typical example of person following. Left: A robot following a person. The person wears clothing with the same color as the environment. Right: Feature detection and matching in order to extract the person.

We have developed an algorithm using feature detection and matching in order to determine the location of the person in the image and thereby control the robot, as shown in Figure 1.2. Motion and stereo information is fused in order to handle difficult situations such as dynamic backgrounds and out-of-plane rotation. Unlike color-based approaches, the person is not required to wear clothing with a different color from the environment. Our system is able to reliably follow a person in complex dynamic, cluttered environments in real time.

1.1.3 Door detection

Doors are important landmarks for indoor mobile robot navigation. They mark the entrance/exit of rooms in many offices and laboratory environments. The ability of a robot to detect doors can be a key point for a robust navigation. However, there are still no fully operational systems that can operate robustly to detect doors in various environments.

Recognizing doors involves dealing with many factors that may affect the appearances of the objects: scale changes, perspective transformation of the door appearance in the image plane, lighting conditions, partial occlusion, other similar objects in the scene, etc. These factors make the door detection difficult. For examples, the color of the door might be the same as the wall; the floor might exhibit high reflection that severely distract the detector; the doors may be located in different geometrical positions and poses relative to the camera; and the drastic lighting changes may occur between the environment and the door.

Much of the previous work on door detection has relied upon 3D range information available from sonar, lasers, or stereo vision [47, 73, 89, 4]. We are interested, however, in using off-the-shelf cameras for detecting doors, primarily because of their low-cost, low-power, and passive sensing characteristics, in addition to the rich information they provide. Figure 1.3 illustrates our scenario, as well as the difficulties of solving this problem. The robot is equipped with two webcams, each one pointing at a different side of the hallway as the robot drives. Because there is no overlap between the cameras, stereo vision is not possible. Even more importantly, because the cameras are low to the ground, the top of the door (the *lintel*) — which otherwise would provide a powerful cue for aiding door detection — is often occluded by the top of the image. Pointing the cameras upward is not possible, because of the importance of being able to see the ground to avoid obstacles. Even with these constraints, our goal is to detect doors in a variety of environments, containing textured and untextured floors, walls and doors with similar colors, low-contrast edges, bright reflections, variable lighting conditions, and changing robot pose, as shown in Figure 1.3.

We present an algorithm to detect doors in images. The key to the algorithm's success is its fusion of multiple visual cues, including standard cues (color, texture, and intensity edges) as well as several novel ones (concavity, the kick plate, the vanishing point, and the intensity profile of the gap below the door). We use the Adaboost algorithm to ensure optimal linear weighting of the various cues. Formulated as a

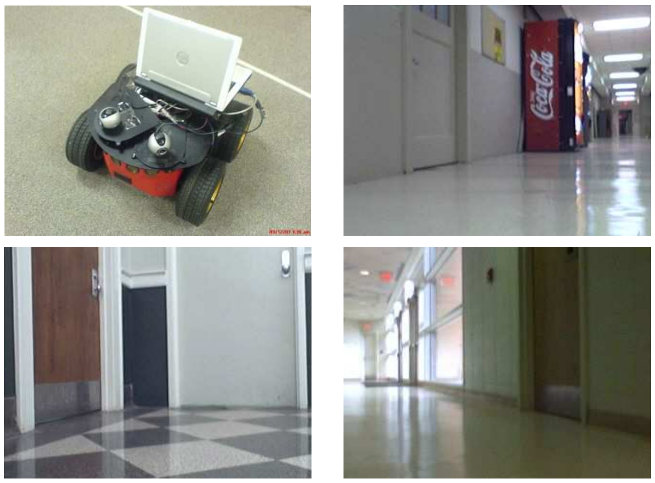

Figure 1.3: Doors in sample images. Top-left: Our robot is equipped with two non-overlapping off-the-shelf webcams, mounted on top (30 cm above the ground). Top-right: An image taken by one of the cameras, showing a door whose color is the same as the surrounding wall and whose lintel is not visible. Bottom: Two additional examples, showing doors at drastically different poses and colors, along with a variety of floor patterns and lighting conditions. These challenges make vision-based door detection difficult.

maximum a posteriori probability (MAP) problem, a multi-cue energy functional is minimized by a data-driven Markov Chain Monte Carlo (DDMCMC) process that arrives at a solution that is shown empirically to be near the global minimum. Intensity edge information is used in the importance probability distribution to drive the Markov chain dynamics in order to achieve a speedup of several orders of magnitude over traditional jump diffusion methods. Unlike previous approaches, the algorithm does not rely upon range information and yet is able to handle complex environments irrespective of camera pose, lighting conditions, wall or door color, and reflections. Moreover, the algorithm is designed to detect doors for which the lintel is occluded, which often occurs when the camera on a mobile robot is low to the ground. The versatility of the algorithm is demonstrated on a large database of images collected in a wide variety of conditions, on which it achieves greater than 90% detection rate with a low false positive rate. Versions of the algorithm are shown for open and closed doors, as well as for calibrated and uncalibrated camera systems. Additional experiments demonstrate the suitability of the algorithm for near-real-time applications using a mobile robot equipped with off-the-shelf cameras.

1.2 Application scenario

The research of this dissertation would benefit many applications, especially in the development of fully autonomous robots. In the future, the three algorithms presented could be integrated into a robot navigation system toward fully autonomous robot applications. For example, autonomous robot is highly desired in the hospital distribution service for decreasing operating costs while improving delivery performance. To meet the delivery needs of a hospital, any automated solution will need to handle routine deliveries as well as be flexible enough to handle arbitrary deliveries or other exceptions to the norm [76]. For routine pick-ups and deliveries, the robot follows a predefined route to deliver supplies to and from the service units. Beside routine deliveries, sometime the robot needs to deliver items to specific rooms. Therefore, door detection and recognition are required.[1] For arbitrary deliveries, the robot could follow a hospital staff to deliver emergent supplies anywhere as required.

1.3 Outline of dissertation

Following this introduction, the structure of this dissertation is a brief state of the art concerning related work on three specific topics in Chapter 2: path following, person following and door detection. Also discussed are some issues in their approaches. Then overviews of our approaches, and their advantages are described.

[1]Door recognition is not included in this dissertation.

This is followed by our qualitative vision-based path following algorithm, which is presented in Chapter 3; after that, the motion-based person following algorithm is presented in Chapter 4. Chapter 5 presents the door detection approach, including detecting both open and closed doors and tracking doors in videos. Chapters 3, 4 and 5 comprise a significant portion of the thesis. Once each algorithm is described, its applications to the mobile robot and the experimental results, and also the practical system limitations are given at the end of each Chapter. Finally, Chapter 6 presents some conclusions and suggestions for future work, along with a summary of the contributions of the dissertation.

Chapter 2

Related Work

In Chapter 1 we discussed general problems existing in vision-based mobile robot sensing regarding three topics: path following, person following, and door detection. This chapter reviews previous research in each of these three areas. The first section reviews previous research relevant to state-of-the-art path following approaches for long distance navigation in unstructured environments; particular emphasis is placed on the need for uncalibration systems. The second section reviews previous work on person following, that is, how to extract a person from a cluttered background and reliably track the person over time. In the third section a brief background of door detection is presented. The anatomy of the door is discussed along with visual cues suitable for detecting doors in images. Brief introductions of our solutions to existing problems are given at the end of each section.

2.1 Path following

Two questions that arise when addressing the path-following problem are the representation for the destination location and the choice of sensor. A traditional answer to the former question has been to build and maintain a global map of the environment, and to represent the destination as a point in that map [17, 52, 56, 101, 93, 94, 5]. While a global map is needed to compute the global location of the robot (particularly when its initial location is unknown), such a complicated approach may not be necessary to simply follow an incremental path to the destination [27]. Regarding the latter question, compared with other sensors vision is a promising option due to its low cost, low power consumption, and passive sensing [14]. Just as vision is a dominant sense in many biological systems, it is likely to become increasingly important in robotic systems.

An approach that has been gaining popularity in recent years is visual servoing, in which the robot is controlled by comparing the current image with a reference image, both taken by a camera on the robot [44, 22]. These techniques generally use a Jacobian that relates the coordinates of points in the world with their projected image coordinates [18]. Alternatively, some approaches utilize a homography or fundamental matrix to relate the coordinates between images [79, 59]. Vision-based algorithms usually make strong assumptions about the sensor or the environment, such as a calibrated camera (even uncalibrated systems often require some sort of calibration, such as removing lens distortion) [18, 6, 19], a flat ground plane [54, 18, 19, 59, 39, 79], or a man-made environment in which vertical straight lines [54, 50, 6, 39, 79] or the flat, parallel walls of a corridor are present [80]. Some systems require two or more cameras [52, 6, 85] or omnidirectional cameras [3], which are not as readily available as standard monocular cameras.

To some extent, map-based approaches using calibrated cameras have made significant progress in path following. Royer et al. [78] built a monocular vision mobile robot system, which probably is the one of the most successful approaches. The robot is equipped with a wide angle camera in a front looking position. A video sequence acquired in the learning step is processed off line to build a map of the environment with a structure-from-motion algorithm. Then the robot is able to follow the same path as in the learning step in real time. However, the camera has to be well calibrated and the ground is assumed locally planar and horizontal at the current position of the robot.

To overcome these limitations, we consider the problem from a novel viewpoint in which there is no equation relating image coordinates to world coordinates. Such a direct approach is motivated by the observation that the problem is vastly overdetermined, with tens of thousands of image pixels available to determine a single turning command output. In Chapter 3, we present a simple algorithm that uses a single, off-the-shelf camera attached to the front of the robot. The technique follows the teach-replay approach [18] in which the robot is manually led through the path once during a teaching phase and then follows the path autonomously during the replay phase. Without any camera calibration (even calibration for lens distortion), the robot is able to follow the path by making only qualitative comparisons between the feature coordinates in the two phases. All that is needed is a single controller gain parameter to convert pixel coordinates to turning angles. We demonstrate the technique on several indoor and outdoor experiments, showing its robustness with respect to slanted surfaces, changing lighting conditions, and dynamic occluding objects. This paper extends the applicability and improves upon the robustness of our earlier work [23] by incorporating odometry information and correcting for camera roll. We also demonstrate the ability of the technique to work with wide-angle and omnidirectional cameras, with only slight modification in the latter case to ignore the bottom half of the image which views the scene behind the robot.

The proposed approach falls within the category of mapless algorithms [27]. As such, it is closely related to the view-sequenced route representation (VSRR) of Matsumoto et al. [62, 63, 45] in which the turning angle is computed by cross-correlating images acquired during the replay phase with those captured during training. However, VSRR requires large amounts of memory to store the views and is sensitive to occlusions by dynamic objects. Along with a homography-based extension using vertical lines [79], it has only been demonstrated for short sequences on flat terrains.

An alternate mapless approach is to learn the mapping from images to turning commands based on their classification [99, 2]. While this method can successfully follow a specific pattern such as a road or hallway, it will have difficulty generalizing to environments in which the images cannot be categorized into a small number of classes known at training time. Another approach that has received considerable attention [37, 100, 102, 87, 51, 97, 43] is to store an example image with each specific location of interest. At run time, the image database is searched to find the image that most closely resembles the current one (or, alternatively, the current image is projected onto a manifold learned from the database [70, 53]). Such approaches require extensive training and have difficulty providing sufficient spatial resolution to determine actual turning commands in large environments. Similarly, sensory-motor learning has been used to map visual inputs to turning commands, but the resulting algorithms have been too computationally demanding for real-time performance [38]. Other researchers have developed mapless algorithms for low-level functionality like corridor following or obstacle avoidance [72, 80, 10, 57, 65, 69], but these techniques are not applicable to following a specific arbitrary path.

2.2 Person following

Existing approaches to vision-based person following can be classified into three categories. First, the most popular approach is to utilize appearance properties that distinguish the target person from the surrounding environment. For example, Sidenbladh et al. [86] segment the image using binary skin color classification to determine the pixels belonging to the face. Similarly, Tarokh and Ferrari [91] use the clothing color to segment the image, applying statistical tests to the resulting blobs to find the person. Schlegel et al. [81] combine color histograms with an edge-based module to improve robustness at the expense of greater computation. More recently, Kwon et al. [55] use color histograms to locate the person in two images, then triangulate to yield the distance. One limitation of these methods is the requirement that the person wear clothes that have a different color from the background. In addition, they are sensitive to illumination changes.

Other researchers have applied optical flow to the problem. An example of this approach is that of Piaggio et al. [75], in which the optical flow is thresholded to segment the person from the background by assuming that the person moves differently from the background. Chivilò et al. [36] use the optical flow in the center of the image to extract velocity information, which is viewed as a disturbance to be minimized by regularization. These techniques are subject to drift as the person moves about the environment, particularly with out-of-plane rotation, and are therefore limited to short paths.

As a third approach, Beymer and Konolige [11] use dense stereo matching to reconstruct a 2D plan view of the objects in the environment. Odometry information is applied to estimate the motion of the background relative to the robot, which is then used to perform background subtraction in the plan view. The person is detected as the object that remains after the segmentation, and a Kalman filter is applied to maintain the location of the person. One of the complications arising from background subtraction is the difficulty of predicting the movement of the robot due to uneven surfaces, slippage in the wheels, and the lack of synchronization between encoders and cameras.

In Chapter 4 an approach based upon matching sparse Lucas-Kanade features [84, 95] in a binocular stereo system is presented. The algorithm, which we call Binocular Sparse Feature Segmentation (BSFS), involves detecting and matching feature points both between the stereo pair of images and between successive images of the video sequence. Random Sample Consensus (RANSAC) [32] is applied to the matched points in order to estimate the motion model of the static background. Stereo and motion information are fused in a novel manner in order to segment the independently moving objects from the static background by assuming continuity of depth and motion from the previous frame. The underlying assumption of the BSFS algorithm is modest, namely, that the disparity of the features on the person should not change drastically between successive frames.

Because the entire technique uses only gray-level information and does not attempt to reconstruct a geometric model of the environment, it does not require the person to wear a distinct color from the background, and it is robust to having other moving objects in the scene. Another advantage of using sparse features is that the stereo system does not need to be calibrated, either internally or externally. The algorithm has been tested in cluttered environments in difficult scenarios such as out-of-plane rotation, multiple moving objects, and similar disparity and motion between the person and the background.

2.3 Door Detection

Some researchers have developed door detection systems using only range information, without cameras. Early work involved sonar sensors [74], while more recent work utilizes laser range finders [8, 64]. In all of these approaches, the detector requires the door plane to be distinguishable from the wall plane either because the door is recessed, a molding protrudes around the door, or the door is slightly open. Thus, if a door is completely flush with the wall, such detectors will be unable to find it.

Perhaps the most popular approach to door detection involves combining range sensors with vision. Kim and Nevatia [47] extract both vertical (post) and horizontal (lintel) line segments from an image, then analyze whether these segments meet minimum length and height restrictions, verifying door candidates by a 3D trinocular stereo system. Stoeter et al. [89] extract vertical lines in the image using the Sobel edge detector followed by morphological noise removing, then combine the resulting lines with range information from a ring of sonars to detect doors. In contrast, the system of Anguelov et al. [4] does not use intensity edges at all but rather the colors along a single scan of an omnidirectional image combined with a laser range finder. Doors are first detected by observing their motion over time (i.e., whether an open door later becomes closed, or vice versa) in order to learn a global mean door color. Doors are then detected in an expectation-maximization framework by combining the motion information with the door width (as estimated by the laser range finder) and the similarity of image data to the learned door color. This approach assumes that the doors are all similarly colored, and that the mean color of the doors and walls are significantly different from each other. Another piece of interesting research is that of Hensler et al. [42], who augment our recent vision-only algorithm [24] with a laser range finder to estimate the concavity and width of the door, which are then combined with other image-based features.

A few researchers have focused upon the much more difficult problem of detecting doors using vision alone, without range information. Monasterio et al. [67] detect intensity edges corresponding to the posts and then classify the scene as a door if the column between the edges is wider than a certain number of pixels, an approach that assumes a particular orientation and distance of the robot to the door. Similarly, Munoz-Salinas et al. [68] apply fuzzy logic to establish the membership degree of an intensity pattern in a fuzzy set using horizontal and vertical line segments. Rous et al. [77] generate a convex polygonal grid based on extracted lines, and they define doors as two vertical edges that intersect the floor and extend above the center of the image. Their work employs mean color information to segment the floor, thus assuming that the floor is not textured. An alternate approach by Cicirelli et al. [25] analyzes every pixel in the image using two neural networks: one to detect the door corners, and one to detect the door frame, both of which are applied to the hue and saturation color channels of the image.

While these previous systems have achieved some success, no vision-only system has yet demonstrated the capability of handling a variety of challenging environmental conditions (changing pose, similarly colored doors and walls, strong reflections, and so forth) in the presence of the lintel-occlusion that often occurs when the camera is low to the ground and the door is nearby.

In Chapter 5 we present a solution to the problem based upon combining multiple cues. Our approach augments standard features such as color, texture, and vertical intensity edges with novel geometric features such as the concavity of the door and the gap below the bottom door edge. The approach builds on our previous research [24] by incorporating these features into a maximum a posteriori (MAP) framework. Adaboost [33] is used to compute the optimal linear weighting of the different features, and a Data Driven Markov Chain Monte Carlo (DDMCMC) technique is used to explore the solution space. By incorporating intensity edges in the importance proposal distribution, a significant speedup is achieved in comparison to the traditional jump diffusion methods. We also present variations of the algorithm for detecting open as well as closed doors, and for working with calibrated as well as uncalibrated camera systems. Experimental results on a large database of images show the versatility of the algorithm in detecting doors in a variety of challenging environmental conditions, achieving a nearly global optimal solution in many cases. We also incorporate the algorithm into a real-time system that detects doors as the robot drives down a corridor.

Chapter 3

Path Following

Visual path following is a method that a robot can autonomously repeat a previous path to a given location. Cartwright and Collett [21] believe that the path following behavior can be achieved without a topographical map. They propose a "snapshot" model, which is designed to explain how a bee might return to a goal using a two-dimensional "snapshot" of the landscape seen from the goal. To guide its return, the bee continuously compares its snapshot with its current retinal image and moves so as to reduce the discrepancy between the two. Bees can only be guided in the right direction by the difference between current retinal image and snapshot when there is some resemblance between the two.

As Burschka and Hager [18] insightfully point out, the problem of following a predetermined path may not require a complicated approach. Intuitively, the vastly overdetermined nature of the problem (thousands of pixels in an image versus one turning command output) would seem to indicate that a simple method might be feasible. In this chapter we present a simple qualitative path following algorithm relying on visual tracking of features (landmarks). The technique follows the teach-replay approach [18] in which the robot is manually led through the path once during a teaching phase and then follows the path autonomously during the replay phase. Without any camera calibration (even calibration for lens distortion), the robot is able to follow the path by making only qualitative comparisons between the feature coordinates in the two phases.

Section 3.1 presents the qualitative feature mapping method for path following, including a novel concept called the *funnel lane* and the control algorithm . Section 3.2 briefly introduces how to select and track features. Section 3.3 describes the detailed strategy of teach-and-replay using qualitative feature mapping. Experimental results including indoor and outdoor are given in Section 3.4. Finally, Section 3.5 presents the conclusions.

3.1 Qualitative mapping from feature coordinates to turning direction

Consider a mobile robot equipped with a camera whose optical axis is parallel to the heading direction of the robot. Suppose we wish to move the robot from location $C = (x_C, y_C, \theta_C)$ to a previously encountered location $D = (x_D, y_D, \theta_D)$, where (x_i, y_i) and θ_i are the position and orientation, respectively, in the xy plane, $i \in \{C, D\}$. The robot has access to a current image I_C, taken at C, and a destination image I_D, taken previously at the destination D. In this section we introduce a qualitative test on image feature coordinates that guides the robot toward the destination. We start with a simple observation. Suppose the robot views a fixed landmark in both images yielding image feature coordinates of u^C and u^D, as shown in Figure 3.1. The features are computed with respect to a coordinate system centered at the principal point (the intersection of the optical axis and the image plane), so that

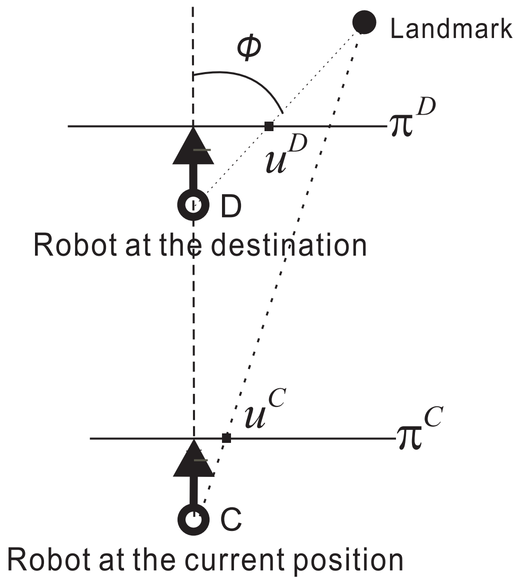

Figure 3.1: A fixed landmark. The robot is at C moving toward the destination D with the same heading direction. The open circle coincides with both the camera focal point and the robot position, the arrow indicates the heading direction, π is the image plane, and ϕ is the angle between the optical axis and the projection ray from the landmark.

positive coordinates are on the right side of the image while negative coordinates are on the left side. If the robot moves toward the destination in a straight line with the same heading direction as that of the destination (i.e., $\theta_C = \theta_D$), then the point u^C will move away from the principal point toward u^D, reaching u^D when the robot reaches D. This observation is made more precise in the following theorem.

Theorem 1 *Let a mobile robot move in a straight line toward location D on a flat surface. Let u^j be the horizontal image coordinate, relative to the principal point, of a monotonic projection at location j of a fixed landmark. For any location C along the line such that $\theta_C = \theta_D$, $\mid u^C \mid < \mid u^D \mid$ and sign$(u^C) =$ sign(u^D).*

The theorem can be easily proved by geometry. Note that perspective projection is only required to be monotonic (i.e., perspective projection is not necessary), so the result applies equally to a camera with radial lens distortion. Nevertheless, we will assume perspective projection throughout this section to simplify the presentation. Although the assumption of a flat surface is needed in theory, it has little effect in practice. A non-zero tilt angle has negligible effect on horizontal coordinates. We apply the random sample consensus (RANSAC) algorithm to compensate the roll angle and therefore align the the teaching images and the replay images.

3.1.1 The funnel lane

According to the preceding theorem, if the robot is on the path toward the destination with the same heading direction, then two constraints are satisfied. We call these the *funnel constraints*. Conversely, as shown in Figure 3.2, if the constraints are satisfied then the robot lies within a trapezoidal region for any given relative robot angle $\alpha = \theta_C - \theta_D$. For $\alpha = 0$ the sides of the trapezoid are defined by two lines passing through the landmark, one through D and another that is parallel to the destination direction. These lines are rotated about the landmark by α if the relative angle is nonzero. We call the trapezoidal region the *funnel lane* associated with the landmark, destination, and relative angle. The terminology arises from the analogy of pouring liquid into a funnel: The liquid moves in a straight line until it hits the sides of the funnel, which cause it to bounce back and forth until it eventually reaches the spout. In a similar manner, the sides of the trapezoid act as bumpers, guiding the robot toward the goal. The notion of the funnel and the funnel lane are captured in the following definitions.

Definition 1 *The* funnel *of a fixed landmark λ and a robot location D is the set of locations $\mathcal{F}_{\lambda,D}$ such that, for each $C \in \mathcal{F}_{\lambda,D}$, the two funnel constraints are satisfied:*

$$|\ u^C\ | \ < \ |\ u^D\ | \qquad \textit{(Constraint 1)}$$

$$sign(u^C) \;=\; sign(u^D) \qquad \textit{(Constraint 2)}$$

where u^C *and* u^D *are the coordinates of the image projection of* λ *at the locations* C *and* D*, respectively.*

Definition 2 *The* funnel lane *of a fixed landmark* λ*, a robot location* D*, and a relative angle* α *is the set of locations* $\mathcal{F}_{\lambda,D,\alpha} \subset \mathcal{F}_{\lambda,D}$ *such that* $\theta_C - \theta_D = \alpha$ *for each* $C \in \mathcal{F}_{\lambda,D,\alpha}$*.*

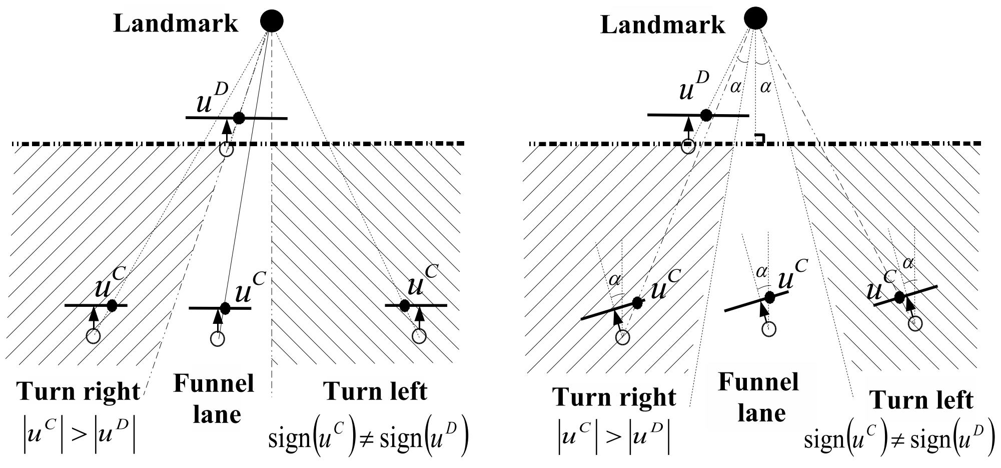

Figure 3.2: The funnel lane with a fixed landmark. The funnel lane created by the two constraints, shown when the robot is facing the correct direction (left) and when it has turned by an angle α (right).

Multiple features yield multiple funnel lanes, the intersection of which is the set of locations for which both constraints are satisfied for all the features. This intersection, which we call the *combined funnel lane*, is depicted in Figure 3.3. Notice the importance of having features on both sides of the image in order to narrowly constrain the path of the robot, thus achieving more robust and accurate results.

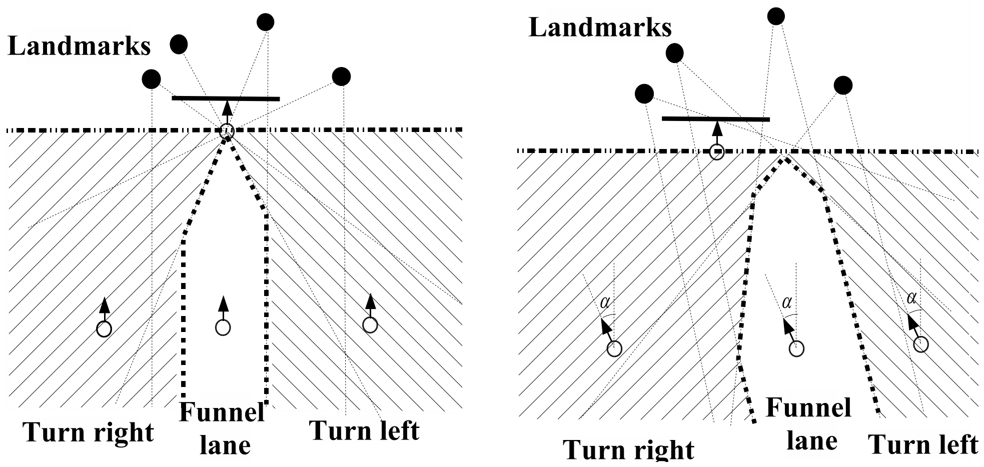

Figure 3.3: The combined funnel lane created by multiple landmarks. The combined funnel lane created by multiple feature points, shown when the robot is facing the correct direction (left) and when it has turned by an angle α (right).

3.1.2 Qualitative control algorithm

The funnel constraints lead to a simple control algorithm, illustrated in Figure 3.4. The robot continually moves forward, turning to the right whenever Constraint 1 is violated and to the left whenever Constraint 2 is violated, given a feature on the right side of the image ($u^D > 0$). If the feature is on the left side ($u^D < 0$), then the directions are reversed.

For each feature i, a desired heading is obtained by

$$\theta_d^{(i)} = \begin{cases} \gamma \min\{u^C, \phi(u^C, u^D)\} & \text{if } u^C > 0 \text{ and } u^C > u^D \\ \gamma \max\{u^C, \phi(u^C, u^D)\} & \text{if } u^C < 0 \text{ and } u^C < u^D \\ 0 & \text{otherwise} \end{cases}$$

where $\phi(u^C, u^D) = \text{sgn}(u^C - u^D)\sqrt{\frac{1}{2}(u^C - u^D)^2}$ is the signed distance to the line $u^C = u^D$. Here we approximate the conversion of pixels to radians with a constant gain γ, but more involved mappings could be used.

At any given time, the desired heading of the robot is given by

$$\theta_d = \beta \frac{1}{N} \sum_{i=1}^{N} \theta_d^{(i)} + (1 - \beta)\theta_o, \tag{3.1}$$

where θ_o is the desired heading obtained by the corresponding odometry measurements in the teaching phase, and the factor $0 \leq \beta \leq 1$ determines the relative importance of visual measurements versus odometry measurements.

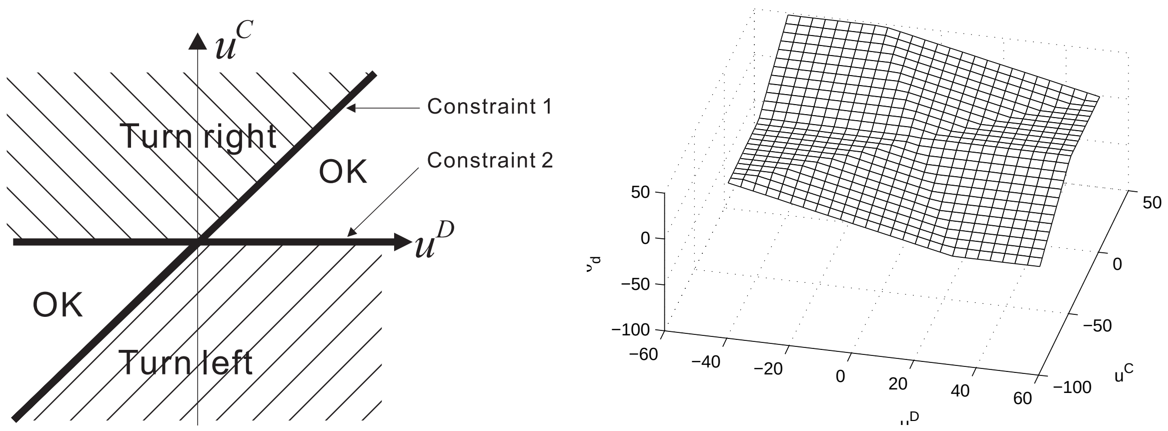

Figure 3.4: Qualitative control decision space. The coordinates of the feature point in the current and destination images (u^C and u^D, respectively) are compared to determine whether to turn the robot to the right, to the left, or not at all. LEFT: Top-down view of decision space. RIGHT: 3D view of decision space, showing the desired angle $\theta_d^{(i)}$ versus u^C and u^D.

3.1.3 Analysis of qualitative control algorithm

Figure 3.5 illustrates the qualitative approach with a simple example involving a single landmark. In its initial position the robot is outside the funnel lane, violating Constraint 1 (Figure 3.5a). The robot turns to the right, causing the funnel lane to rotate as well, and the robot moves forward a small amount until the constraint is violated again (Figure 3.5b). The robot turns a second time to the right, finds itself with a much clearer opening, and moves forward until the constraint is violated

(Figure 3.5c). Finally, the robot turns again and moves forward until it reaches a point close to the goal (Figure 3.5d).

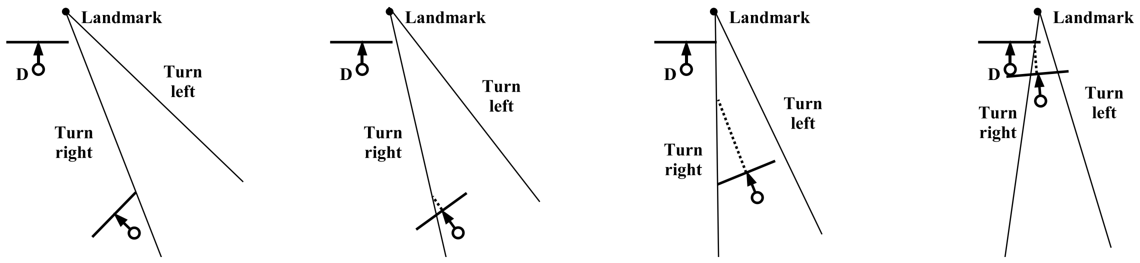

Figure 3.5: Snapshots of a robot making progress toward a destination. Four snapshots of a robot making progress toward a destination D using the qualitative control algorithm. The two solid lines indicate the funnel lane, while the dashed line indicates the path of the robot.

To better understand the behavior and accuracy of the approach, we ran simulations in Matlab. A single landmark was placed at the origin, and the robot was placed at various initial positions for different values of ϕ (the angle of the landmark with respect to the optical axis). From any initial position the robot may turn and drive straight toward the landmark, in which case it will barely satisfy Constraint 2. Alternatively it may turn away from the landmark and drive along a curve so that Constraint 1 is always barely satisfied. In both cases the other constraint is automatically satisfied. This line and curve define a region of positions, shown as gray in Figure 3.6, that are reachable from the initial position by a non-holonomic vehicle without violating either constraint. Notice that the actual location of the destination along the projection ray is irrelevant for the plots, which depend only upon the starting location, the landmark location, and the angle ϕ that the light ray makes with respect to the destination optical axis. The reachable set is wider for increasing values of ϕ.

Figure 3.7 displays the data in a different format, showing the minimum and maximum error in reaching the goal from various initial positions. With the landmark

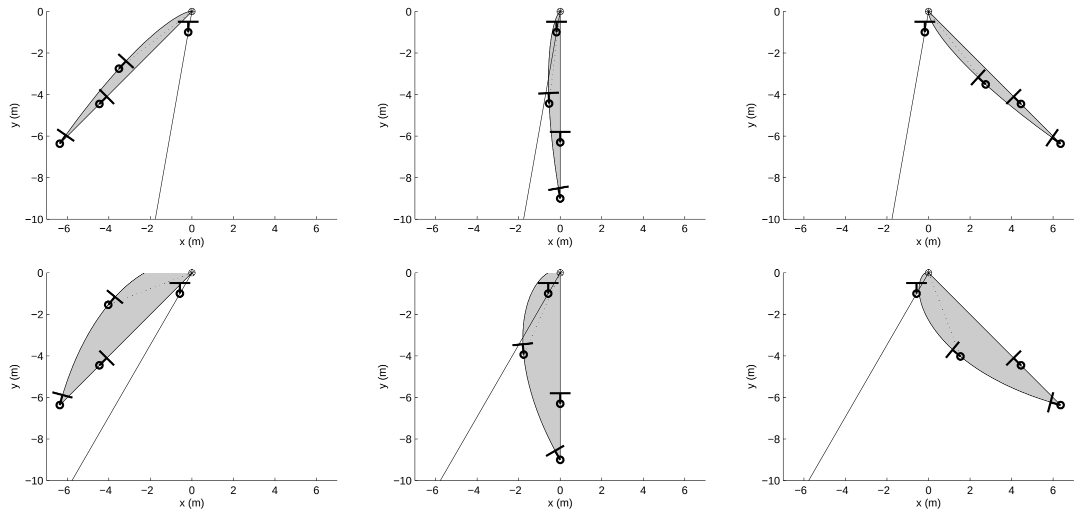

Figure 3.6: The reachable set of positions (gray region) from three different initial positions (left, middle, and right) and two different values of ϕ (top: 10 degrees, bottom: 30 degrees). The landmark is at $(0, 0)$, the initial position of the robot is at the bottom tip of the gray region, and the projection ray from the landmark to the destination is the angled line. Two possible robot locations along edges of the reachable set are shown, along with a possible location for the destination.

still at the origin, we placed the destination at the intersection of the line $y = -1$ m with the projection ray from the landmark at a given ϕ. The set of possible initial locations was densely sampled in order to generate contour plots of the error, as shown. The error was computed as the distance from the robot to the destination when the robot crossed the line $y = -1$ m. As can be seen, the probability of reaching the destination with zero error increases with larger values of ϕ, but the probability of large errors increases as well. As long as the robot starts from a position nearly behind the destination at a reasonable distance, the minimum error is zero and the maximum error is approximately 20-50% of the distance from the destination to the landmark. Keep in mind that these results were obtained for a single landmark; in a real system the use of multiple landmarks dramatically reduces this error.

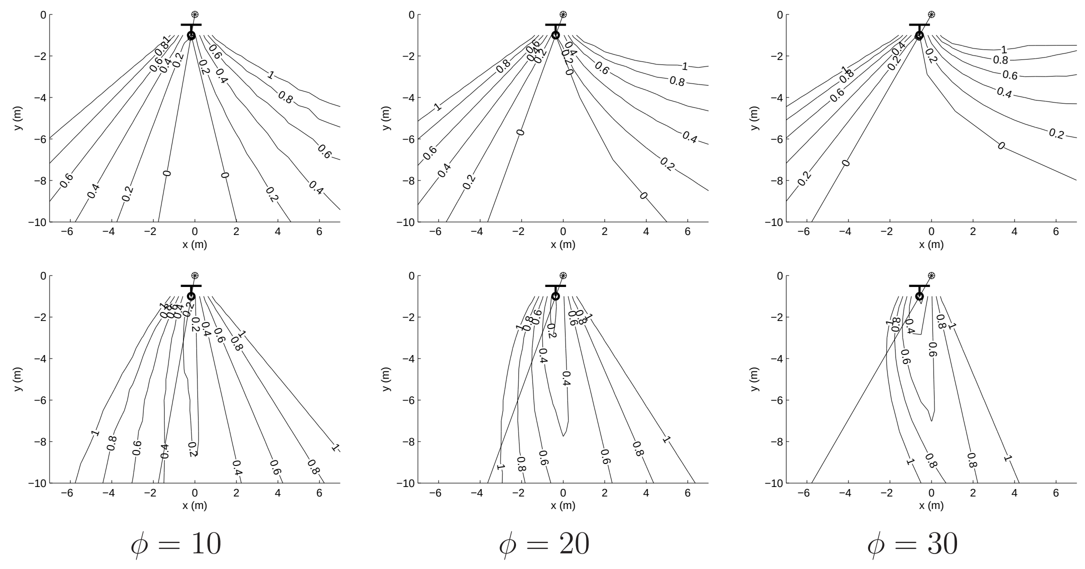

Figure 3.7: Contour plots of the minimum (top) and maximum (bottom) error in reaching a destination from any point in the plane. The destination is 1 m behind the landmark, which is placed at the origin. To reduce clutter, contours with a value greater than 1.0 are not shown. The curves labeled 0 enclose the region of zero error.

3.2 Tracking feature points

Feature points are automatically selected and tracked using the Kanade-Lucas-Tomasi (KLT) feature tracker [12], which computes the displacement $\mathbf{d} = [\, d_x \quad d_y \,]^T$ that minimizes the sum of the squared differences between consecutive image frames I and J:

$$\iint_W \left[I(\mathbf{x} - \frac{\mathbf{d}}{2}) - J(\mathbf{x} + \frac{\mathbf{d}}{2}) \right]^2 d\,\mathbf{x},$$

where W is a window of pixels around the feature point and $\mathbf{x} = [\, x \quad y \,]^T$ is a pixel in the image. This nonlinear error is minimized by repeatedly solving its linearized version by Taylor series expansion:

$$\begin{aligned} Z &= \sum_{\mathbf{x} \in W} \mathbf{g}(\mathbf{x}) \mathbf{g}^T(\mathbf{x}), \\ \mathbf{e} &= \sum_{\mathbf{x} \in W} \mathbf{g}(\mathbf{x}) \left[I(\mathbf{x}) - J(\mathbf{x}) \right], \end{aligned}$$

where $\mathbf{g}(\mathbf{x}) = \frac{1}{2}\partial[I(\mathbf{x}) + \alpha J(\mathbf{x})]/\partial\mathbf{x}$ is the spatial gradient of the weighted average image. These equations are the standard Lucas-Kanade equations [61, 7, 84, 95] with geometric symmetry between the two images and an affine model of brightness to model the dynamic lighting conditions encountered by the mobile robot, particularly when moving outdoors [61, 71]. A coarse-to-fine pyramidal strategy is used to allow large image motions. As in [84, 95], features are automatically selected as those points in the image for which both eigenvalues of Z are greater than a specified minimum threshold. This feature selection mechanism is a slight variation of the Harris corner detector which has been shown to be effective for both its repeatability rate, information content, and theoretical properties [40, 82, 46, 60].

The tracking algorithm just described relies on the well-known *constant brightness assumption* [96] in which image intensities are constant over time. As a robot moves about a real environment, however, the lighting conditions often change from one location to another. This problem is particularly acute in outdoor scenes during daylight hours when the robot moves in and out of shadows or when the sun is occluded or disoccluded by clouds. In such scenarios the standard algorithm often loses feature points prematurely. We present a simple extension of the KLT algorithm to handle illumination changes.

The residue equation defined above is augmented with a relative gain α and bias β describing the illumination relationship between the two images:

$$\iint_W \left[I(\mathbf{x} - \frac{\mathbf{d}}{2}) - \left(\alpha J(\mathbf{x} + \frac{\mathbf{d}}{2}) + \beta \right) \right]^2 d\,\mathbf{x}.$$

Applying a Taylor series expansion as above yields similar equations:

$$Z = \sum_{\mathbf{x} \in W} \mathbf{g}(\mathbf{x})\mathbf{g}^T(\mathbf{x}),$$

$$\mathbf{e} = \sum_{\mathbf{x} \in W} \mathbf{g}(\mathbf{x}) \left[I(\mathbf{x}) - (\alpha J(\mathbf{x}) + \beta) \right],$$

where $\mathbf{g}(\mathbf{x}) = \frac{1}{2} \partial [I(\mathbf{x}) + \alpha J(\mathbf{x})] / \partial \mathbf{x}$.

The values α and β are computed separately for each window by solving the following two equations:

$$\begin{aligned} E(I) &= \alpha E(J) + \beta \\ E(I^2) &= \alpha^2 E(J^2), \end{aligned}$$

where $E(I)$ is the mean intensity of the pixels in the window and $E(I^2)$ is the mean squared intensity of the pixels in the window. Similarly for $E(J)$ and $E(J^2)$.

3.3 Teach-and-replay navigation

The navigation system involves two phases. In the teaching phase, an operator manually moves the robot along a desired path to gather training data. The path is divided into a number of non-overlapping segments defined by a constant amount of travel time between them. Within each segment, feature points are automatically detected in the first image and tracked throughout subsequent images. For each feature that is successfully tracked throughout a segment, its graylevel intensity pattern and x-coordinate in the first and last images of the segment are stored in a database for use in the replay phase. We also store the length of each segment and the change of heading direction of the robot in each segment by odometry, which are used in determining the segment transitions.

In the replay phase, the robot is manually placed in approximately the same initial location as that of the teaching phase, and the robot proceeds sequentially through the segments. At the beginning of each segment, the KLT algorithm is used to establish correspondence between feature points in the current image and those of the first teaching image of the segment. Then, as the feature points are tracked in the incoming images, their coordinates are compared with those of the milestone image (i.e., the last teaching image of the segment) in order to determine the turning direction for the robot.

When the robot runs on an unpaved rough terrain, it moves from side to side resulting in rotations in the image plane between the teaching and the replay images, which give rise to incorrect funnel lanes. We apply the random sample consensus (RANSAC) algorithm to align the teaching and replay images. We repeatedly pick two random features in the milestone image and corresponding features in the replay image and calculate the rotation angle, which is then applied to all the milestone features to record the number of inliers. This process is repeated several times, and the rotation model with the largest number of inliers is taken to be the rotation between the teaching images and replay images.

A crucial component of the technique is determining when to transition to a new segment. One approach would be to threshold the mean squared error of the coordinates between the current and the milestone feature points. As the robot approaches the milestone, this error should decrease. However, we have found it impossible to find a single threshold that works in all environments, due to the various sources of noise occurring in real video data. Instead, we rely on the fact that the mean squared error tends to decrease over time as the robot approaches the milestone, then increase afterward. Although this method works with visual data alone, we have found a significant improvement in reliability when combining visual features with odometric information. Because odometers are accurate along short distances, they provide a healthy complement to the visual sensor whose strength is in the global information that it provides. This global picture, in turn, complements the odometry readings that drift over time due to slippage in the wheels and integration errors. Thus, we continually monitor the value

$$\delta = \exp\left\{-\frac{\epsilon_f^2}{2\sigma_f^2}\right\}\exp\left\{-\frac{\epsilon_o^2}{2\sigma_o^2}\right\}\exp\left\{-\frac{\epsilon_h^2}{2\sigma_h^2}\right\} \tag{3.2}$$

which estimates the likelihood that the robot is at the end of the current segment. In this equation ϵ_f is the mean squared error of the feature coordinates between the current and milestone images; ϵ_o is the difference between the distance traveled in the current segment and the corresponding segment in the teaching phase, calculated by odometry; and ϵ_h is the difference between the current heading and the heading at the end of the teaching segment. These errors are normalized by values computed automatically by the system: σ_f is the mean squared error of the feature points at the beginning of the segment; σ_o is the length of the segment calculated by odometry in the teaching phase; and σ_h is the maximum variation in heading encountered during the teaching segment.

Due to the distraction from noise, δ might not decrease or increase monotonically. We monitor the changes of δ between 5 consecutive frames. In these 5 consecutive frames, if most δ increase, the algorithm transitions to the next milestone. At the same time, we also monitor δ changes in the previous segment and the next segment. δ should always increase in the previous segment and decrease in the next segment. Otherwise, the algorithm will transit back and forth.

3.4 Experimental results

The qualitative algorithm was implemented in Visual C++ on a Dell Inspiron 700m laptop (1.6 GHz) controlling an ActivMedia Pioneer P3-AT mobile robot with an inexpensive Logitech QuickCam Pro 4000 webcam mounted on the front. The 320×240 images were acquired at 30 Hz and processed by the KLT algorithm with the default 7×7 feature window size [12]. In all experiments a maximum of 60 features were detected and tracked throughout each segment. On average 85% of the features survive the initial correspondence in the first image of the segment during replay. The algorithm was tested in a number of indoor and outdoor environments.[1]

3.4.1 Indoor experiments

The algorithm was tested in an indoor environment, including our laboratory as well as a corridor of the hallway in our building. The maximum speed of the robot during the teaching phase was 100 mm/s and the turning speed was 4 degrees per second. Due to the small environment, the driving speed during the playback phase was reduced in order to avoid going off course. Figure 3.8 shows a typical run in which the robot successfully navigated between chairs and desks in our lab along a 10 m path. Trajectories displayed in the figure were computed by integrating the odometry readings (which are not used by the algorithm). The maximum error was 0.35 m (for 80% of the path the error was less than 0.2 m), and the final error was 0.03 m.

Figure 3.9 shows the decision process at two time instants during the replay phase. In one case the robot is pointing to the right of the current direction, so the features on the left half of the image violate either Constraint 1 or Constraint 2,

[1]Videos of the results can be found at
`http://www.ces.clemson.edu/~stb/research/mobile_robot`

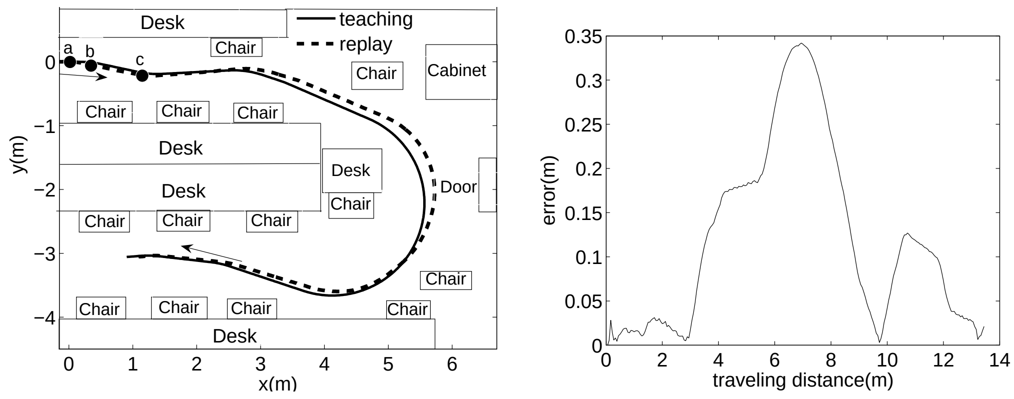

Figure 3.8: Indoor navigation. Top: The teaching and replay paths of the robot in an indoor environment (our laboratory). The locations `a`, `b`, and `c` are used in Figure 3.10. Bottom: Error versus distance traveled.

thereby indicating the need for the robot to turn left. In the other case the features on the right half of the image violate one of the constraints, thereby indicating the need to turn right. In both cases notice the unanimity of the voting: Although many features simply plead ignorance, those features that do cast a vote are in agreement.

Figure 3.10 displays the decision process during three segments of the experiment. For display purposes, the feature coordinates are normalized so that the interval $y \in [0, 1]$ indicates "do not turn", while larger values ($y > 1$) indicate "turn right", and smaller values ($y < 0$) indicate "turn left", where y is defined as

$$y = \begin{cases} 1 + u_i^t / \left| u_i^d \right| & (u_i^d < 0) \\ u_i^t / \left| u_i^d \right| & (u_i^d > 0) \end{cases} . \tag{3.3}$$

Notice again the near unanimity in voting (a lone feature in (b) votes incorrectly to turn left). Also notice that, as the robot turns (in (b) and (c)) the features move toward the OK region.

Indoor environments present a particular challenge for feature point tracking because of the lack of texture on the walls. Occasionally the robot fails to remain on course due to lack of texture in the scene that causes feature points to be lost.

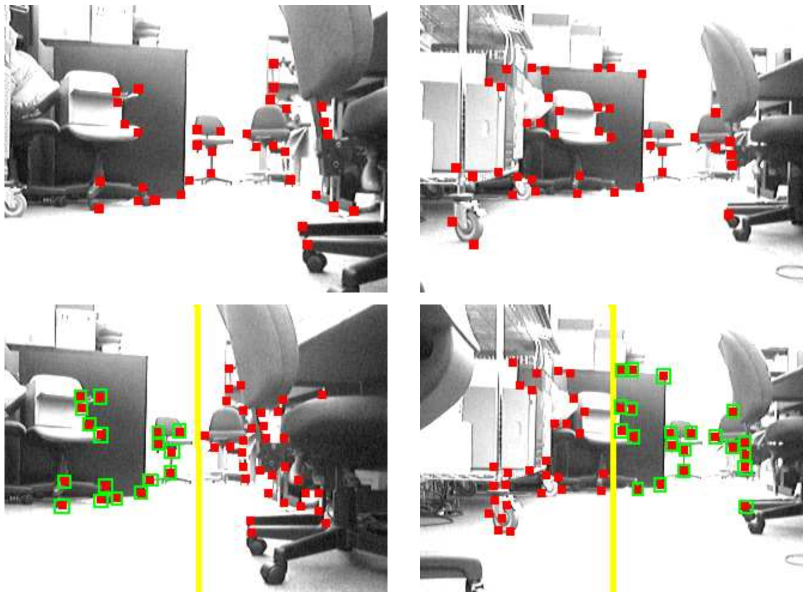

Figure 3.9: Feature decision process. Top: Two milestone images from the indoor experiment, with all the feature points overlaid. Bottom: Two current images within each segment, as the robot moves toward the corresponding milestone location, with feature points overlaid. The features outlined by a rectangle (green in the electronic version of the paper) are the ones for which one of the constraints is violated. In the left column, the features on the left half of the current image tell the robot to turn left. In the right column, the features on the right half of the current image tell the robot to turn right.

Difficulty is encountered primarily when the robot has to turn near the corner of a hallway containing no additional objects.

3.4.2 Outdoor experiments

Dozens of experiments were also conducted outdoors, with the robot driving along sidewalks and parking lots of a university campus. The additional maneuvering room enabled the driving and turning speeds to be increased to 750 mm/s (the maximum driving speed of the robot) and 6 degrees per second, respectively. Figure 3.11 show the results of a typical run in which the robot successfully followed a 140 m

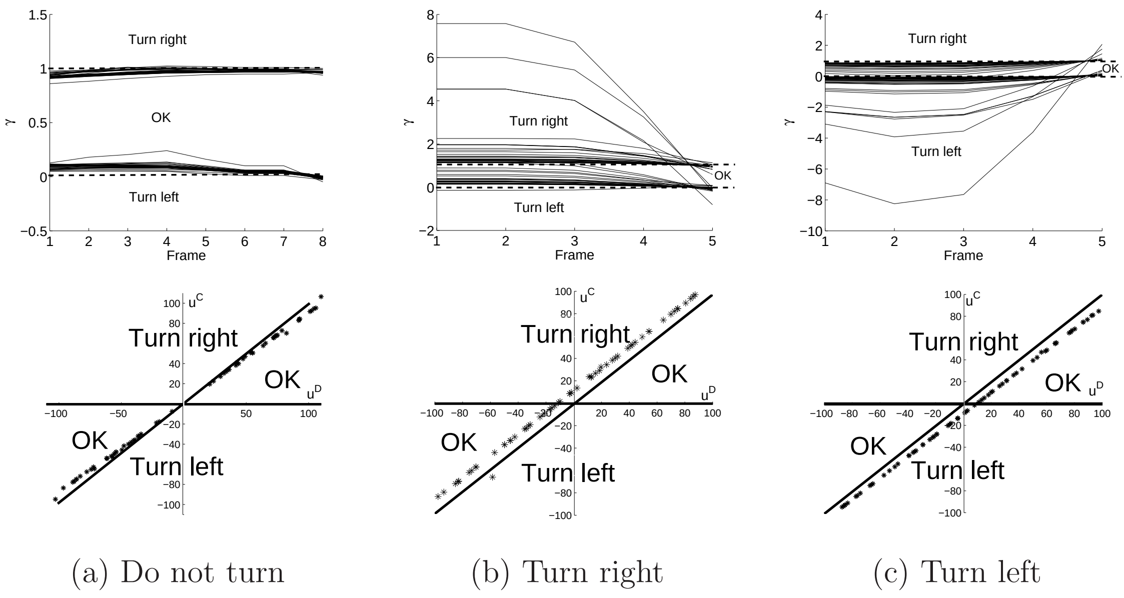

Figure 3.10: Features vs. direction. TOP: The normalized feature coordinates of all the features plotted versus the image frame number for three segments of the indoor experiment. Features below 0 vote for "turn left", while those above 1 vote for "turn right". BOTTOM: A snapshot of the features from frame 2 of each segment plotted on the qualitative control decision space to show the instantaneous decision. The three segments correspond to the points a, b, and c from Figure 3.8.

loop trajectory in a parking lot. The error was less than 1 m for two-thirds of the sequence and remained below 3.5 m for the entire sequence.

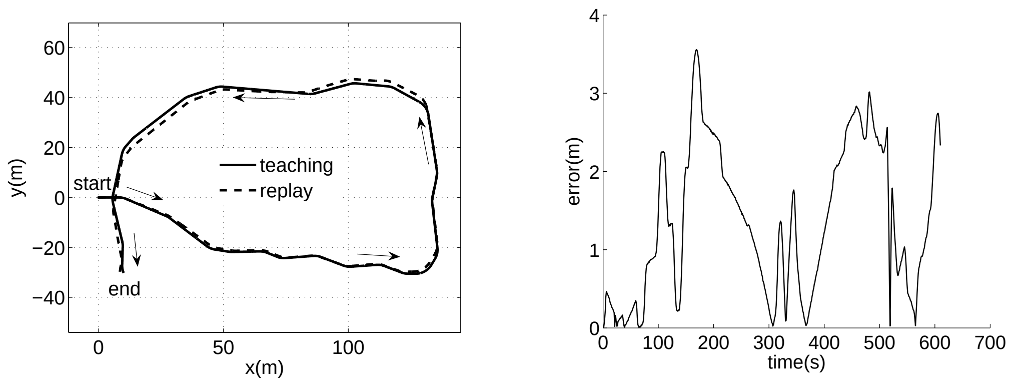

Figure 3.11: Outdoor navigation. TOP: The teaching and replay paths of the robot in an outdoor environment (parking lot). BOTTOM: Error versus distance traveled.

Figure 3.12 shows sample images from two experiments demonstrating the robustness of the algorithm. In the first, the robot navigated a slanted ramp in a 40 m run, thus verifying that the algorithm does not require a flat ground plane. In the second, the robot navigated a narrow road for 80 m while a pedestrian walked by the robot and later a van drove by it. Because the milestone images change frequently, the algorithm quickly recovered from the loss of features due to the occlusion caused by the dynamic objects.

When a dynamic object (e.g., a person walking) comes into the view of the robot, feature points on the background may be lost due to occlusion. Because the algorithm treats all the features equally and because a new milestone image (defined below) is taken frequently, this loss does not affect the performance of the algorithm in practice as long as the occlusion is fairly small (say, one-fourth of the image). If the occluding object is so large in the field of view that it causes a large number of feature points to be lost, then there is not enough information for the algorithm to continue. This problem can be solved by detecting the sudden loss of a large percentage of the features and commanding the robot to stop until it is able to reacquire the features once the object leaves the field of view.

A challenge of outdoor environments is the drastic change in illumination, which is caused primarily by either (1) changing environmental conditions over time, or (2) the automatic gain control of the camera adjusting to the difference between shadow and sunlight. Figure 3.13 shows the importance of the lighting-insensitive modification to the KLT feature tracking algorithm using two experiments. In the first, there was significant change in the environmental lighting between the teaching and replay phases due to changing cloud cover. In the second, the automatic gain control of the camera caused the overall brightness of the scene to change significantly because the robot moved from bright sunlight into a shadow. In both cases the original KLT algorithm lost nearly all the features while the modified algorithm successfully

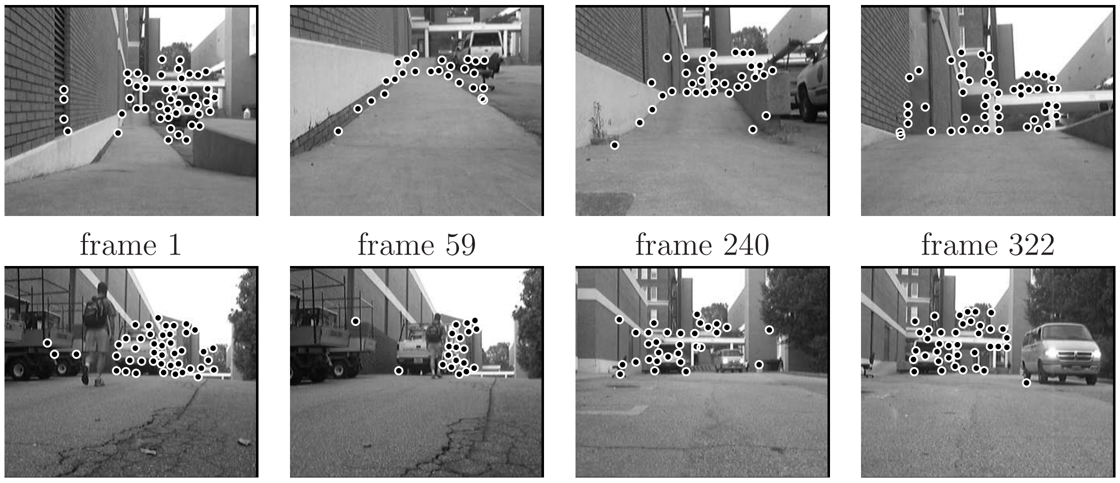

Figure 3.12: Running on the ramp with dynamic objects. Sample image frames from two different sequences, one in which the robot traveled down and up a ramp (top), and the other containing dynamic objects (bottom). The circles indicate the features.

tracked many of them.

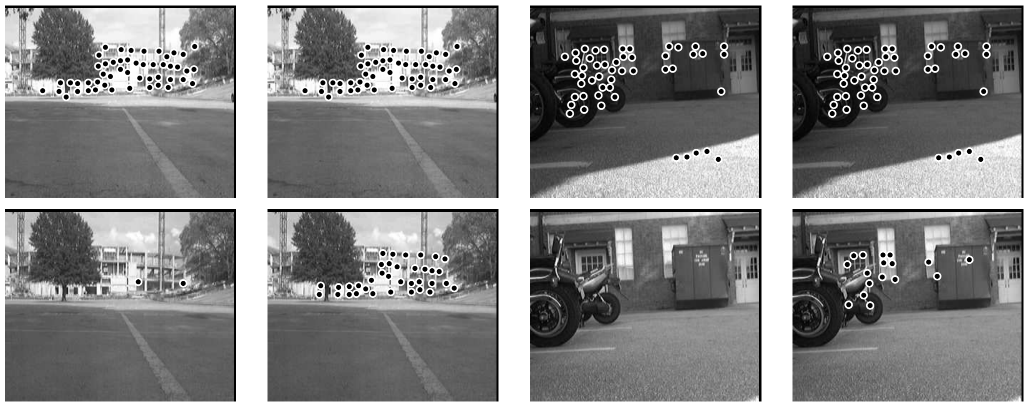

Figure 3.13: Results under changing lighting conditions. Left columns: Two images with features tracked using the original and modified KLT algorithms, with the sun being occluded by clouds. Right columns: Two images from a sequence in which the automatic gain control caused a brightening of the image as the robot moved from sun to shade.

3.4.3 Different cameras

Figure 3.14 shows the results of the approach using cameras with severe lens distortion. In one experiment we used a wide-angle camera with a 3.5 mm focal length and 110-degree field of view. The other experiment utilized an omnidirectional camera with a 360-degree field of view. For both experiments we used the same parameters as the previous experiments. The only change made to the code was to discard the bottom half of the omnidirectional donut image. This step was necessary because features behind the robot (whether viewed by an omnidirectional or standard camera) move in a way that violates the fundamental assumptions of our approach. In contrast, features in front of the camera obey the funnel constraints sufficiently to be of use in keeping the robot on the path, despite their moving in curved image paths due to the severe lens and catadioptric distortion. The average error of the two experiments was 0.04 m and 0.04 m, respectively, while the maximum error was 0.13 m and 0.09 m.

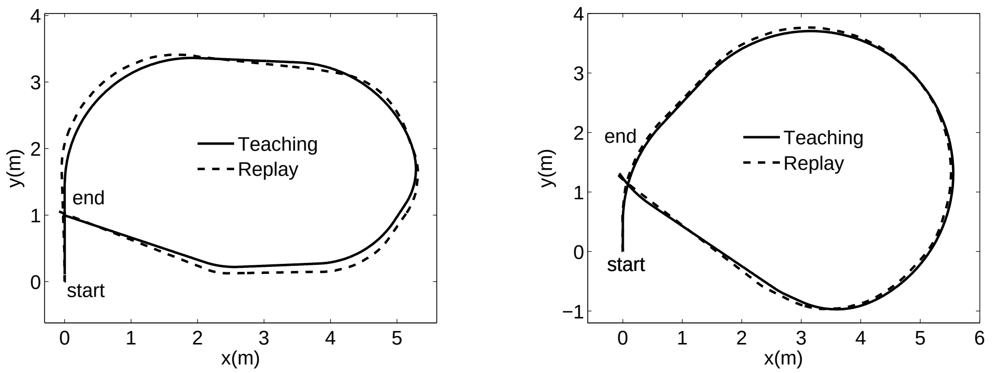

Figure 3.14: Using cameras with severe lens distortion. The approach successfully following a path using a wide-angle camera (left) and an omnidirectional camera (right).

To further illustrate the lack of calibration, we conducted an outdoor experiment in which the robot navigated the same 50 m path twice. In the first run the robot used the Logitech Quickcam Pro 4000 camera, while in the second run it used an Imaging Source DFK21F04 Firewire camera with an 8.0 mm F1.2 lens. The same camera was used for both teaching and replay. As shown in Figure 3.15, the algorithm was able to successfully follow the path using either camera, without changing any parameters between runs.

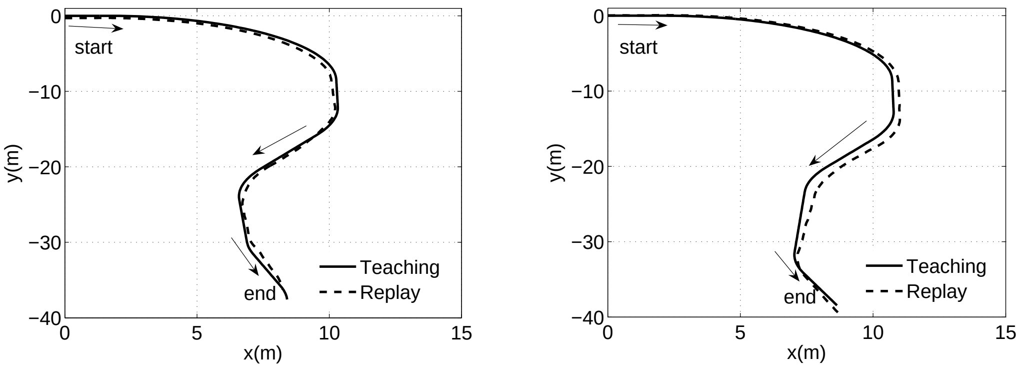

Figure 3.15: Using two different uncalibrated cameras. Teaching and replay paths for the robot using two different uncalibrated cameras, with the same system parameters. LEFT: Logitech QuickCam Pro 4000 USB webcam, RIGHT: Imaging Source DFK 21F04 Firewire camera.

Three additional experiments are shown in Figure 3.16. In the first, a scout robot was sent along an outdoor path. Another robot, which received the transmitted path information, was then able to follow the same path as the scout. This demonstrates a natural application to swarm robotics, where calibrating dozens or hundreds of cameras would be prohibitive, especially if recalibration is needed whenever the lenses are refocused or the cameras adjusted. The second experiment shows the robot following a path along rough terrain, in which roll and tilt angles up to 5 degrees were encountered. The roll angle compensation described earlier was sufficient to enable the robot to remain on the path. In the third, a path with several sharp turns is demonstrated. This ability is achieved by setting the replay driving speed to be that of the teaching driving speed, which is decreased during a turn.

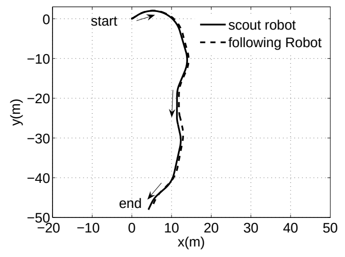

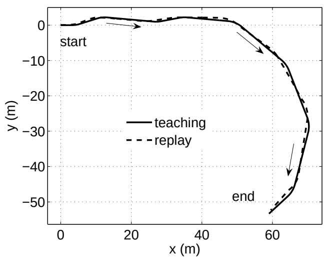

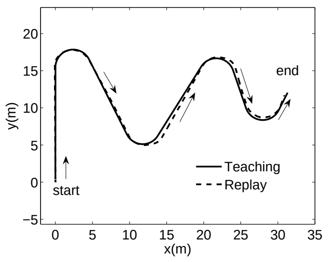

Figure 3.16: Applications for scout robot. LEFT: The robot followed a path taken earlier by a scout robot. MIDDLE: A path on rough terrain. RIGHT: A path with sharp turns.

3.4.4 Repeatability and accuracy

Additionally, the algorithm was tested in various scenarios to quantitatively measure its accuracy and repeatability. Table 3.1 displays the results of the algorithm compared with those of our earlier version [23] which did not use odometry, relied upon a bang-bang control scheme, and did not compensate for the camera roll angle. The algorithms were tested in three environments: a 15 m path in an indoor laboratory environment with rich texture for feature tracking, a 60 m trajectory in an outdoor paved parking lot, and a 40 m path along unpaved terrain. In each case, we conducted ten trials and recorded the final 2D location of the robot for each trial: $\{\mathbf{x}_i\}_{i=1}^n$, where $\mathbf{x}_i \in \mathbb{R}^2$ and $n = 10$. Accuracy was measured as the RMS Euclidean distance to the final ground truth location: $\sqrt{\frac{1}{n}\sum_{i=1}^n || \mathbf{x}_i - \mathbf{x}_{gt} ||^2}$. Repeatability was measured as the standard deviation of the final locations: $\sqrt{\frac{1}{n}\sum_{i=1}^n || \mathbf{x}_i - \mu ||^2}$, where $\mu = \frac{1}{n}\sum_{i=1}^n \mathbf{x}_i$. While the earlier algorithm works well when the ground is paved and the scenery is rich in texture, the improved algorithm is more robust, achieving maximum errors of only 0.23 m, 1.20 m, and 1.76 m, respectively, compared with 0.45 m, 1.20 m, and 5.68 m for the earlier algorithm.

The algorithm assumes that the robot is placed in the same initial location in both the teaching and replay phases. To test the sensitivity to this assumption,

Algorithm	indoor acc. / rep. (m) / (m)	outdoor paved ground acc. / rep. (m) / (m)	outdoor rough terrain acc. / rep. (m) / (m)
vision only [23]	0.30 / 0.18	0.77 / 0.74	3.87 / 1.85
combination (this thesis)	**0.14** / **0.08**	**0.60** / **0.55**	**1.47** / **0.66**

Table 3.1: Comparison of the accuracy and repeatability of the algorithm with an earlier version, in three different scenarios. The lowest number in each case is in bold.

we conducted an experiment with a fairly straight teaching path outdoors, with the background approximately 50 m from the initial location. The robot was then placed at different initial locations for the replay phase, deviating laterally from the initial teaching location by 0 m, 0.5 m, 1.0 m, and 2.0 m. To ensure overlap between the teaching and replay features, the initial robot orientation was adjusted by 0^o, 1^o, 2.5^o, 3.5^o, and 4.5^o, respectively. The results, shown in Figure 3.17a, show that the robot converges to the teaching path in all cases, reducing the error in half after approximately 20 m. With closer backgrounds, the convergence is faster. In a similar experiment, the robot was placed 0 m, 0.5 m, 1.0 m, 1.5 m, 2.0 m respectively, ahead and behind the initial teaching location. Figure 3.17b plots the deviation in the estimate of the position of the robot along the path versus the driving distance along the teaching path. Although these results exhibit more noise, the errors reduce over time, requiring about 6 m for convergence for locations in front, and approximately 20 m for locations behind.

3.5 Summary

A simple and efficient algorithm has been presented for enabling a mobile robot to follow a desired path using a single off-the-shelf camera. Following a teach-replay

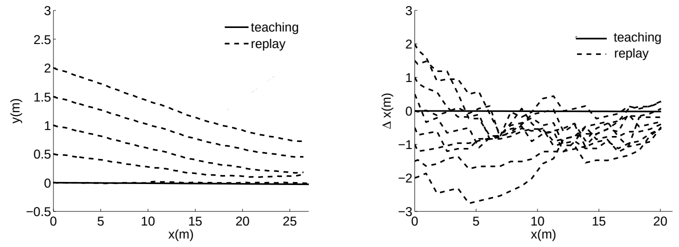

(a) (b)

Figure 3.17: Sensitivity to the initial location. (a) The replay path of the robot versus time, starting from different locations deviating laterally from the initial teaching location. (b) The deviation of the robot along the replay path versus time, starting from different deviations along the path from the initial teaching location.

approach, the robot navigates by performing a qualitative comparison of feature coordinates across the teaching and replay phases. Vision information is combined with odometry for increased robustness. As such, the algorithm does not make use of the traditional concepts of Jacobians, homographies, fundamental matrices, or the focus of expansion. It also does not require any calibration (even lens calibration). Experimental results on both indoor and outdoor scenes demonstrate the effectiveness of the approach on trajectories over 100 m, along with its robustness to effects such as dynamic objects and slanted surfaces. However, the limitation of this algorithm is obvious. Since the algorithm depends on comparing scenes between the teaching and replay phase, it would fail if the scene changes significantly after teaching. For example, the robot is taught in a parking lot with a lot of cars parking there in the morning. And it would fail to repeat the learned path in the afternoon because most cars are gone. Future work should be aimed at incorporating higher-level scene knowledge to have the robot focus on those unchanged landmarks, such as buildings, by applying scene segmentation algorithm.

Chapter 4

Person Following

Visual person following with a mobile robot is another important research topics in machine vision and robotics. New and innovative techniques are constantly being developed. However, despite the impressive results obtained, it is clear that no approach can perform reliably in all situations. People are non-rigid objects and are difficult to model geometrically; plus, the occlusions and distractions from the environment, including other people, can confuse the tracker. And the foreground segmentation is more difficult from a moving platform than from a fixed viewpoint because the background undergoes motion relative to the platform, and therefore the static background subtraction is not applicable. To keep up with a walking person in real-time, detection and tracking algorithm must be fast enough and require very quick focus of attention. The most popular approach utilizes appearance properties, such as color, that distinguish the target person from the surrounding environment. This method requires the person wear clothes that have a different color from the background. In addition, lighting changes tend to cause serious problems for color-based techniques. Other researchers have applied optic flow to the problem. These techniques are subject to drift as the person moves about the environment, particularly with out-of-plane rotation, and are therefore limited to short paths.

This chapter presents a approach for a person following vision system that addresses these issues by fulfilling the following criteria:

- allowing person wearing the same color as the background.
- allowing person rotating arbitrarily during tracking.
- allowing person walking in a cluttered environment including other people walking around.

Firstly the overall architecture of the system is described in Section 4.1. Section 4.2 describes the sparse disparity map constructed by feature matching between two stereo images. Section 4.3 demonstrates the detailed algorithm to extract person from background. Section 4.4 presents the robot control strategy. Experimental results are shown in Section 4.5. Section 4.6 closes with a summary.

4.1 System overview

The system consists of a pair of forward-facing stereo cameras on a mobile robot. The Binocular Sparse Feature Segmentation (BSFS) for processing the binocular video, shown in Figure 4.1, consists of two modes. In detection mode, sparse features are matched between the two images to yield disparities, from which the segmentation of foreground and background is performed. Once the person is detected the system enters tracking mode, in which the existing features on the person are tracked from frame to frame. Features not deemed to belong to the person are discarded, and once the person has been lost the system returns to detection mode. In both modes the results of the feature algorithm are combined with the output of

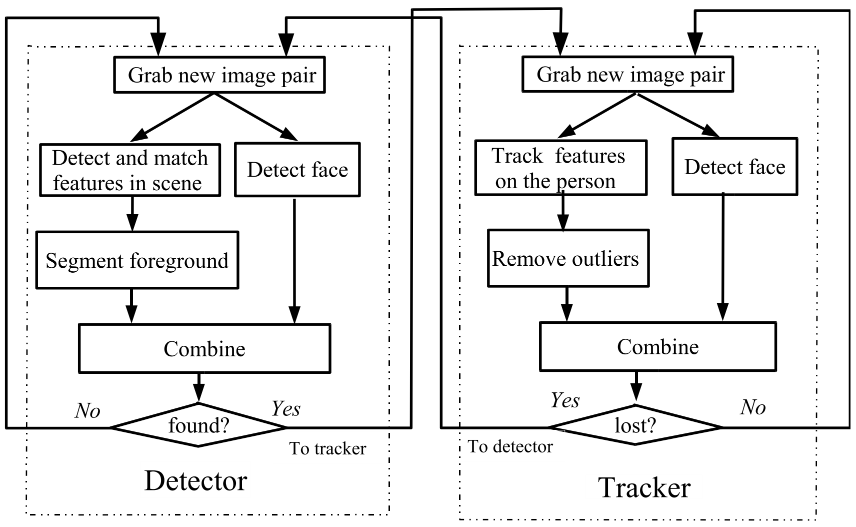

Figure 4.1: Overview of the person following algorithm.

a face detector, which provides additional robustness when the person is facing the camera.

4.2 Computing disparity between feature points

Feature points are automatically matched, both between the two stereo images and in one sequence over time, using the Lucas-Kanade approach [7, 84, 95]. In detection mode, the features are matched between the stereo images to compute the disparity between them. At time t, features are selected in the left image I_t^L and matched in the right image I_t^R, after which the resulting features in the right image are matched again in the left image. This left-right consistency check [35] discards features whose initial and final locations are not within a tolerance ϵ_t, thus improving robustness by removing unreliable features. (We set $\epsilon_t = 2$ in our experiments.) The horizontal disparities of the remaining features are stored for the later processing stages. (Since the cameras are approximately aligned, the vertical disparities are nearly zero and are therefore ignored.) The result on a pair of images is shown in

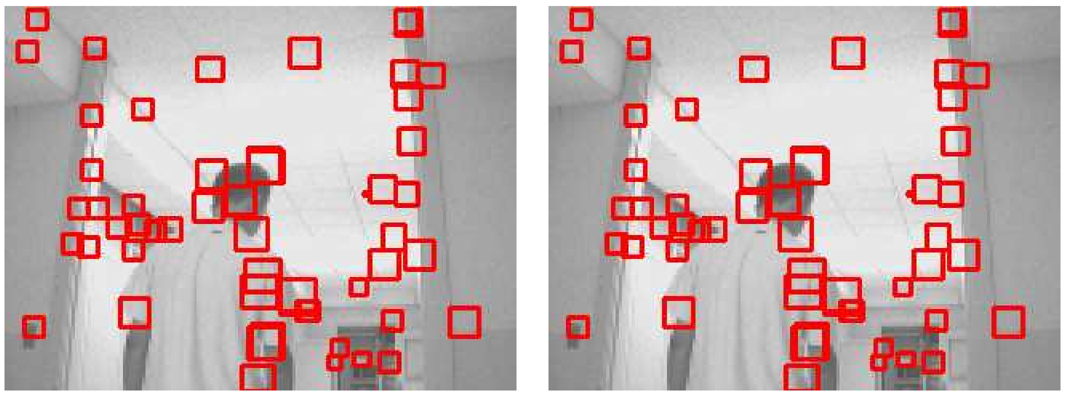
Figure 4.2: Left and right images with features overlaid. The size of each square indicates the horizontal disparity of the feature. Since disparity is inversely proportional to depth, smaller squares are farther from the robot.

Figure 4.2.

4.3 Segmenting the foreground

Once the features have been reliably matched, those belonging to the person are segmented from other features using both disparity and motion cues. A three-step procedure removes features that are not likely to belong to the person, based upon (1) the known disparity of the person in the previous image frame, (2) the estimated motion of the background, and (3) the computed motion of the person. These three steps are now described.

Let $\mathbf{f}_t = (x_t, y_t, d_t)$ be the image coordinates (x_t, y_t) of a feature along with its disparity d_t at time t. The first step simply discards features for which $\mid d_t - \tilde{d}_t \mid > \epsilon_d$, where $\tilde{d}_t$ is the current estimate of the disparity of the person. This estimate is initially obtained from the face detector, as explained below, and is maintained thereafter by the tracker.

The second step estimates the motion of the background by computing a 4×4

affine transformation matrix H between two image frames at times t and $t+1$:

$$\begin{bmatrix} \mathbf{f}_t^i \\ 1 \end{bmatrix} = H \begin{bmatrix} \mathbf{f}_{t+1}^i \\ 1 \end{bmatrix}. \tag{4.1}$$

At least three points are required to solve for H:

$$H = F_t F_{t+1}^T \left[F_{t+1} F_{t+1}^T \right]^{-1}, \tag{4.2}$$

where F_t and F_{t+1} are the $4 \times N$ matrices consisting of N features:

$$F_t = \begin{bmatrix} \mathbf{f}_t^1 & \mathbf{f}_t^2 & \cdots & \mathbf{f}_t^N \\ 1 & 1 & \cdots & 1 \end{bmatrix}_{4XN}. \tag{4.3}$$

Features that fit the resulting motion are determined by

$$\left\| H\mathbf{f}_{t+1}^i - \mathbf{f}_t^i \right\| \leq \epsilon_h, \tag{4.4}$$

where $\epsilon_h = 1.5$ in our experiments. Due to the possible distraction caused by other moving objects in the scene, along with errors from the tracker and approximation errors in the motion model, the background motion cannot be estimated by simply fitting a model to all the features. Even a robust fitting that discards outliers will not be reliable, because the number of outliers may exceed the number of inliers.

Instead we apply the random sample consensus (RANSAC) algorithm [32] to find small groups of features (containing at least five features) with consistent motion. We repeatedly select five random features from among the background features (determined by disparity), enforcing a minimum distance between the features to ensure that they are well spaced in the image. From these features we use Equation (4.2) to calculate the background motion H_b, which is then applied to all the background features to record the number of inliers. This process is repeated several times, and the motion model with the largest number of inliers is taken to be the background motion. Once the background motion has been estimated, the foreground features that do not match this motion model are discarded using Equation (4.4).

To remove independently moving objects, the third step calculates the motion model H_p of the person using the remaining features. RANSAC is applied, as before, to yield the dominant motion among these features. A second motion model is then determined by applying RANSAC to the features that do not fit the dominant motion model. Two cues are used to distinguish the person from another moving object, namely the size of the group and the proximity to the previous position of the person. Thus, the group that maximizes $n(s_i) - m(s_i)$, $i = 1, 2$, where $m(s_i)$ is the mean squared error M_i between the centroid of the ith group and the previous person position, taken in the horizontal direction: $m(s_i) = M_i/(M_1 + M_2)$; and $n(s_i)$ is the relative number of features N_i of the ith group: $n(s_i) = N_i/(N_1 + N_2)$. The remaining features are then projected onto the horizontal axis, and the largest connected component is retained. The bottom right image of Figure 4.3 shows the final result of the detector.

After these steps, the features that remain are assumed to belong to the person. If the number of features exceeds a threshold, then the person is detected, and the system enters tracking mode. An example of the three steps applied to a portion of the video sequence is shown in Figure 4.3. The person is typically detected after just two image frames.

An example showing the results of the algorithm when the background has a similar disparity as the person is shown in Figure 4.4. In this case the disparity test (Step 1) finds almost no features on the background, thus rendering the first two

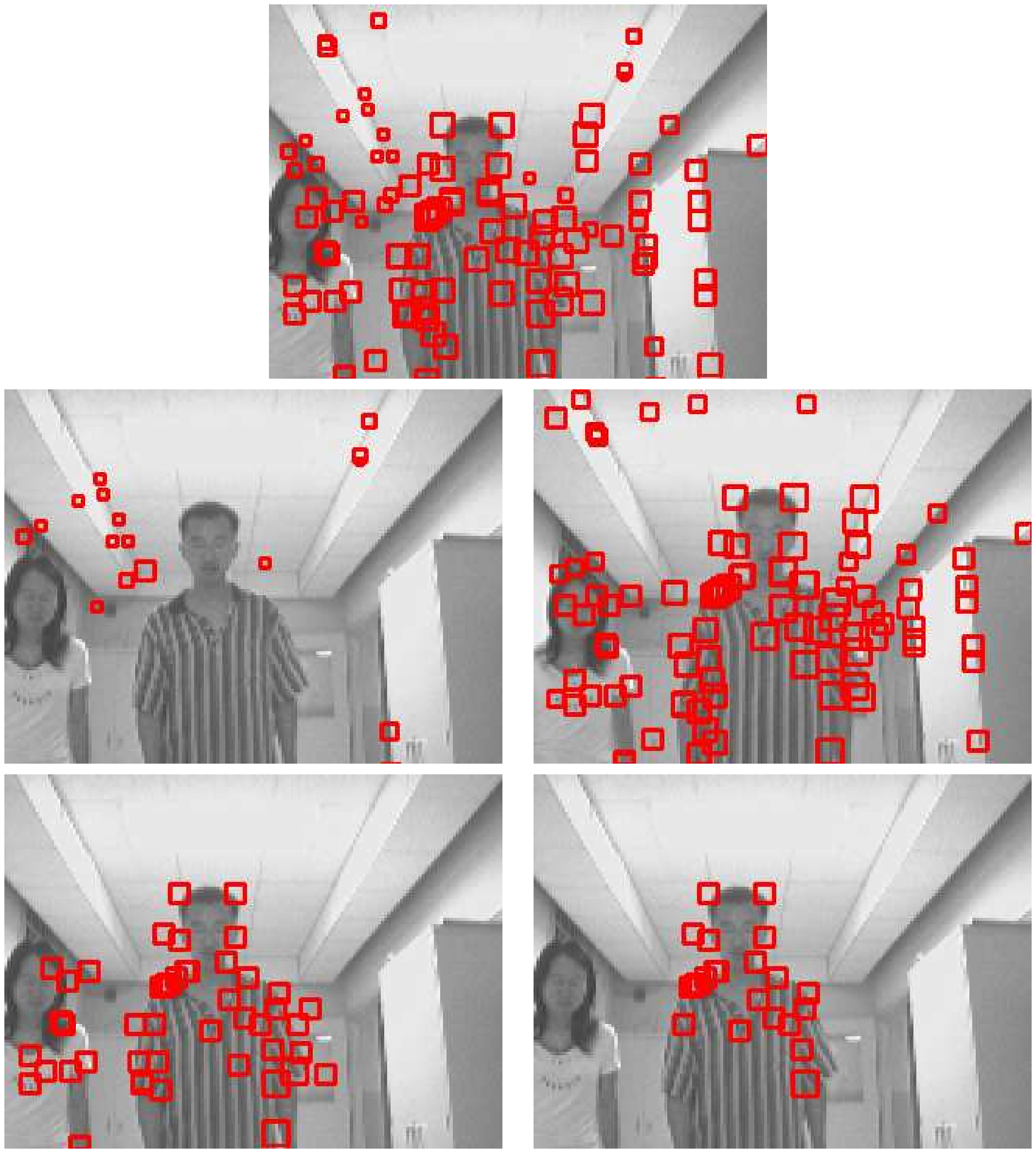

Figure 4.3: Step-by-step results of the person detection algorithm. Top: All the features that pass the consistency check. Middle: The background (left) and foreground (right) features after the disparity test (Step 1). Bottom left: The features that remain after removing those that fit the background motion (Step 2). Bottom right: The features that remain after removing those that do not fit the person motion (Step 3).

steps ineffective at discarding background features. Step 3, however, uses the motion of the person to correctly discard the features on the background, resulting in features that lie almost entirely on the person. Figure 4.4 shows that the algorithm does not assume that the person is the closest object. As shown in Figure 4.5, this procedure is insufficient when the person is not moving, because Step 2 of the algorithm incorrectly discards the features on the person due to the similarity between the motion of the person and background. To solve this problem, the robot simply waits until a sufficient number of features are detected before moving.

In both the detection and tracking modules, the Viola-Jones frontal face detector [98] is applied at constant intervals. The face detector uses integral images to compute features resembling Haar wavelets, and a cascade architecture is used to enable the algorithm to efficiently evaluate all image locations. This detector is used both to initialize the system and to enhance robustness when the person is facing the camera. In both modes, the face detector is combined with the results of the detection or tracking algorithms by discarding features that lie outside a body bounding box just below the face detection. Note, however, that our system does not require the person to face the camera.

4.4 Tracking and camera control

Once the person has been detected, control passes to the tracking module. The person is tracked using the same features by applying Lucas-Kanade from frame to frame. Over time features are lost due to several reasons. Some features are discarded automatically by the Lucas-Kanade algorithm because a sufficient match is not found in the next frame. More commonly, features drift from the person to the background, in particular when the person self-occludes by rotating. To detect this event, features

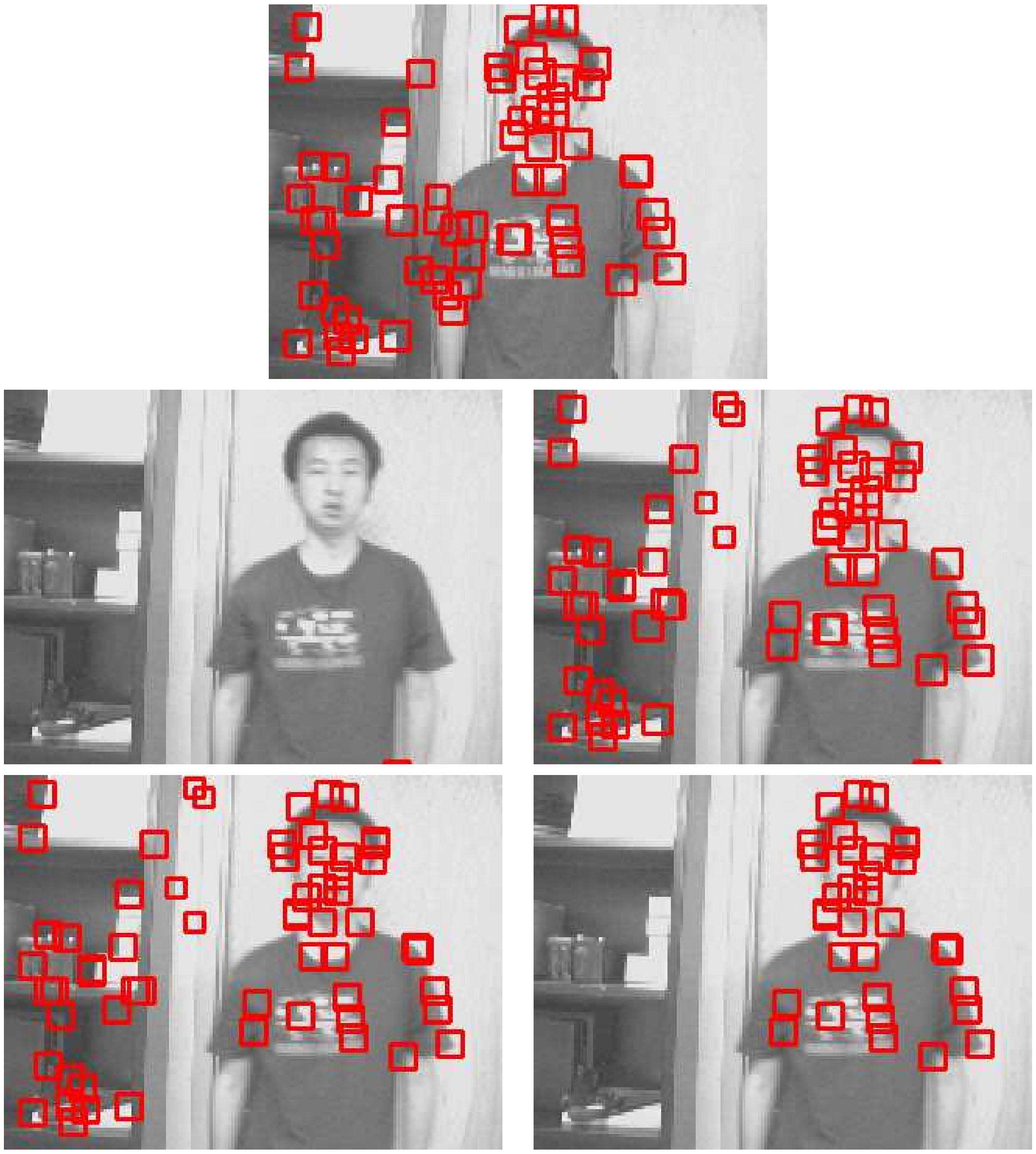

Figure 4.4: The person and background have similar disparity. Step-by-step results when the person and background have similar disparity. The images follow the same order as in Figure 4.3. The algorithm does not assume that the person is the closest object.

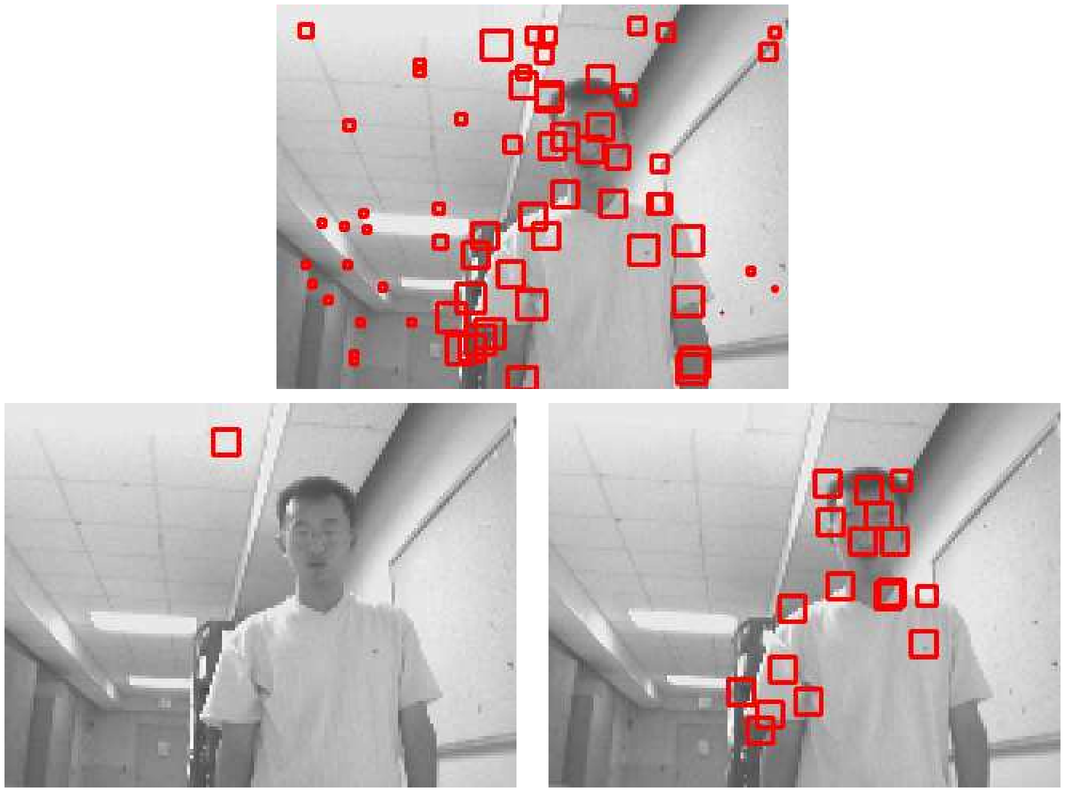

Figure 4.5: Two additional examples. Top: All the features that pass the consistency check. Bottom: The final result of the person detection algorithm when the person is still (left) and moving (right).

are discarded when their disparity differs from the disparity of the person by more than the threshold ϵ_d. When a significant number of the original features have been lost, the tracker gives up, and control returns to the detection module.

A simple proportional control scheme is applied to the robot motors, i.e., the driving speed σ_d is set to be proportional to the inverse of the disparity d to the person, while the turning speed σ_t is set to be proportional to the product of the horizontal position p of the person in the image relative to center and the disparity, as follows:

$$\sigma_d = K_1 d,\ \sigma_t = K_2 p d, \tag{4.5}$$

where K_1, K_2 are constants (80 and 0.01, respectively). We have found this simple control scheme to be sufficient for our purposes.

4.5 Experimental results

The proposed algorithm was implemented in Visual C++ on a Dell Inspiron 700m laptop (1.6 GHz) controlling an ActivMedia Pioneer P3-AT mobile robot. Mounted on a tripod on the robot were two ImagingSource DFK21F04 Firewire cameras with 8.0 mm F1.2 lenses spacing approximately 5.5 cm apart yielding images of size 320×240. The OpenCV library [1] was used for the feature detection, feature tracking, and face detection. The maximum driving speed of the robot was 0.75 meters per second, while the maximum turning speed was 30 degrees per second. The entire system operates at an average of 16 Hz.

The algorithm has been tested extensively in indoor environments and moderately in outdoor environments. Figure 4.6 shows a typical run of the system, with the robot traveling over 100 meters. To initialize, the person faced the robot, after which the person walked freely at approximately 0.8 m/s, sometimes facing the robot and other times turning away. The environment was challenging because it contained a textured background, other people walking around, some lighting changes, and image saturation due to a bright ceiling light. Some example images from two experiments are shown in Figure 4.7 to demonstrate the ability of the system to handle an untextured shirt that is the same color as the background, as well as moving objects in the scene.

To further test the robustness of the algorithm, five people were asked to walk around the environment in a serpentine path for approximately five minutes. Two experiments were captured for each person, one at a speed of approximately 0.5 m/s and another at approximately 0.8 m/s. The shirts of the people were white, white, yellow, blue, and textured. Some of the people always faced the robot, some rarely faced the robot, and other faced the robot occasionally. Of the ten trials, the robot succeeded nine times (90% success rate). The only failure was caused by the person walking quickly away from the camera with an untextured shirt. In other experiments, the robot has successfully tracked the person for more than 20 minutes without an error.

We compared our algorithm with a popular color histogram-based algorithm, namely the Camshift technique in OpenCV. The latter was found to be much more likely to be distracted by background or lighting changes than ours. Figure 4.8 shows a typical run, in which the robot lost the person when he turned around the corner, whereas our algorithm successively followed the person to the end. In this experiment the person intentionally walked in a fairly straight path, and the person wore a shirt whose color was distinct from the background, in order to make the task easier for the color-based algorithm. Some images from a different experiment comparing the two algorithms are shown in Figure 4.9. It should be noted that more advanced color-

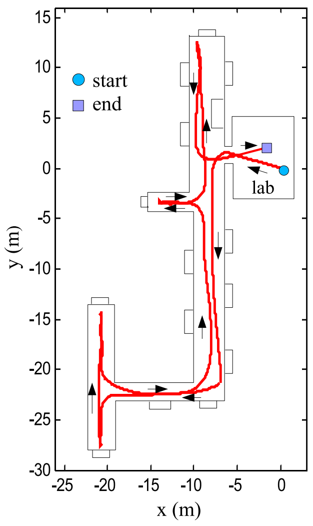

Figure 4.6: Path of a person following experiment. The robot path as it followed the person through the hallways of our laboratory in an experiment.

based tracking algorithms will also fail whenever the target has a similar appearance to the background.

4.6 Summary

We have presented an algorithm for following a person using a grayscale stereo pair of cameras on a mobile robot using sparse features. The features are matched between the stereo images and then tracked over time, while a RANSAC-based procedure discards features that do not belong to the person. An efficient face detector is used both to initialize the system and to increase robustness when the person is facing the camera. Compared with previous techniques, this approach has the advantage of not requiring the user to wear a shirt colored distinctly from the background or to always face the robot. It also demonstrates some amount of insensitivity to lighting variations and moving people in the scene.

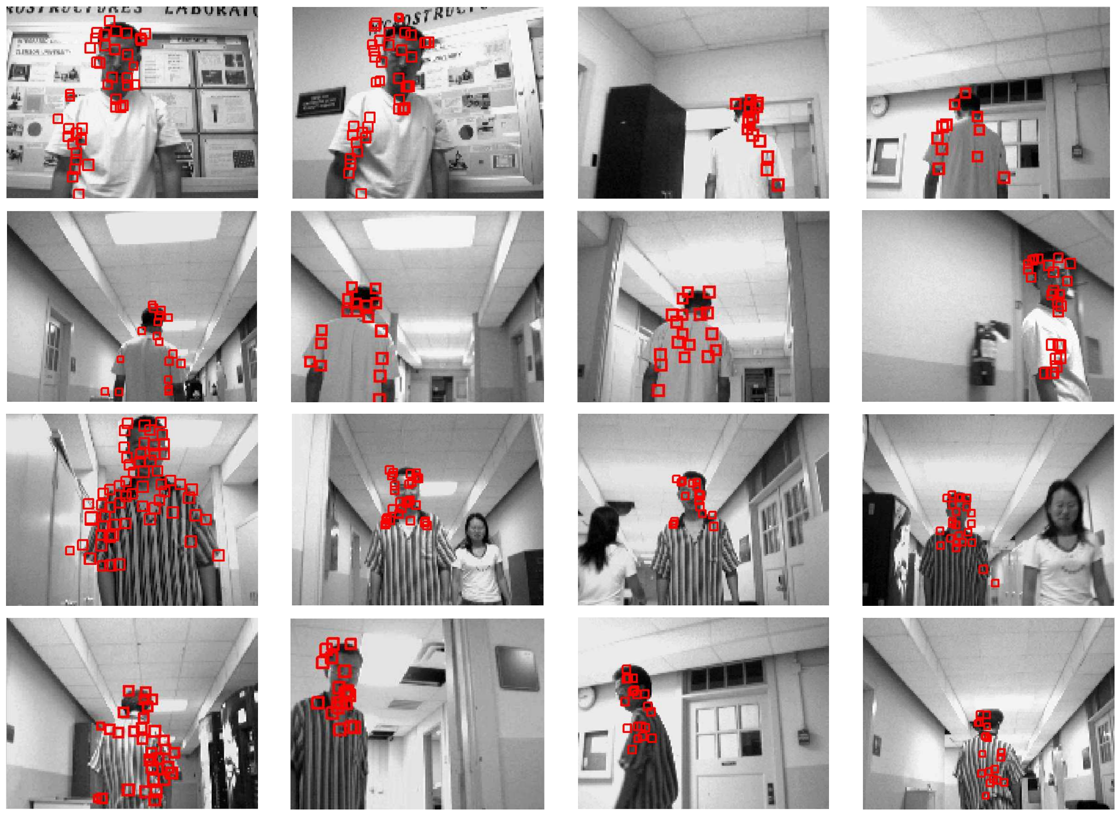

Figure 4.7: Sample images from a person following video. Top two rows: Images taken by the left camera of the robot during an experiment in which the person wore a shirt with a similar color to the background. Bottom two rows: Images from an experiment in which another person walked by the camera.

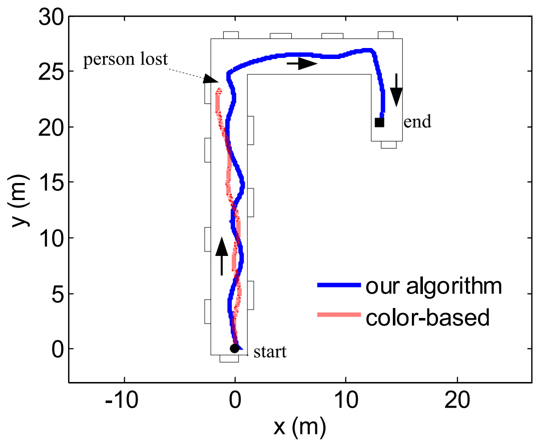

Figure 4.8: Comparison with color-histogram-based tracking. The color-based algorithm lost the person when he turned down the hallway, whereas our algorithm succeeded.

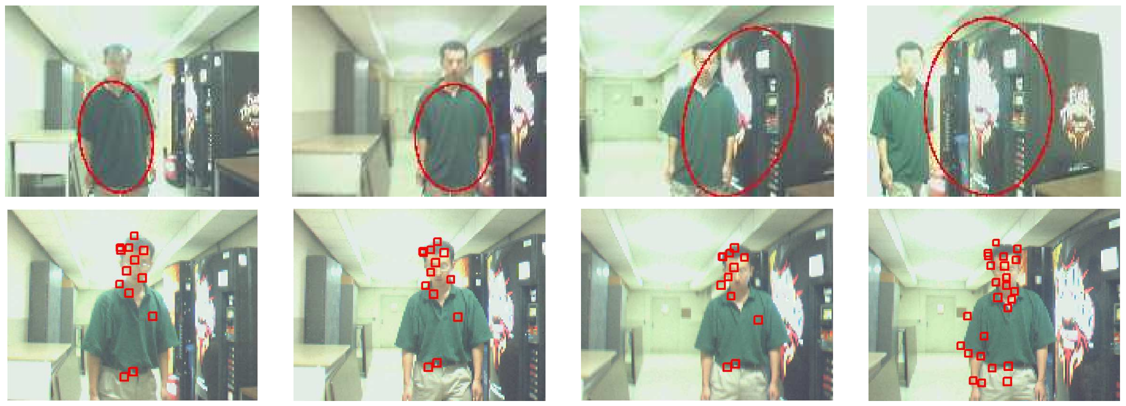

Figure 4.9: Sample images for comparison with color-histogram-based tracking. The results of the color-based algorithm (top) and our algorithm (bottom) in an environment with a textured background. The former loses the person, while the latter succeeds.

Chapter 5

Door Detection

Doors are important landmarks for indoor mobile robot navigation. They mark the entrance/exit of rooms in many offices and laboratory environments. The ability of a robot to detect doors can be a key point for a robust navigation. What visual characteristics make a door appear to be a door. In other word, what features can be used by computer vision to automatically locate doors in images? Figure 5.1 shows the main features which characterize a door. However, these features are not always present or cannot always be detected in a single camera image, for example, the color of door and wall might not be different; the kick plate might not exist; the top frame of the door (lintel) might be occluded; the door knob and hinge might be too small in the image to be detected. It is our belief that the solution to this problem cannot be achieved by focusing only upon one piece of local evidence. Rather, the integration of a variety of cues is needed to overcome the noise of sparse, local measurements. As a result, we approach the problem recognizing that recognition is inherently a global process.

As shown in Figure 5.2, two vision-based door detection algorithms are developed, one based on Adaboost and the other on Data-Driven Markov Chain Monte

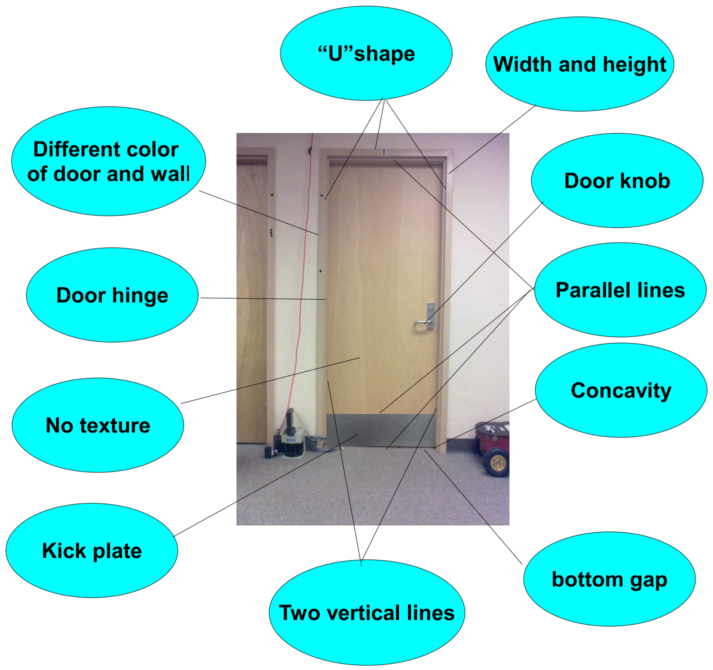

Figure 5.1: Door features. Door is characterized by several features.

Carlo (DDMCMC). Models of doors utilizing a variety of features, including prior and posterior features are presented. The Bayesian formulations are constructed and a Markov chain is designed to sample proposals. The features are combined using Adaboost to ensure optimal linear weighting. Doors are detected based on the idea of maximizing a posterior probability (MAP). Data-Driven techniques are used to compute importance proposal probabilities, which drive the Markov Chain dynamics and achieve speedup in comparison to the traditional jump diffusion methods.

In Section 5.1, we formulate the door detection problem in a Bayesian framework and build the door detection model, including a prior model and a data model. Section 5.2 and Section 5.3 formulate the score of a door candidate as a linear combination of various pieces of evidence. Based on the score function, Section 5.4 and Section 5.5 present two approaches, Adaboost and Data Driven Markov Chain Monte

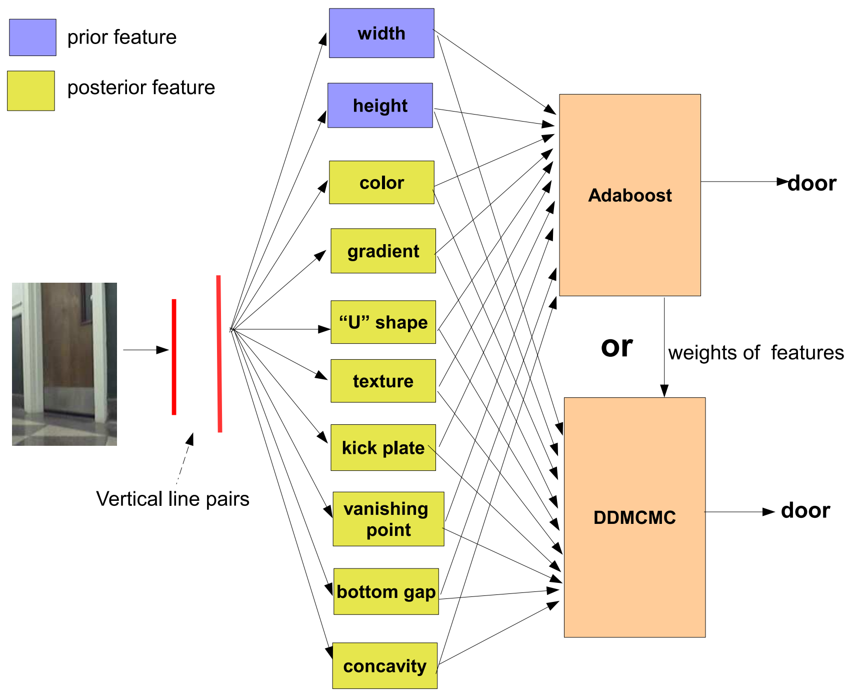

Figure 5.2: Overview of our approach to detect doors. Several features are combined using the AdaBoost or DDMCMC

Carlo (DDMCMC), to detect doors. In Section 5.6 we propose three methods to automatically detect wall/door color. Section 5.7 proposes an approach to detect open doors. In addition to door detection, we develop a door tracking algorithm, which is presented in Section 5.8. Experimental results are shown in Section 5.9. Finally, Section 5.10 presents the conclusions.

5.1 Bayesian formulation

In this section, we formulate the problem in a Bayesian framework. Assuming that the camera is oriented so that the image plane is perpendicular to the floor, a door $\mathbf{d} = (x_l, x_r, y_{lt}, y_{lb}, y_{rt}, y_{rb})$ in an image I is represented using the six coordinates of the four end points of two vertical line segments ℓ_l and ℓ_r. Our goal is to find the number of doors in the image, along with the location of each door. Invoking the first-order Markov assumption, and letting $\mathbf{d}_1, \ldots, \mathbf{d}_k$ to represent the sequence of k doors from left to right in the image, the goal is expressed probabilistically as maximizing

$$p(k, \mathbf{d}_1, \ldots, \mathbf{d}_k \mid I) = p(\mathbf{d}_1 \mid I) p(k \mid I) \prod_{i=2}^{k} p(\mathbf{d}_i \mid I, \mathbf{d}_{i-1}). \tag{5.1}$$

A straightforward approach to solve this problem would be to apply reversible jump Markov chain Monte Carlo (RJMCMC) to simultaneously estimate the number k and the joint configuration of all the doors. Such an approach, however, is notoriously computationally intensive. In contrast, the formulation above suggests that a simpler approach might be sufficient: search the image from left to right (or vice versa) in a sequential manner to find the doors one at a time. Since the coupling between the doors can be modeled as a prior on location, the primary problem becomes to find a single door given the image by maximizing $p(\mathbf{d} \mid I)$, which, according to Bayes' rule, is

$$p(\mathbf{d} \mid I) \propto p(I \mid \mathbf{d}) p(\mathbf{d}). \tag{5.2}$$

Taking the log likelihood, this is equivalent to maximizing the following functional:

$$E(\mathbf{d}) \quad = \quad \Psi_{data}(I \mid \mathbf{d}) + \Psi_{prior}(\mathbf{d}), \tag{5.3}$$

where the likelihood is $p(I \mid \mathbf{d}) = \exp\{\Psi_{data}(I \mid \mathbf{d})\}$, and the prior is $p(\mathbf{d}) = \exp\{\Psi_{prior}(\mathbf{d})\}$.

5.2 Prior model

The prior model captures information about the expected door configuration without considering image evidence relevant to the particular door being found. We formulate the prior score of a door candidate as a linear combination of various pieces of evidence:

$$\Psi_{prior}(\mathbf{d}) = \sum_{i=1}^{N_{prior}} \alpha_i f_i(\mathbf{d}), \tag{5.4}$$

where N_{prior} is the number of tests aggregated, and α_i is the weight that governs the relative importance of the ith test. (As described later, the Adaboost algorithm will be used to ensure optimal weighting.) All the tests f_i are normalized to yield values between 0 and 1, leading to a formulation of expert opinions similar to the sum rule of Kittler and colleagues [49, 48, 92].

Our approach employs two tests ($N_{prior} = 2$). First, we compare the width w of the door in world coordinates with the expected width $\hat{w}$ of real doors:

$$f_1(\mathbf{d}) = \exp\left\{-\frac{(w-\hat{w})^2}{2\sigma_w^2}\right\}. \tag{5.5}$$

Several real world doors were measured in order to determine the expected door width and standard deviation, leading to $\hat{w} = 0.96$ m, and $\sigma_w = 0.08$ m. To enable the measuring of the door width in world coordinates, the camera is first calibrated by capturing an image of a piece of paper of known dimensions placed on the floor. The normalized Direct Linear Transformation (DLT) [41] is used to calculate a homography between the floor plane and the image plane, which enables the image to world transformation of the two points at the bottom of the door.

Secondly, we expect the height of the two vertical door edges (in world coordinates) to be similar to the height of a standard door. However, since the lintel (top) of the door could be occluded, it may be impossible to measure the height of these two edges. Instead, we measure the height of the hinge edge between the ground plane and the horizontal plane passing through the optical center of the camera. The ratio ρ of the door width to this height should be constant, leading to

$$f_2(\mathbf{d}) = \exp\left\{-\frac{(\rho - \hat{\rho})^2}{2\sigma_\rho^2}\right\}, \tag{5.6}$$

where $\hat{\rho}$ is the ratio of a standard door. Based on measurements of 25 real doors, and a camera height of 0.32 m above the ground, we obtain $\hat{\rho} = 3.0$ and $\sigma_\rho = 0.2$.

Figure 5.3 illustrates the computation of $\rho = \Delta_x/\Delta_y$. Given the homography H between the image and world coordinate systems, $H^{-1}\begin{bmatrix} x_r & y_{rb} & 1 \end{bmatrix}^T$ are the homogeneous world coordinates of the rotation axis of the door in the ground plane. Let C be the 3×3 homogeneous matrix representing the circle centered at this location with radius equal to the width of the door. Then $H^{-T}CH^{-1}$ is the ellipse in the image tracing the coordinates of the bottom of the left line as the door rotates about its hinge. For any image point along this ellipse, the world width of the door is, of course, the same. Thus, the point $(\widetilde{x}, y_{rb})$ indicates the image location of the bottom of the door that would result if the door were parallel to the image plane. Assuming unity aspect ratio of the image sensor, this yields the ratio as

$$\rho = \frac{\Delta_x}{\Delta_y} = \frac{x_r - \widetilde{x}}{y_{rb} - v_0}. \tag{5.7}$$

Figure 5.4 demonstrates an example with real images. As can be seen, the trace of a door rotating around its hinges is successfully achieved.

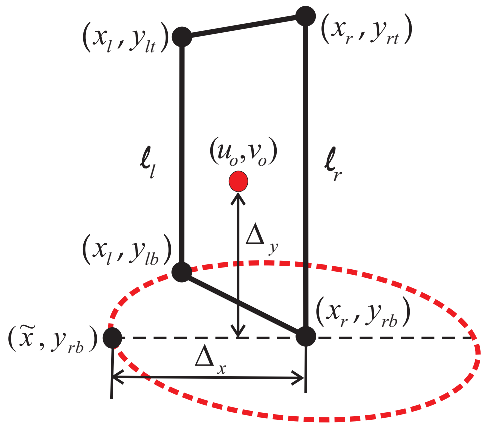

Figure 5.3: Door configuration: A door candidate can be described using two vertical lines, ℓ_l and ℓ_r, defined by four end points (x_l, y_{lt}), (x_l, y_{lb}), (x_r, y_{rt}) and (x_r, y_{rb}). Assuming that the door rotates around the right vertical line, the bottom left corner of the door is located at $(\tilde{x}, y_{rb})$ when the door is parallel to the image plane. Δ_x is the width of the aligned door in image coordinates, while Δ_y is the height from the bottom of the door to the horizontal line passing through the principal point (u_0, v_0) of the image.

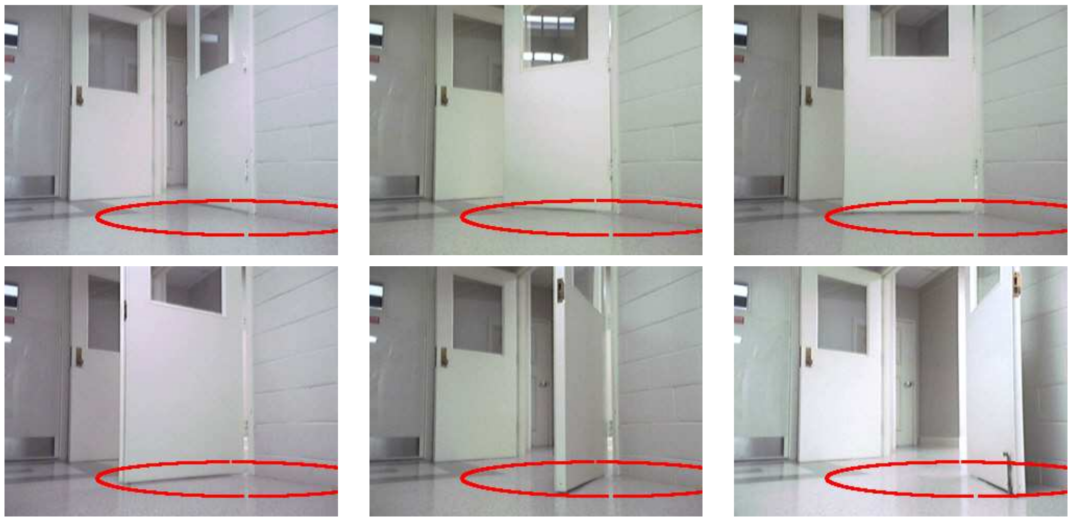

Figure 5.4: The trace of a door rotating around its hinges. In the top-right image, the door is parallel to the image plane.

5.3 Data model

Similar to the prior model, the data model is formulated as a linear combination of evidences:

$$\Psi_{data}(I \mid \mathbf{d}) = \sum_{j=1}^{N_{data}} \beta_j g_j(I \mid \mathbf{d}), \tag{5.8}$$

where the weights β_j are chosen based on Adaboost, and all the tests g_j are normalized between 0 and 1. We now describe the $N_{data} = 9$ tests.

5.3.1 Image gradient along edges (g_1)

Perhaps the most distinguishing visual characteristic of doors in images is the change in intensity that usually accompanies the sides of the door. As a result, we measure

$$g_1(\mathbf{d}, I) = \exp\left\{ - \sum_{\mathbf{x} \in \mathcal{R}_e} \left| (\nabla I(\mathbf{x}))^T \mathbf{n}(\mathbf{x}) \right| \right\}, \tag{5.9}$$

where $\mathbf{x}$ is a pixel on the door edge, $\nabla I(\mathbf{x})$ is the 2D image gradient at the pixel, and $\mathbf{n}(\mathbf{x})$ is the normal to the door edge at the pixel. The set $\mathcal{R}_e$ of pixels includes the left and right edges of the door, the bottom edge, and the top edge (if $x_{lt} \neq 0$ and $x_{rt} \neq 0$). The gradient of the image is computed using a 3-tap separable Gaussian derivative filter with a standard deviation of 1 pixel.

5.3.2 Placement of top and bottom edges (g_2 and g_3)

After computing the gradient of the image, vertical and horizontal line segments are found by applying the Douglas-Peucker line fitting algorithm [28], as modified in [24], to the output of the Canny edge detector. Appendix B presents the detail of the modified Douglas-Peucker line fitting algorithm. The horizontal segments between the two vertical door edges are compared to determine the topmost segment, which is then extended to intersect with the vertical edges, yielding expected values $\hat{y}_{lt}$ and $\hat{y}_{rt}$ for the top points of the two edges. If there is no such segment, then $\hat{y}_{lt} = \hat{y}_{rt} = 0$, indicating a lintel-occluded door. Similarly, the bottom endpoints of the vertical edges are compared with the line forming the boundary between the wall and the floor:

$$\begin{aligned} g_2(I \mid \mathbf{d}) &= \exp\left\{-\frac{(y_{lt} - \hat{y}_{lt})^2}{2\sigma_t^2} - \frac{(y_{rt} - \hat{y}_{rt})^2}{2\sigma_t^2}\right\} && (5.10) \\ g_3(I \mid \mathbf{d}) &= \exp\left\{-\frac{(y_{lb} - \hat{y}_{lb})^2}{2\sigma_b^2} - \frac{(y_{rb} - \hat{y}_{rb})^2}{2\sigma_b^2}\right\}, && (5.11) \end{aligned}$$

where $\hat{y}_{lb}$ and $\hat{y}_{rb}$ are the intersection of the wall-floor boundary with the two vertical edges, where the wall-floor boundary is computed by Image-based segmentation of indoor corridor floors [58]. The standard deviations σ_t and σ_b are set to 5 pixels.

5.3.3 Color and texture (g_4 and g_5)

Color provides a helpful cue to distinguish the door from its surroundings. We use the Bhattacharyya coefficient

$$g_4(I \mid \mathbf{d}) = 1 - \sum_{i=1}^{N_{col}} \sqrt{\phi(i)\phi_{wall}(i)} \qquad (5.12)$$

to compare the normalized color histogram ϕ computed using the pixels inside the door parallelogram, and the normalized color histogram ϕ_{wall} that models the colors in the wall, where $N_{col} = 8^3$ is the number of bins in the histogram. The HSV (hue, saturation, value) color space is used due to its insensitivity to illumination changes compared with RGB. In our system the robot builds a model of the wall color automatically as it moves down the corridor, described later.

Although the top half of a door may contain windows, signs, or flyers, the bottom half of a door is often untextured. We measure texture using the entropy of the normalized histogram of the image gradient magnitude and phase:

$$g_5(I \mid \mathbf{d}) = 1 - \frac{1}{\eta} \sum_{i=1}^{N_{tex}} \sum_{j=1}^{M_{tex}} \phi_{tex}(i,j) \log\left(\phi_{tex}(i,j)\right), \tag{5.13}$$

where i and j index the magnitude and phase, respectively, in the histogram ϕ_{tex}; $N_{tex} = 16$ and $M_{tex} = 8$ are the number of bins along the two directions of the histogram; and $\eta = \log\left(N_{tex} M_{tex}\right)^{-1}$ is the entropy of a uniform distribution, used to normalize the result. Entropy is used to avoid being distracted by strong intensity edges that may occur near the bottom of the door, due to the boundary of the kick plate. Typically, such edges are fairly localized in magnitude and phase, thus resulting in low entropy.

5.3.4 Kick plate (g_6)

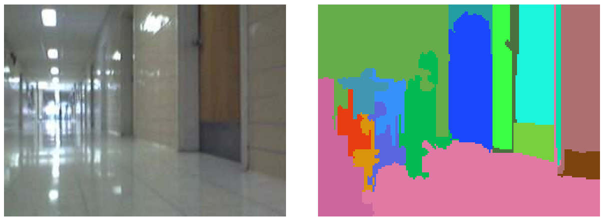

Figure 5.5: Kick plate. LEFT: A door with a kick plate. RIGHT: The segmentation of the image using the method of Felzenszwalb et al. [31]. The kick plate is the olive green region at the bottom of the door.

Some doors have kick plates near the bottom which provide an additional cue for door detection. The image is first segmented using the method of Felzenszwalb et al. [31], as shown in Figure 5.5.

A region in the segmented image is considered as kick plate if it is located within the two vertical door lines and the bottom of the door candidate, and if its height is about a quarter of the height of the door candidate. This results in

$$g_6(I \mid \mathbf{d}) = \exp\left\{-\frac{(k_x - \hat{k}_x)^2}{2\sigma_{kx}^2}\right\} \exp\left\{-\frac{(k_y - \hat{k}_y)^2}{2\sigma_{ky}^2}\right\}, \tag{5.14}$$

where (k_x, k_y) is the centroid of the kick plate, $\hat{k}_x = x_r - x_l$ is the x coordinate of the centroid of the door candidate, and $\hat{k}_y = \frac{1}{4}\Delta y$ is the expected y coordinate of the centroid of the kick plate, assuming that the height of the kick plate is approximately one half the distance from the bottom of the door to the principal point. We set $\sigma_{kx} = \frac{1}{4}(x_r - x_l)$ and $\sigma_{ky} = \frac{1}{4}\Delta y$. If no kick plate is detected, then $g_6 = 0$.

5.3.5 Vanishing point (g_7)

The vanishing point provides an additional test, as shown in Figure 5.6. The vanishing point is computed as the mean of the intersection of pairs of non-vertical lines inside the door region:

$$\begin{bmatrix} wv_x \\ wv_y \\ w \end{bmatrix} = \frac{1}{N_v} \sum_{i,j} \begin{bmatrix} a_i \\ b_i \\ c_i \end{bmatrix} \times \begin{bmatrix} a_j \\ b_j \\ c_j \end{bmatrix}, \tag{5.15}$$

where the sum is over all pairs of lines i and j, N_v is the number of such pairs, each line is described by an equation $ax + by + c = 0$, $\times$ denotes the cross product, and the result is expressed in homogeneous coordinates. The vanishing point $\mathbf{v} = \begin{bmatrix} v_x & v_y \end{bmatrix}^T$ is determined by dividing by the scaling factor w. Vanishing point consistency is measured by

$$g_7(I \mid \mathbf{d}) = \exp\left\{-\frac{(v_x - \hat{v}_x)^2}{2\sigma_{vx}^2}\right\} \exp\left\{-\frac{(v_y - \hat{v}_y)^2}{2\sigma_{vy}^2}\right\}, \tag{5.16}$$

where $\hat{v} = [\,\hat{v}_x \quad \hat{v}_y\,]^T$ is the vanishing point estimated as the mean of the intersection of pairs of non-vertical lines outside the door. We set σ_{vx} and σ_{vy} as $\frac{1}{10}$ of the width and height, respectively, of the image.

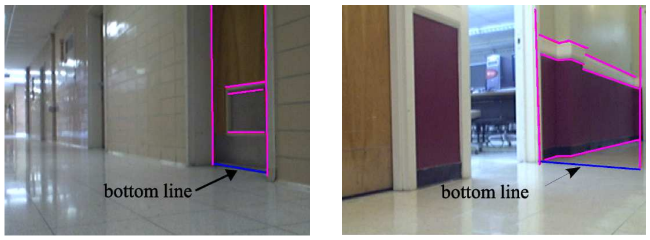

Figure 5.6: Vanishing point. LEFT: The bottom line of a door or wall/floor boundary intersects the vanishing point. RIGHT: In contrast, a distracting line caused by shadows does not.

5.3.6 Concavity (g_8)

In many environments doors are receded into the wall, creating a concave shape for the doorway. A simplified concave door structure is illustrated in Figure 5.7, leading to two observations regarding the intensity edges:

- A slim “U” exists consisting of two vertical lines (the door edge and jamb) and one horizontal line (between the door frame and floor); and
- The bottom edge of the door is slightly recessed from the wall-floor edge.

Let (x, y) be a pixel on the line formed by extending the wall/floor boundary in front of the door (the dashed line in the figure), and let (x, y_b) be the pixel on the bottom of the door in the same column of the image. The slim “U” is tested by comparing its width w_u with an expected width $\hat{w}_u$:

$$h_U = \exp\left\{-\frac{(w_u - \hat{w}_u)^2}{2\sigma_u^2}\right\}, \tag{5.17}$$

while the recession is tested by

$$h_R = \exp\left\{-\frac{(y - y_b - \Delta\hat{y}_{rec})^2}{2\sigma_r^2}\right\}, \tag{5.18}$$

where $\hat{w}_u = \frac{1}{4}(x_r - x_l)$, $\Delta\hat{y}_{rec} = 2$ pixels, $\sigma_u = 2$ pixels, and $\sigma_r = \frac{1}{4}(x_r - x_l)$, where $x_r - x_l$ is the width of the door in the image.

The value g_8 is then defined as:

$$g_8(I \mid \mathbf{d}) = h_U h_R. \tag{5.19}$$

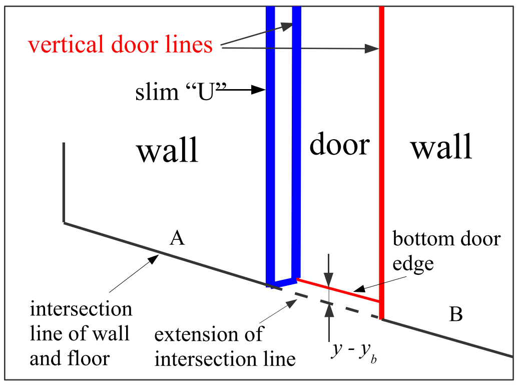

Figure 5.7: Concavity. A concave door exhibits a slim “U” to its side, as well as a recession of the bottom edge. This geometry yields a concavity test which is an important cue for detecting doors.

5.3.7 Gap below the door (g_9)

Almost without exception, doors are constructed with a gap below them to avoid unnecessary friction with the floor as they open or close. As a result, when the light in the room is on, the area under the door tends to be brighter than the immediate surroundings, whereas if the light is off, then the area tends to be darker due to the shadow. In either case this piece of evidence, which is often just a few pixels in height, provides a surprisingly vital cue to the presence of the door, which is illustrated in Figure 5.8. In particular, this phenomenon is important for disambiguating the bottom door edge from the wall-floor edge. For each pixel along the bottom door edge, we compute the minimum and maximum intensities in the surrounding vertical profile and perform a test to ensure that the extremum value is near the center of the profile, and that the difference between the extremum value and the average of the surrounding values is above a threshold. The gap below the door is then measured as the ratio of the number of pixels N_g that satisfy the bottom gap test to the total number of pixels N_b along the bottom edge:

$$g_9 = \frac{N_g}{N_b}. \tag{5.20}$$

5.4 Door detection using Adaboost

Adaboost [34] is an algorithm to combine multiple weak classifiers into a strong classifier. As long as each weak classifier performs with at least 50% success, and the errors of the different classifiers are independent, then the algorithm is able to improve upon the error rate by optimally selecting the weights for the weak classifiers.

Let h_n be the nth weak classifier, and let $y = h_n(x)$ be the output of the

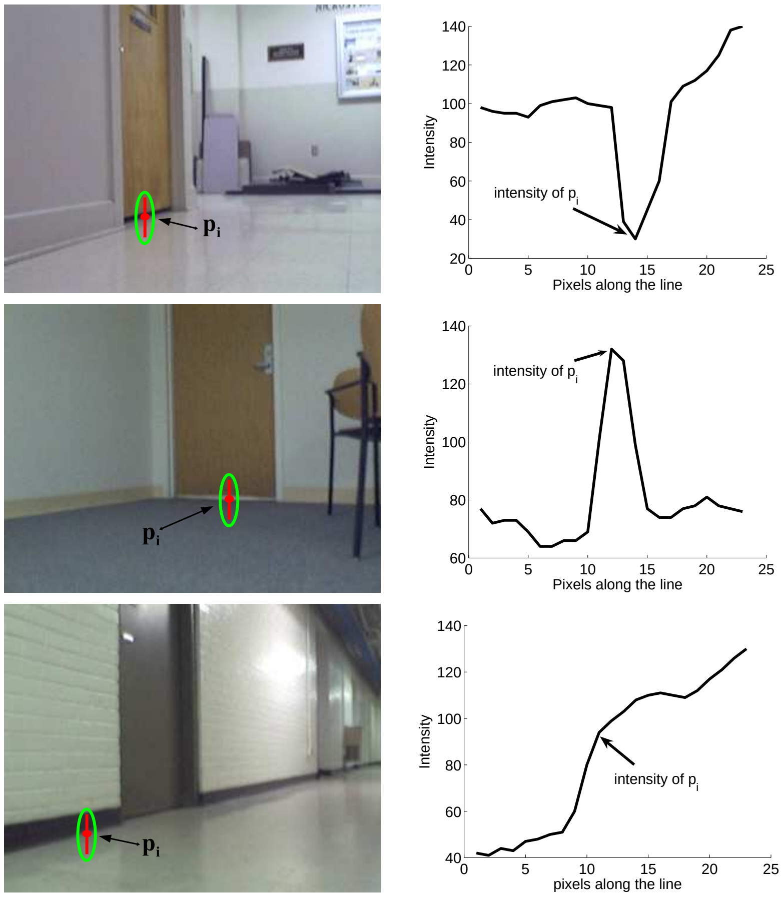

Figure 5.8: The intensity profile of a vertical slice around the bottom edge. LEFT: images. TOP-RIGHT: The intensity profile of a vertical slice around the bottom edge. The dark region caused by the shadow of the door indicates the presence of the door. MIDDLE-RIGHT: Alternatively, if the light in the room is on, a bright peak indicates the door's presence. BOTTOM-RIGHT: However, if the vertical slice covers the intersection of the wall and floor, the intensity profile changes smoothly, and no sharp peak occurs.

classifier to input x. In our case, x is the image and y is a binary label indicating whether a door was detected by the weak classifier. The strong classifier is given by a weighted sum of the weak classifiers:

$$\Psi(x) = \operatorname{sign}\left(\sum_{n=1}^{N} \alpha_n h_n(x)\right), \tag{5.21}$$

where α_n is the scalar weight found by AdaBoost indicating the importance of the weak classifier h_n, and $N = 5$. The weights are determined in an iterative manner according to

$$\alpha_n = \frac{1}{2}\left(\ln \frac{1-\varepsilon_n}{\varepsilon_n}\right), \tag{5.22}$$

where the error ε_n is given by

$$\varepsilon_n = Pr_{i\sim D_n}[h_n(x_i) \neq y_i] = \sum_{i:h_n(x_i)\neq y_i} D_n(i). \tag{5.23}$$

In this equation the output $y_i \in \{-1, +1\}$ is the ground truth for the training set, and $D_n(i)$ is the weight assigned to the ith training example on round n.

5.5 Door detection using DDMCMC

Markov Chain Monte Carlo (MCMC) is used here to find the MAP solution to door detection. Suppose the Markov chain is in state S. We randomly choose a move of type i , which transforms S to S' with proposal probability $q_i(S \to dS')$. The new state S' is then accept with probability based on the Metropolis-Hastings method,

$$a(S \to dS') = \min\left(1, \frac{E(S')q_i(S' \mid S)}{E(S)q_i(S \mid S')}\right). \tag{5.24}$$

Given current candidate S with state $S = (x_l, x_r, y_{lt}, y_{lb}, y_{rt}, y_{rb})$, all parameters change simultaneously and each parameter has equal chance to update. The speed of a Markov Chain depends critically on the design of its proposal probabilities in the jump. If we choose uniform distributions, it is equivalent to blind search and Markov chain will experience exponential waiting time before each jump. The proposal probability $q(s)$ should be very close to $E(S)$ within the search space. Therefore, we must seek approximations and this is where the data-driven methods step in. In data-driven MCMC, the proposal probability $q_i(S \to dS')$ is changed to $q_i(S' \mid S, I)$ and the new state S' is then accept with probability

$$a(S \to dS') = \min\left(1, \frac{E(S')q_i(S' \mid S, I)}{E(S)q_i(S \mid S', I)}\right) \tag{5.25}$$

$q_i(S' \mid S, I)$ indicates that we can draw new parameters according to some important cues in the image. As we mentioned in the previous section, doors appear more frequently in the image at the position close to the vertical lines which are long enough. This cue could be used to guide the search of x_r, x_l. Then the proposal probability $q_i^x(S' \mid S, I)$ for sampling x-coordinates of x_r, x_l is taken as:

$$q_i(x' \mid x, I) = q(x \mid l)q(l) \tag{5.26}$$

where

$$q(x \mid l) = -\frac{1}{2\pi\delta_x} \exp\left\{-\frac{(x' - x^*)^2}{2\delta_x^2}\right\} \tag{5.27}$$

$q(l)$ is the probability to choose the vertical lines in the image. We simply sample the vertical lines from a uniform distribution. x^* is the x-coordinate of the sampled vertical line.

Because the cameras are low to the ground, the top of the door (the lintel) is often occluded or a horizontal line L_t closest to the top of the image. The bottom of the door is often close to the wall/floor boundary L_f. We use these cues to speed up the jumps of $y_{lt}, y_{lb}, y_{rt}, y_{rb}$. Let y_k^+ be the y-coordinates of the intersection of L_t and ℓ_l, ℓ_r, and y_k^- be the y-coordinates of the intersection of L_f and ℓ_l, ℓ_r, where

$k \in \{l, r\}$. Then the proposal probability $q_i^y(S' \mid S, I)$ for sampling $y_{lt}, y_{lb}, y_{rt}, y_{rb}$ is taken as:

$$q_i(y' \mid y, I) = -\frac{1}{2\pi\delta_y} \exp\left\{-\frac{(y' - y^*)^2}{2\delta_y^2}\right\} \tag{5.28}$$

where $y^* = y_k^+, k \in \{l, r\}$ for updating y_{lt}, y_{rt} and $y^* = y_k^-, k \in \{l, r\}$ for updating y_{lb}, y_{rb}. $y_k^+ = 0$ if door is lintel occluded.

When the algorithm rejects proposals by a certain times consecutively, we stop the algorithm and take the current proposal as the door detected.

All the operations are stochastic, thus the Markov chain designed in this way is ergodic and aperiodic, i.e., the Markov chain can travel between any state S_i and state S_j in a finite number of steps. This ensures that the chain can reach the maximum point in the proposal space.

After one proposal is finally determined as a door, our algorithm steps forward for detecting the next door. The image zone of the detected door will not be searched for detecting the next door. The detection will stop when the score of the door candidate is lower than a threshold.

5.6 Acquiring door/wall color model by training

As described above in this section, color is one of the weak classifiers in our Ababoost-based door detection system. We need to estimate the color histogram of the wall in advance so that we can compare with the color histogram of the door candidates. We have developed three methods, either of which can automatically distinguish wall/door color in an unknown environment.

Method 1: absolute width of door.

The width of a door is usually within a range from 0.7 m to 1.1 m, which is an important cue to locate a door. To calculate the width, the camera is roughly calibrated by a simple method first. We put a piece of A4 paper on the floor. One of the corner of the paper is set as the origin of 2D world coordinate system. Since the size of the paper is known, the coordinates (x, y) of four corners of the paper in the world coordinate system are available. Let's set them (0, 0), (B, 0), (0, C) and (B, C), respectively. Similarly, the four corresponding points on the image plane are set as (0, 0), (b, 0), (0, b) and (b, c), respectively. The homography H between the image plane and the floor plane can be estimated using the four correspondences by Direct Linear Transformation (DLT) [41]. Therefore, the absolute distance of any two points on the floor can be computed. Suppose L_f is the line of intersection of wall and floor and P_i, P_j are the intersections of L_f and the two vertical lines, L_i and L_j, of door candidates. If the distance between the two points, P_i and P_j, are within the range of the typical door width from 0.7 m to 1.1 m, the area between L_i and L_j mostly like belongs to a door and the color between them is mostly like the color of doors. Otherwise it could be wall if this area is untextured.

Method 2: relative width of door

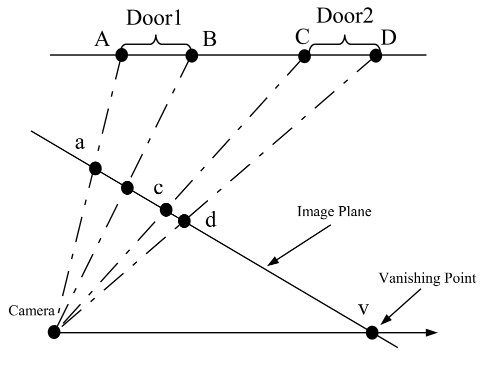

Figure 5.9: Relative width of door. A geometric construction to determine widths of doors given the vanishing point

Generally, doors have similar widths in an environment. In other words, if we can find four vertical lines intersecting with floor and the distances between two of them are similar, the four vertical lines most likely belong two doors. Here we develop a simple algorithm which can approximately distinguish doors from their surroundings without calibrating the camera.

As shown in Figure 5.9, (A, B) (C, D) are the intersection points of the floor and the vertical lines of door 1 and door 2 respectively, (a, b) and (c, d) are the corresponding points on the image plane. Given the vanishing point, the relative width of door 1 and door 2 can be computed with Algorithm: `DoorWidth`

Algorithm: `DoorWidth`

1. Set the origin of the 1D world coordinate system at **A**. Then points **A B C D** can be represented as coordinates 0, B, C, D and homogeneous (0, 1), (B, 1), (C, 1) and (D, 1). The vanishing point **V** can be represented as homogeneous (1, 0).
2. Similarly, set the origin of the 1D image coordinate system at **a**. Then points **a b c d** can be represented as coordinates 0, b, c, d and homogeneous as (0, 1), (b, 1), (c, 1), and (d, 1). The vanishing point **v** can be represented as coordinates v and homogeneous (v, 1).
3. There is a 2×2 1D prospective transformation H_{2x2} mapping $\mathbf{a} \rightarrow \mathbf{A}$, $\mathbf{b} \rightarrow \mathbf{B}$ $\mathbf{c} \rightarrow \mathbf{C}$ and $\mathbf{d} \rightarrow \mathbf{D}$. Compute the H_{2x2} by mapping $\mathbf{a}(0,1) \rightarrow \mathbf{A}(0,1)$ and $\mathbf{v}(v,1) \rightarrow \mathbf{V}(1,0)$,
$$H_{2x2} = \begin{bmatrix} \frac{1}{v} & 0 \\ -\frac{1}{v} & 1 \end{bmatrix}$$
4. The b is known. Therefore, B = H_{2x2}b. Similarly, C and D can be calculated.
5. The relative widths of the two doors are B and D - C, respectively. If B $\approx$ D - C, (A B) and (C D) construct two doors.

First of all, we find two door candidates by Algorithm: `DoorWidth`. Second, the result will be verified by checking the similarity of color between them and the cross ratio between **a b c** and **d**. The two candidates will be considered as doors if their color are almost same and the cross ratios keep consistent as the robot moves. Note that the cross ratio is used to verify that the A B C D are collinear. The part between the two doors is considered as wall.

Method 3: pre-detection without color

We run our door detection algorithm initially without color classifier. The area between two vertical lines which has the most features detected (concavity, bottom gap, ...) could be a door. And an untextured area which has the least features detected could be a wall.

To make the detection more reliable for the three methods, we use an image sequence instead of a single image for acquiring the color model. Throughout the sequence, each potential door/wall color histogram is stored. The final door/wall color model is determined by averaging the major color.

5.7 Open door

The detection of open doors is different from that of closed doors because some features for the closed door are not available. Figure 5.10 lists four types of typical views of open doors. Generally, open doors have at least one or more features as follows:

- **Different colors inside and outside**. As seen in Figure 5.10, colors of floors inside and outside of Door A, C, D are different. As shown in Figure 5.11b, L_2 is detected as the boundary between inside and outside regions. If the L_2 is not available, (in this case, inside and outside regions have the same color), the extension of the intersection line of the wall and the floor L_f will be used as the boundary.

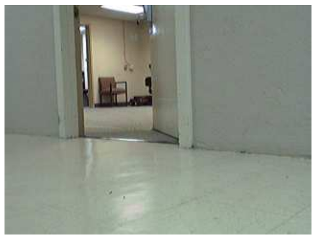
Door A

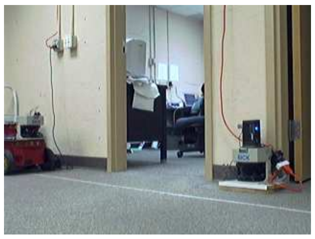
Door B

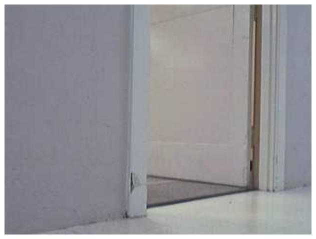
Door C

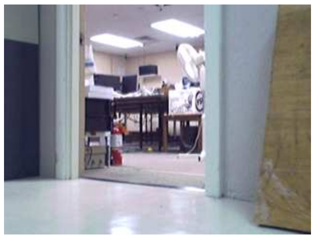
Door D

Figure 5.10: Typical open doors

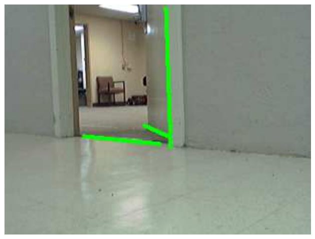
(a)

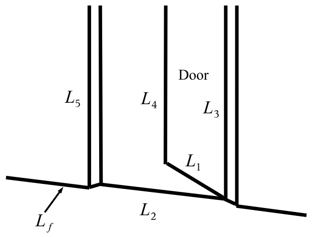

(b)

Figure 5.11: Three intersection lines: the bottom line L_1 of the door board, one of the vertical line L_3 of a door and a horizontal line L_2 of a corridor. L_f is the intersection line of the wall and the floor. L_4 is another vertical line of the door board.

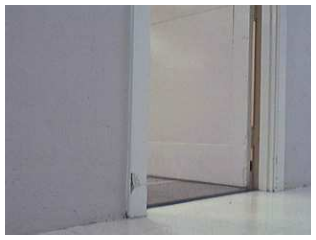
frame 68

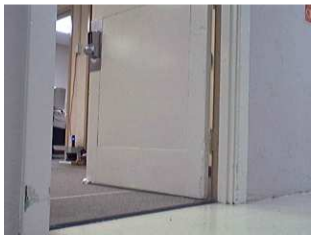
frame 181

Figure 5.12: The door area changed from untextured to textured as the robot moves

- **Textured area**. As seen in Figure 5.10, areas of insides of Door A B D contain significant texture. As seen in Figure 5.12, the door area for Door C changes from untextured to textured as the robot moves over time.

- **Three intersection lines**. As seen in Figure 5.11, there are three lines intersecting in one point; the bottom line of the door board L_1 , the vertical line L_3 of the door, and the horizontal line L_2 of the corridor. This case can be seen for Door A and C. To decrease the false positive, the following rules have to be satisfied:

  - the angle between L_2 and L_f should be smaller than the angle between L_1 and L_f.
  - another vertical line L_4 should either exist (Door A) or overlap with one of the door post (Door C).
  - area between L_1, L_3 and L_4 should be untextured.

- **non-coplanar**. For an open door, we assume that both posts of the door as well as the areas near the posts are within a plane, which we call post plane, while the region between the two posts is located in a different plane. Given two consecutive image frames, there is a homography mapping the two post planes. Therefore, any corresponding points or lines on the two post planes should satisfy the homography, while any corresponding points or lines between the two posts should not satisfy the homography. The homography is computed by the normalized extended DLT algorithm [29]. This algorithm uses both point and line correspondences such that it improves the homography results. The algorithm is briefly described in Algorithm: `Homography`. We use joint feature tracking [13] to obtain point correspondences between images. Using those feature points on the lines, line correspondences are acquired by least squares line fitting. Due to the possible errors from the tracker and approximation errors in computing H, the matrix H cannot be estimated by simply fitting a model to all the features. Instead we apply the random sample consensus (RANSAC) algorithm [32] to find small groups of points/lines with consistent motion. We repeatedly select a total of 4 random points/lines from among the areas near the posts, enforcing a minimum distance between the points to ensure that they are well spaced in the image. From these features we use Algorithm: `Homography` to calculate the homography H, which is then applied to all the features near the posts to record the number of inliers. This process is repeated several times, and the homography H with the largest number of inliers is taken to be the homography for the post plane.

5.8 Door tracking

Our tracking method is based on the detection of the doors. The detection of doors and vertical lines are taken as inputs for the tracker. We track the doors by data association, i.e., matching the predicted door hypotheses with the detection responses, whenever corresponding detection responses can be found. We match the hypotheses with the door detection responses first, as they are more reliable than the responses of the individual parts. If for a hypothesis no detection response with similar appearance and close to the predicted position is found, then we try to associate it with vertical line tracking. We match vertical lines by applying joint feature tracking [13] to track points on the lines of the previous image and least squares line fitting to hypothesize the lines in the current image.

Doors are detected frame by frame. In order to decide whether two responses, d1 and d2, from different frames belong to one door, a similarity measure is defined

Algorithm: `Homography`

Given n 2D to 2D point correspondences $\mathbf{x}_i \leftrightarrow \mathbf{x}'_i$ and m 2D to 2D line correspondence $\mathbf{l}_i \leftrightarrow \mathbf{l}'_i$, $m + n > 4$, determine the 2D homography matrix H.

1. Compute a transformation T that maps points $\mathbf{x}_i$ to $\tilde{\mathbf{x}}_i$ such that the centroid of the points $\tilde{\mathbf{x}}_i$ is the coordinate origin and the average distance from the origin is $\sqrt{2}$, where

$$T = \begin{bmatrix} s & 0 & t_x \\ 0 & s & t_y \\ 0 & 0 & 1 \end{bmatrix}$$

2. Transform lines $\mathbf{l}_i = (a, b, 1)$ to $\tilde{\mathbf{l}}_i$,

$$\tilde{\mathbf{l}}_i = s \begin{pmatrix} a \\ b \\ s - t_x a - t_y b \end{pmatrix}$$

3. Similarly, computer a transformation T' by repeating step 1 and step 2 mapping points $\mathbf{x}'_i$ to $\tilde{\mathbf{x}}'_i$ and transform lines $\mathbf{l}'_i$ to $\tilde{\mathbf{l}}'_i$.

4. Construct matrix A^p_i by points $\tilde{\mathbf{x}}_i = (x_i, y_i, 1)$ and points $\tilde{\mathbf{x}}'_i = (x'_i, y'_i, 1)$, $A^p_i =$

$$\begin{bmatrix} -x_i & -y_i & -1 & 0 & 0 & 0 & x'_i x_i & x'_i y_i & x'_i \\ 0 & 0 & 0 & -x_i & -y_i & -1 & y'_i x_i & u'_i y_i & y'_i \end{bmatrix}$$

5. Construct matrix A^l_i by lines $\tilde{\mathbf{l}}_i = (a_i, b_i, 1)$ and lines $\tilde{\mathbf{l}}'_i = (a'_i, b'_i, 1)$, $A^l_i =$

$$\begin{bmatrix} -a'_i & 0 & a'_i a_i & -b'_i & 0 & b'_i a_i & -1 & 0 & a_i \\ 0 & -a'_i & a'_i b_i & 0 & -b'_i & b'_i b_i & 0 & -1 & b_i \end{bmatrix}$$

6. Stack A^p_i on top of A^l_i to give a matrix A. Solve equation $A\mathbf{h} = 0$ by Singular Value Decomposition (SVD) to get $\mathbf{h}$, and $H = \begin{bmatrix} h_{11} & h_{12} & h_{13} \\ h_{21} & h_{22} & h_{23} \\ h_{31} & h_{32} & h_{33} \end{bmatrix}$.

Figure 5.13:

as the following likelihood mode:

$$S(d1, d2) = S_{pos}(d1, d2) S_{size}(d1, d2) S_{color}(d1, d2), \tag{5.29}$$

where S_{pos} , S_{size}, and S_{color} are affinities based on position, size, and color of two detection responses respectively. Their definitions are

$$S_{pos}(d1, d2) = \eta_{pos} \texttt{exp} \left[-\frac{(x_1 - x_2)^2}{\sigma_x^2} \right] \texttt{exp} \left[-\frac{(y_1 - y_2)^2}{\sigma_y^2} \right], \tag{5.30}$$

$$S_{size}(d1, d2) = \eta_{size} \texttt{exp} \left[-\frac{(x_1 - x_2)^2}{\sigma_x^2} \right], \tag{5.31}$$

$$S_{color} = \frac{\sum_{i=1}^{N} \min(\phi_1[i], \phi_2[i])}{\sum_{i=1}^{N} \phi_1[i]} \tag{5.32}$$

where $\phi_1[i]$ and $\phi_2[i]$ are the numbers of pixels in the ith bin of the histograms of two detection responses, respectively, and N is the number of bins. η_{pos} and η_{size} are normalizing factors.

We start to track a door when enough evidence is collected from the detection responses. If a door has T consecutive detection responses with $S(d1, d2)$ greater than a threshold, we start to track the door. For a new frame, for all existing doors, we first look for their corresponding detection responses in this frame. If there is a new detection response matched with a existing door, then the door location is updated with the detected door. Otherwise we match the $S(d1, d2)$ of the region between two tracked vertical lines with a existing door. If $S(d1, d2)$ is greater than a threshold, the door location is updated with the two tracked vertical lines. When a door detection responses are not found for consecutive T time steps, the tracking of the door is terminated.

5.9 Experimental results

To test the performance of the system, we created a database consisting of 577 door images. All the door images was taken in more than twenty different buildings exhibiting a wide variety of different visual characteristics. The images were taken by an inexpensive Logitech QuickCam Pro 4000 mounted about 30 cm above the floor on an ActivMedia Pioneer P3AT mobile robot. 100 images were used for training the algorithm. On the remaining 477 images, which were used for testing, the algorithm detects 90% of the doors with a false positive rate of 0.07 non-doors per image (on average) by MCMC and 86% of the doors with a false positive rate of 0.09 non-doors per image (on average) by DDMCMC. The algorithm was implemented in Visual C++ and runs at a speed of 5 frame/s on a 1.6 GHz Dell Inspiron 700m laptop computer.

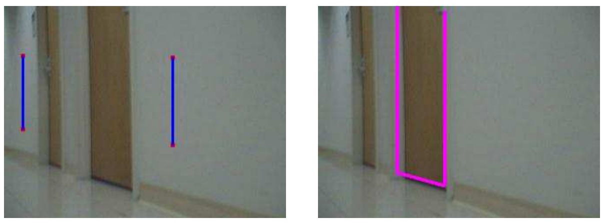

a) b)

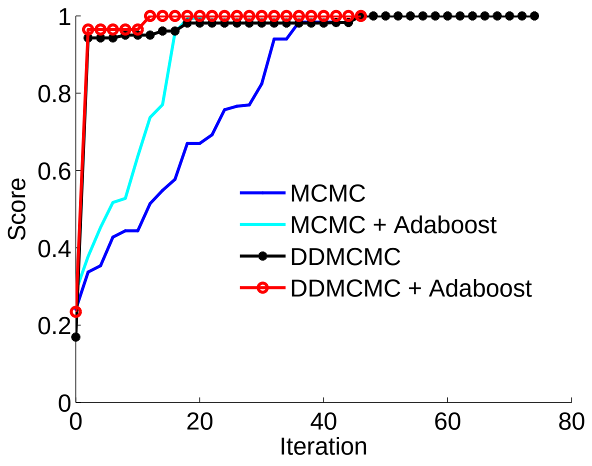

c)

Figure 5.14: Comparison of MCMC and DDMCMC with/without weighting to detect doors. Data are collected from testing in 10 typical images and averaged. See text for explanation.

We first show our working example on a simple image. We freely pick two vertical lines as an initial guess of a door as shown in Figure 5.14a. We detect the door by the traditional MCMC and the DDMCMC we proposed above, respectively. For MCMC, the door is searched with a uniform distribution over the image. Also, the cues of the door are either treated equally, i.e., α_i and β_j are set to 1, or weighted by Adaboost. The score E changes are shown in Figure 5.14c. We can see the DDMCMC achieves tremendous speedup in comparison to the traditional MCMC. Also we notice that the Adaboost weighting significantly increases the searching speed for the traditional MCMC. As for DDMCMC, the Adaboost weighting does not play an important role at first (scores both change from 0.8 to 0.08 in 2 iterations). That means DDMCMC with both weighted and un-weighted models can roughly find the door rapidly. However, afterward, the score searched by the DDMCMC with a weighted model can reaches the maximum faster than the DDMCMC with a un-weighted model. Also we note that since the score sharply drops with DDMCMC and almost reaches the maximum (from 0.8 to 0.08) in just 2 iterations. We might not have to search the entire solution space and completely maximize the score so that we can find a door even faster. Figure 5.15 compares the results. As shown in the top images, there is no significant difference between the two methods. However, as shown in the bottom images, DDMCMC with 90% maximized score is not able to precisely locate the door. In our experiments, DDMCMC with 90% maximized score can achiev almost the same results for around 90% images, and yet the speed is increased 30 times from 0.16 frames/s to 4.2 frames/s.

Figure 5.16 shows some typical doors detected by our system but unsuccessfully or incompletely detected by Adaboost algorithm [24]. Our approach can get better results because DDMCMC is able to explore the entire solution space and, thus, achieves a nearly global optimal solution, while the Adaboost-based algorithm [24] locates doors highly depending on the positions of the detected vertical lines. Line

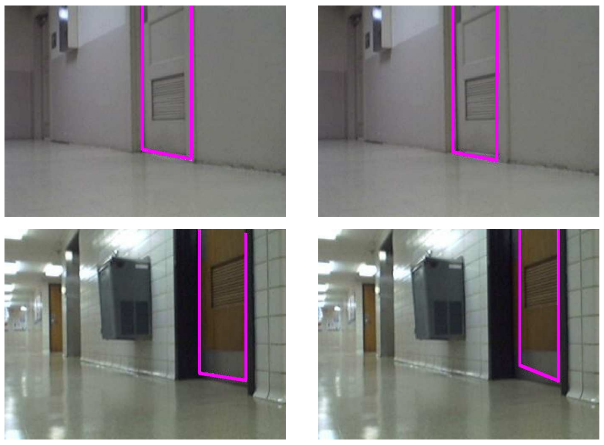

Figure 5.15: Comparison of DDMCMC. Left: score completely maximized. Right: score 92% maximized.

detection is not perfect. For example, in the first image in Figure 5.16, the vertical lines of the door are not completely detected resulting in an imprecise detection of the door. Table 5.1 displays the results of the MCMC and DDMCMC algorithm tested on our door database, compared with those of the earlier version [24] which is Adaboost based. The ground truth is totally 462 doors, which are labeled manually.

Algorithm	MCMC	DDMCMC	Adaboost
True Positive	430	407	392
False Positive	30	33	31

Table 5.1: MCMC and DDMCMC Vs. Adaboost-based algorithm. Detection results of the MCMC and DDMCMC algorithm, compared with Adaboost-based algorithm. The ground truth is 462.

Figure 5.17 shows some typical doors detected by our system. As can be seen, our algorithm is capable of detecting doors in the hallway under different illumination conditions and different viewpoints, with either the same color as the wall or a different color, even in a cluttered environment. The ROC curves of the methods with both MCMC and DDMCMC are shown in Figure 5.18. We also compared the performance of DDMCMC algorithm with and without calibration. The ROC curves

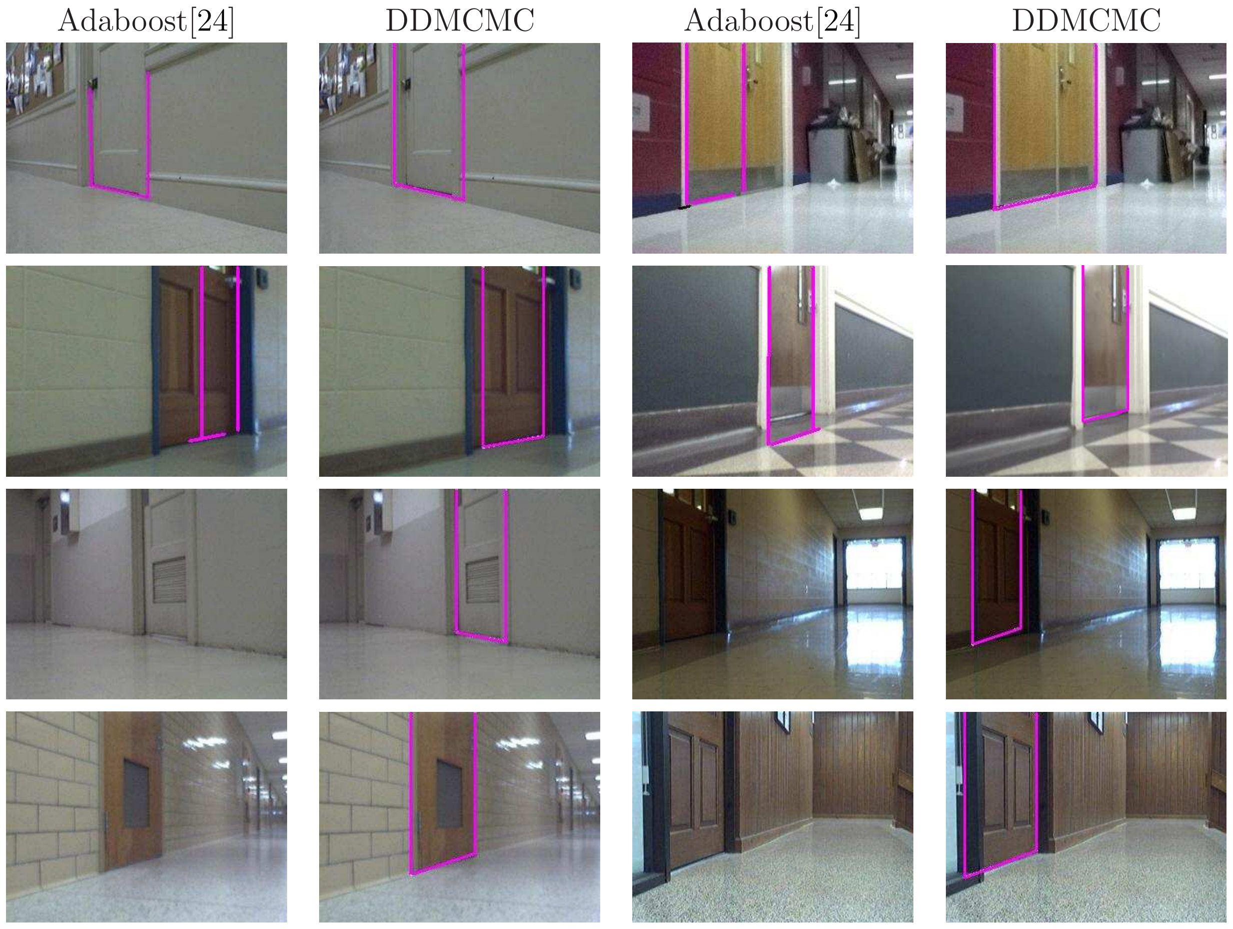

Figure 5.16: Our algorithm vs. Adaboost-based algorithm. Typical doors detected by our system but unsuccessfully or incompletely detected by Adaboost algorithm.

are shown in Figure 5.19. As can be seen, the calibrated system can achieve higher true positive rate and lower false positive rate. From the ROC curves of the individual features shown in Figure 5.20, it is clear that a significant improvement is achieved by combining all the features. Moreover, the features of color, width, concavity and gap below the door play an extremely important role compared with other features.

One question arises: are all the features necessary for door detection? Or can we use fewer features instead of all of them? Performances of feature combinations are tested to answer these questions. In order to simplify the experiments, we arrange the features by the importance according to the weights achieved from the Adaboost training as shown in Figure 5.21. Eight combinations are created. For example, K7 combination includes all the features except "kick plate" while K2 includes "width" and "concavity" only. The ROC curve in Figure 5.22 shows performances of feature combinations. The equal error rates (EERs) are drawn in Figure 5.23. As can be seen, the EERs of K5, K6, K7 are almost same (0.05). That means that feature "kick plate","vanishing point", and "texture" play unimportant roles in door detection. K5 (width + color + concavity + bottom gap + edge intensity) could achieve results good enough.

Of course, the system is not perfect, and some errors are shown in Figure 5.24 for completeness.

To demonstrate the utility of the algorithm, we used the robot shown in Figure 1.3 equipped with two webcams with diverging optical axes. As the robot moved down a corridor, doors were detected on both sides of the hallway by the algorithm by processing the images on-line. Doors were tracked from frame to frame. Doors that were not repeatedly detected a certain number of image frames were regarded as false positives and discarded.

Figure 5.25 shows the results of five trials in which the robot was manually driven along approximately the same path at a speed of $0.2\,m/s$ down a $40\,m \times 15\,m$ corridor with a 90-degree turn. 25 closed doors in the corridor were detected and tracked with 100% accuracy, that is, 5 detections out of 5 trials. A door partly occluded by water fountain is also detected and tracked. However, a cabinet was detected as two doors mistakenly because it really looks like a double door. Overall, the detection rate was 100% with a false positive rate of 0.008 per meter driven. Figure 5.26 shows some typical samples.

Figure 5.27 shows some typical open doors detected by our system and the ROC curve is shown in Figure 5.28.

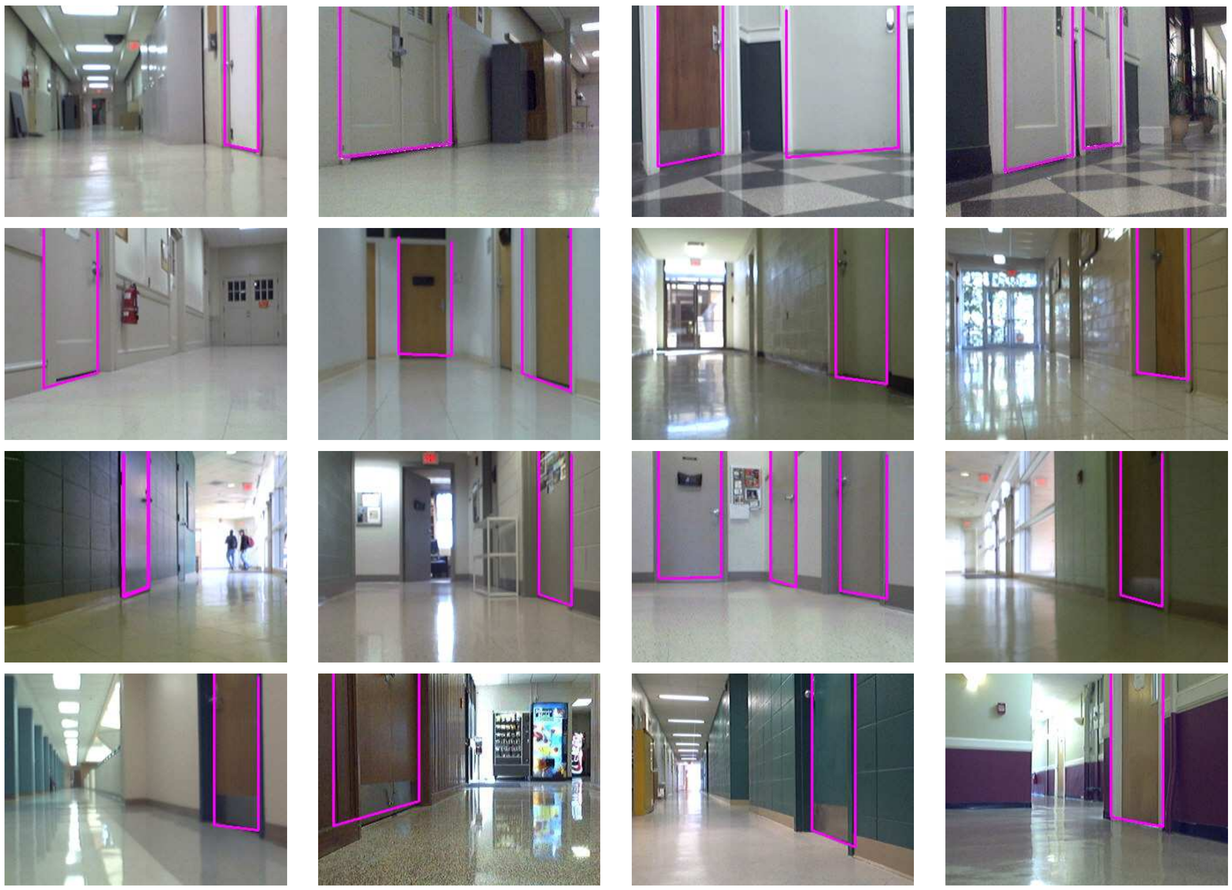

Figure 5.17: Examples of doors successfully detected by our algorithm. Note the variety of door widths, door and wall colors, relative pose of the door with respect to the robot, floor texture, and lighting conditions. Distant doors are not considered by the algorithm.

5.10 Summary

We have presented a vision-based door detection algorithm based on Data-Driven Markov Chain Monte Carlo (DDMCMC). Models of doors utilizing a variety of features, including color, texture, and intensity edges are presented. We introduce two novel geometric features that increase performance significantly: concavity and bottom-edge intensity profile. The Bayesian formulations are constructed and a Markov chain is designed to sample proposals. The features are combined using Adaboost to ensure optimal linear weighting. Doors are detected based on the idea

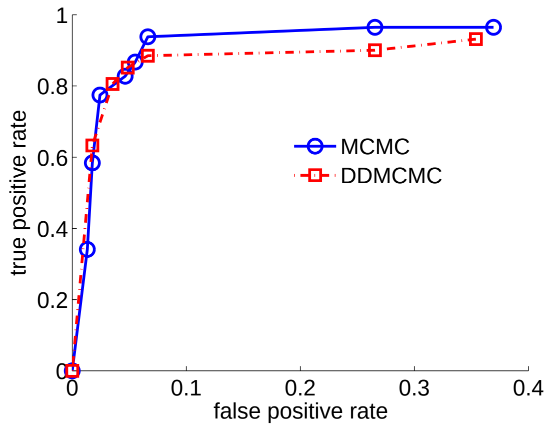

Figure 5.18: ROC curve of MCMC and DDMCMC. ROC curve showing the performance of the MCMC algorithm compared with the performance of the DDMCMC.

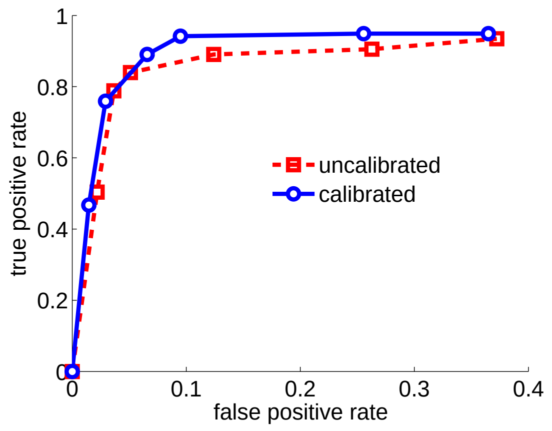

Figure 5.19: ROC curve of DDMCMC with and without calibration.

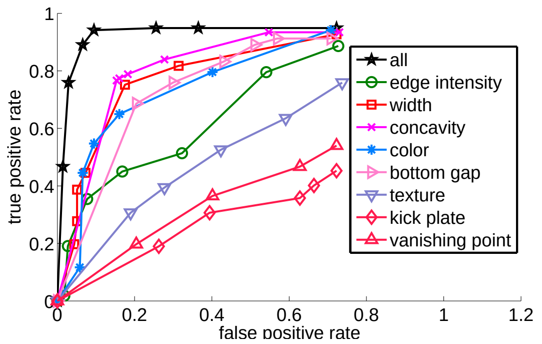

Figure 5.20: ROC curve with single-cue. ROC curve showing the performance of our algorithm compared with the performance of single-cue detectors.

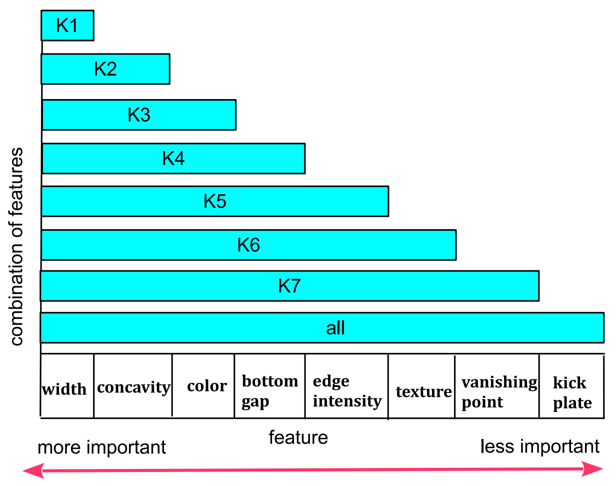

Figure 5.21: ROC curve showing performances of feature combinations

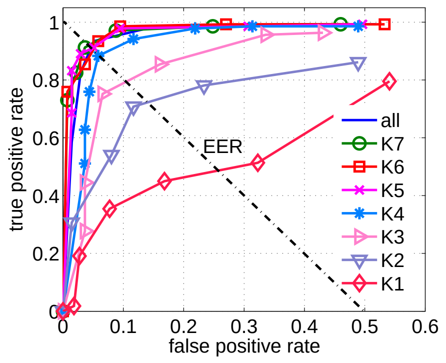

Figure 5.22: ROC curve of feature combinations and EERs. ROC curve showing performances of feature combinations and the equality error rates (EERs).

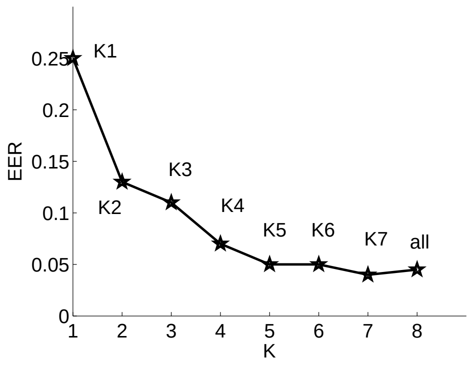

Figure 5.23: EERs versus feature combinations.

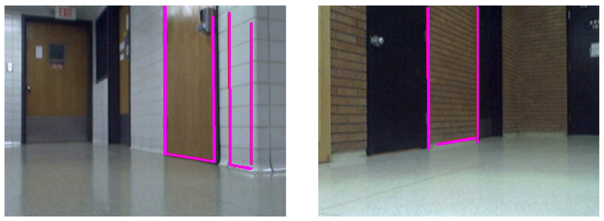

Figure 5.24: False negatives and positives. LEFT: One door is successfully detected, but another is missed due to lack of contrast along its bottom edge coupled with strong reflections on the floor; in addition a false positive occurs because of distracting horizontal edges. RIGHT: A dark door that is flush with the wall fails the concavity and bottom gap tests and hence is missed, while edges on the wall are erroneously detected.

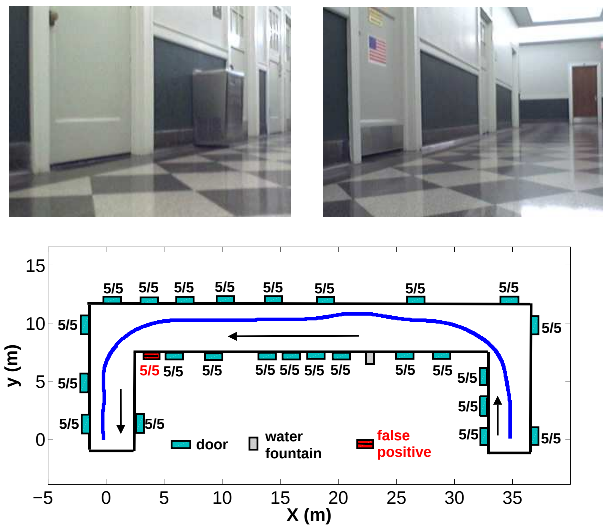

Figure 5.25: Two additional examples. TOP: Two images of the hallway environment near our laboratory. BOTTOM: 2D plan view of the hallway. Beside each door is indicated the number of detections / total number of trials.

of maximizing a posterior probability (MAP). Using the Monte Carlo technique, our algorithm is able to explore the complex solution space and, thus, achieves a nearly global optimal solution. Data-Driven techniques, such as edge detection, are used to compute importance proposal probabilities, which drive the Markov Chain dynamics and achieve speedup in comparison to the traditional jump diffusion methods. On a large database of images collected in a wide variety of conditions, the algorithm

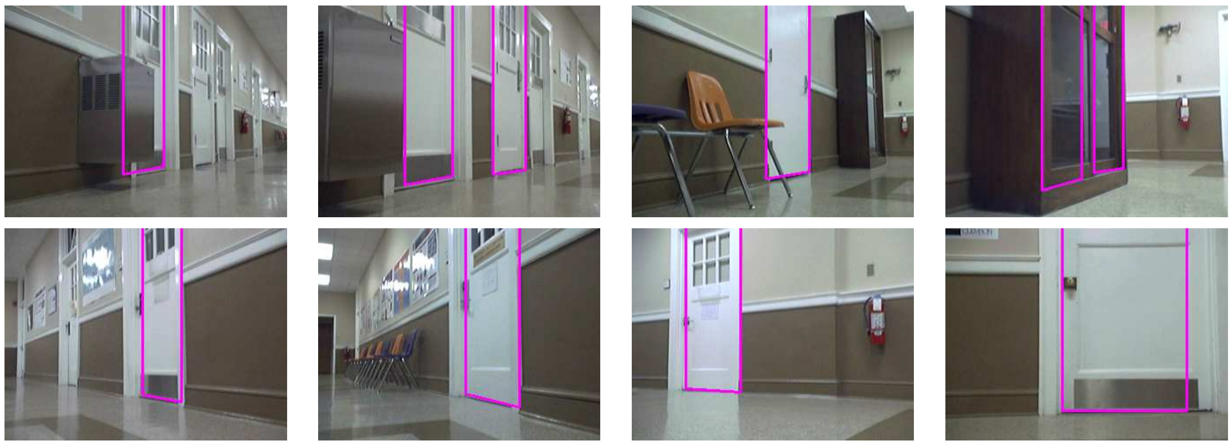

Figure 5.26: Door detection and tracking in a hallway.

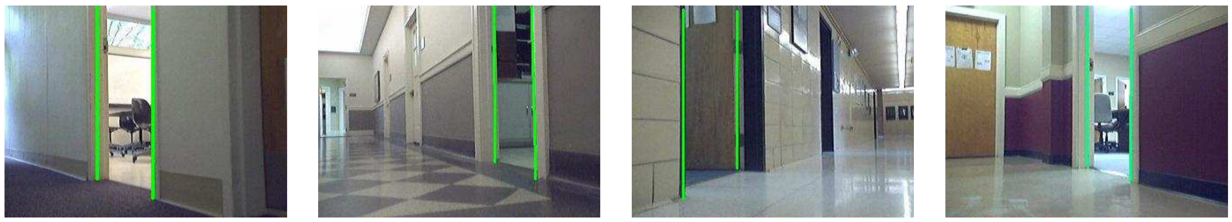

Figure 5.27: Detecting open doors.

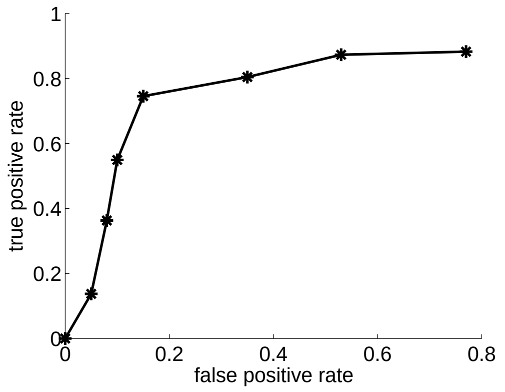

Figure 5.28: ROC curve of detecting open doors.

achieves more than 90% detection with a low false positive rate. Additional experiments demonstrate the suitability of the algorithm for real-time applications using a mobile robot equipped with an off-the-shelf camera and a laptop.

Chapter 6

Conclusion and Future work

The goal of this dissertation is to endow robots with visual capabilities in order to make them more autonomous. We proposed three algorithms involving three important areas in robotics: path following, person following, and door detection, to solve common problems in the real-world application of robot vision. For any mobile robot, navigating in its environment is one of the most important capabilities of all. Our research on path following for mobile robot navigation enables a mobile robot to determine its own position in its frame of reference and then to plan a path towards some goal location. Our research on person following is related to human-robot interaction study. The ability of a mobile robot to follow a person would benefit applications of using robot as a personal digital assistant in everyday life. Detection of doors is also one of the important capabilities for an autonomous robot, and will also benefit other robotics researches, such as building a geometric map in an indoor environment using doors as landmarks. For the path following, doors could also be used as significant landmarks in an untextured environment with fewer reliable feature points. In the future, the three algorithms could be integrated into a robot navigation system toward fully autonomous robot applications. For example, autonomous robot is highly desired in the hospital distribution service for decreasing operating costs while improving delivery performance. To meet the delivery needs of a hospital, any automated solution will need to handle routine deliveries as well as be flexible enough to handle arbitrary deliveries or other exceptions to the norm [76]. For routine pick-ups and deliveries, the robot follows a predefined route to deliver supplies to and from the service units. Beside routine deliveries, sometime the robot needs to deliver items to specific rooms. Therefore, door detection and recognition are required. For arbitrary deliveries, the robot could follow a hospital staff to deliver emergent supplies anywhere as required.

Chapter 1 opened with an introductory discussion to motivate and contextualize our research. The importance of vision-based mobile robot sensing was discussed, and it was concluded that vision sensing is one of the most powerful perception mechanisms for robotics. In addition a preview of our research was presented across the areas of path following, person following, and door detection. In Chapter 2 we moved on to discuss related work, and reviewed the application of computer vision in three areas above. Also discussed are some issues in their approaches. Then overviews of our approaches, and their advantages are described .

Map-based approaches to path following are using calibrated cameras in general. However, the camera has to be well calibrated and the ground is assumed locally planar and horizontal at the current position of the robot. Also they have to relate the image coordinates to world coordinates or image coordinates between image frames, which make solutions to path following complicated. In Chapter 3 we have developed a simple mapless approach to the problem using a single off-the-shelf camera with no calibration. The algorithm is qualitative in nature, requiring no map of the environment, no image Jacobian, no homography, no fundamental matrix, and no assumption about a flat ground plane.

Appearance-based approaches for person following have their limitations in real-world applications. The tracker is easily distracted by environment resulting in unreliable tracking. In Chapter 4 we have presented a Binocular Sparse Feature Segmentation (BSFS) algorithm for vision-based person following by fusing motion and stereo information. This system is able to reliably follow a person in complex dynamic, cluttered environments in real time.

Previous researches on door detection usually rely on range sensors or combine the range sensors with vision, and only a few of features (edges, color, or corners of door) are involved. Therefore, they are limited in handling a variety of challenging environmental conditions (changing pose, similarly colored doors and walls, strong reflections, and so forth). We believe that multiple vision cues are necessary for robustness. In Chapter 5 we have presented a solution to the problem based upon combining multiple cues. Our approach augments standard features such as color, texture, and vertical intensity edges with novel geometric features such as the concavity of the door and the gap below the bottom door edge. This algorithm can detect doors in a variety of challenging environmental conditions, achieving a nearly global optimal solution in many cases.

In this chapter, the three algorithms will be summarized. Their drawbacks and future work are also presented.

6.1 Path following

We have presented a novel approach to the problem of vision-based mobile robot path following using a single off-the-shelf camera. The robot navigates by performing a qualitative comparison of feature coordinates across the teaching and replay phases, utilizing the novel concept of a *funnel lane*. Vision information is combined with odometry for increased robustness. The algorithm does not make use of the traditional concepts of Jacobians, homographies, fundamental matrices, or the focus of expansion, and it does not require any camera calibration, including lens calibration. It only requires implicit calibration in the form of a controller gain. Experimental results on both indoor and outdoor scenes demonstrate the effectiveness of the approach on trajectories of hundreds of meters, along with its robustness to effects such as dynamic objects, slanted surfaces, and rough terrain. The versatility of the algorithm in working with wide-angle and omnidirectional cameras with only minor modification has also been shown.

The algorithm is not perfect, and there are scenarios in which it will fail. For example, occasionally the algorithm does not properly transition to the next milestone image, in which case the overlap between the current and milestone image can decrease to the point that an insufficient number of features are matched. Also, untextured scenes containing distant trees, bushes, or undecorated indoor hallways sometimes prevent the KLT algorithm from successfully tracking enough features to accurately compute the heading direction. While only a handful of features are necessary for the algorithm to succeed, it is important that features exist on both sides of the image, and that some number of features remain visible throughout the milestone.

Another source of error is due to distant features. Although features near the center of the image produce a narrow funnel lane even when they are far from the camera, distant features near the side of the image produce much larger funnel lanes which are less useful for navigation. Moreover, image parallax is inversely proportional to the distance to a feature. As a result, distant features are primarily useful for correcting the rotation of the robot and are quite incapable of informing the robot about minor translation errors. This problem is compounded by the inherent ambiguity between rotation and translation in the funnel lane itself. Even though this ambiguity has little effect when the robot is near the path, it hinders the ability of the visual information to correctly determine the correct amount of rotation when the robot has deviated significantly. Odometry helps to overcome this limitation, and we have conducted experiments in which the robot consistently returns to the path after deviating by several meters. However, much larger deviations either initially or during replay cannot be handled by our present system. At any rate, it should be noted that odometry drift is not an issue because we only store odometry values local to the segment, not in a global coordinate frame.

Because our system does not explicitly model the geometric world, its geometric accuracy is limited. Therefore, when compared with map-based approaches using calibrated cameras [78], the errors exhibited by the simple control scheme of our algorithm are rather large. Nevertheless, the remarkable flexibility and versatility of the system offer some important advantages over more precise techniques. With our approach, one can literally take an off-the-shelf camera, attach it to the robot, align it approximately in the forward direction, and start the system.

Since the algorithm depends on comparing scenes between the teaching and replay phase, it would fail if the scene changes significantly after teaching. For example, the robot is taught in a parking lot with a lot of cars parking there in the morning. And it would fail to repeat the learned path in the afternoon because most cars are gone. Future work should be aimed at incorporating higher-level scene knowledge to have the robot focus on those unchanged landmarks, such as buildings, by applying scene segmentation algorithm.

6.2 Person following

We have presented a novel algorithm, called Binocular Sparse Feature Segmentation (BSFS), for vision-based mobile robot person following. The algorithm detects and matches feature points between a stereo pair of images and between successive images in the sequence in order to track 3D points in time. Segmentation of the features is accomplished through a RANSAC-based procedure to estimate the motion of each region, coupled with a disparity test to determine the similarity with the target being tracked. The BSFS algorithm is augmented with the Viola-Jones face detector for initialization and periodic feature pruning.

This system does not require the person to wear a different color from the background, and it can reliably track a person in an office environment, even through doorways, with clutter, and in the presence of other moving objects. However, relying only upon sparse features makes the system subject to distraction by other objects with similar motion and disparity to the person being tracked. More robust performance could be achieved by fusing the information used by this algorithm with additional appearance-based information such as a template or other measure of image intensities or colors. Another limitation of the present system is its inability to handle the situation when the person leaves the field of view of the camera, or when another object completely occludes the person, in which case the robot tends to fixate on the distracting object. A pan-tilt camera or a wider field of view would overcome this problem. Finally, future should should be aimed at incorporating the proposed technique with other sensor modalities such as color information, infrared data, or range sensors to increase robustness [66].

6.3 Door detection

We have presented a vision-based door detection algorithm for robot navigation using an uncalibrated camera. The doors are detected by a camera mounted on a mobile robot, from which low vantage point the lintel is often not visible. Door candidates are first sought by detecting the vertical lines that form the door frame, and then by applying constraints such as size, direction, and distance between segments. Within these door candidates, several features are measured. The algorithm augments standard features such as color, texture, and vertical intensity edges with novel geometric features based on the concavity of the door and the gap below the bottom door edge. The features are combined in an Adaboost framework to enable the algorithm to operate even in the absence of some cues. Tested on a large database exhibiting a wide variety of environmental conditions and viewpoints, the algorithm achieves more than 90% detection rate with a low false positive rate. The approach is suitable for real-time mobile robot applications using an off-the-shelf camera, and preliminary experiments demonstrate the success of the technique.

There is plenty of room for future work in this area. Additional features can be incorporated into the Adaboost framework to increase performance. Calibration of the camera, along with 3D line estimation, would enable pose and distance measurements to facilitate the building of a geometric map. In addition, open and closed doors can be distinguished using motion information inside the door, specifically the motion parallax of features inside the room that are visible when the door is open. Finally, the algorithm will be integrated into a complete navigation system that is able to drive down a corridor and turn into a specified room.

Appendices

Appendix A

The Kanade-Lucas-Tomasi (KLT) Feature Tracker

In 1981, Lucas and Kanade [61] proposed a new optical estimation method that makes use of the spatial intensity gradient of the images to find a good match between two consecutive images. This method measures the sum of squared intensity differences between the past and current frame over fixed-size feature windows. The displacement is then iteratively determined by minimizing this sum using Newton-Raphson style minimization. In 1991, Tomasi and Kanade [95] improved the technique by proposing a more principled way to select good features for more reliable feature tracking. However, this method considered the image motion in 2D so that only a pure translation model is used during tracking, which results in false tracks for some "bad" features. In 1994, Shi and Tomasi [84] combined the pure tranlation-based motion model for feature tracking, with an affine-transformation-based motion model (linear warping and translation) for image matching. It was proved that false tracks could be reliably rejected by affine motion model. This is the well-known Kanade-Lucas-Tomasi (KLT) Feature Tracker. Since then, the KLT algorithm has become one of the most widely used techniques in computer vision to estimate the optical flow.

A.1 Feature tracking

Let I and J be two consecutive grayscaled images. A point or feature $\mathbf{x} = (x, y)$ measured with respect to a fixed-size window's center in J moves to point $A\mathbf{x} + \mathbf{d}$ in I, where A is a warp matrix which takes the pixel $\mathbf{x}$ in image J and maps it to image I and the displacement $\mathbf{d} = (d_x, d_y)$. Then

$$I(A\mathbf{x} + \mathbf{d}) = J(\mathbf{x}) + n(\mathbf{x}), \tag{A.1}$$

where $n(\mathbf{x})$ is noise. If we consider only a pure translation model, A is equal to the identity matrix. Then equation (A.1) becomes:

$$I(\mathbf{x} + \mathbf{d}) = I(\mathbf{x}) + n(\mathbf{x}), \tag{A.2}$$

The problem of feature tracking is determined by finding $\mathbf{d}$ that minimize the residue error over the given window W:

$$\epsilon = \int_W \left[I(\mathbf{x} + \mathbf{d}) - J(\mathbf{x})\right]^2 w(\mathbf{x}) d\mathbf{x}, \tag{A.3}$$

where w is a weighting function. In the simplest case, $w(\mathbf{x})$ could be set to 1. Alternatively, w could be a Gaussian-like function, to emphasize the central area of the window. When the displacement vector is small, $J(\mathbf{x} + \mathbf{d})$ can be approximated by its Taylor series truncated to the linear term: [61]

$$I(\mathbf{x}+\mathbf{d}) \approx I(\mathbf{x}) + d_x \frac{\partial I}{\partial x}(\mathbf{x}) + d_y \frac{\partial I}{\partial y}(\mathbf{x}) \tag{A.4}$$

Differentiating the last expression of the residue ϵ in equation (A.3) with respect to $\mathbf{d}$:

$$\begin{aligned}\frac{\partial \epsilon}{\partial \mathbf{d}} &= 2\int_W [I(\mathbf{x}+d) - J(\mathbf{x})] \left[\frac{\partial I(\mathbf{x}+\mathbf{d})}{\partial \mathbf{d}} - \frac{\partial J(\mathbf{x})}{\partial \mathbf{d}}\right] w(\mathbf{x}) d\mathbf{x} \\ &\approx 2\int_W [I(\mathbf{x}) - J(\mathbf{x}) + \mathbf{g}\mathbf{d}]\, \mathbf{g} w(\mathbf{x}) d\mathbf{x},\end{aligned}$$

where $\mathbf{g} = (g_x, g_y) = \left(\frac{\partial}{\partial x} I(\mathbf{x}), \frac{\partial}{\partial y} I(\mathbf{x})\right)$. To find the displacement $\mathbf{d}$, the derivative is set to zero:

$$\int_W [I(\mathbf{x}) - J(\mathbf{x}) + \mathbf{g}\cdot\mathbf{d}]\, \mathbf{g} w(\mathbf{x}) d\mathbf{x} = 0, \tag{A.5}$$

Rearranging terms, we get

$$\left(\int_W \mathbf{g}\mathbf{g}^T w(\mathbf{x}) d\mathbf{x}\right) \mathbf{d} = \int_W (J(\mathbf{x}) - I(\mathbf{x}))\mathbf{g} w(\mathbf{x}) d\mathbf{x} \tag{A.6}$$

which can be rewritten as

$$G\mathbf{d} = \mathbf{e}, \tag{A.7}$$

where $G = \begin{bmatrix} g_{xx} & g_{xy} \\ g_{xy} & g_{yy} \end{bmatrix}$ is the following 2 X 2 symmetric coefficient matrix,

$$G = \int_W \mathbf{g}\mathbf{g}^T w(\mathbf{x}) d\mathbf{x} = \sum_W \begin{bmatrix} g_x^2 & g_x g_y \\ g_x g_y & g_y^2 \end{bmatrix} \tag{A.8}$$

and $\mathbf{e}$ is the following 2×1 error vector:

$$\mathbf{e} = \int_W (J(\mathbf{x}) - I(\mathbf{x}))\mathbf{g}w(\mathbf{x})d\mathbf{x}. \tag{A.9}$$

For every pair of adjacent frames, the matrix G can be computed from one frame, by estimating gradients and computing their second order moments. The vector e, on the other hand, can be computed from the difference between the two frames, along with the gradient computed above. The displacement $\mathbf{d}$ is then the solution of equation (A.7). The solution $\mathbf{d}$ to equation (A.7) will usually contain some error. In practice, equation (A.7) is repeatly solved and $\mathbf{x}$ is updated as shown in equation (A.10) at each iteration until $\mathbf{d}$ is less than an accuracy threshold.

$$\mathbf{x} \leftarrow \mathbf{x} + \mathbf{d} \tag{A.10}$$

In general, d_x, d_y could not be integers during iteration. In order to achieve high tracking accuracy, bilinear interpolation [15] is used to compute image value at locations between integer pixels. Let α and β be the two remainder values (between 0 and 1) such that:

$$x = x_0 + \alpha \tag{A.11}$$

$$y = y_0 + \beta \tag{A.12}$$

then,

$$\begin{aligned} I(x, y) &= (1-\alpha)(1-\beta)I(x_0, y_0) + \alpha(1-\beta)I(x_0+1, y_0) + \\ &\quad (1-\alpha)\beta I(x_0, y_0+1) + \alpha\beta I(x_0+1, y_0+1). \end{aligned} \tag{A.13}$$

A.2 Feature Detecting

A feature point can be tracked only if the equation (A.7) can be solved reliably. That requires the 2×2 coefficient matrix G must be both above the image noise level and well conditioned. Tomasi and Kanade [95] pointed out that this requirement can be satisfied if both eigenvalues λ_1, λ_2 of G are large enough, i.e.

$$\min(\lambda_1, \lambda_2) > \text{threshold}. \tag{A.14}$$

Two small eigenvalues mean the window belongs to a relatively uniform area and it's hard to extract useful motion information. A large and a small eigenvalue usually means the window is on a straight line and suffers from so called "aperture problem". Two large eigenvalues can represent corners or any other highly textured regions that can be tracked reliably. Since $G = \begin{bmatrix} g_{xx} & g_{xy} \\ g_{xy} & g_{yy} \end{bmatrix}$, the eigenvalues are calculated by

$$\lambda = \frac{1}{2}\left[(g_{xx} + g_{yy}) \pm \sqrt{(g_{xx} - g_{yy})^2 + 4g_{xy}^2}\right] \tag{A.15}$$

To avoid redundant tracking, the minimum distance is enforced so that distance between any pair of selected features is larger than a given threshold, 5 - 10 pixels usually.

A.3 Dissimilarity checking

Although the KLT algorithm proposes a criterion, which is optimal by construction, to select good features for tracking, bad features are still often selected due to the complexities of environments. Actually, even a region with rich texture content might be poor. For instance, boundaries of different surfaces in the world could intersect each other in the image and then produce "bad" feature points, which actually correspond to no physical points. Also the standard KLT algorithm typically relies on a constant scene appearance over all view points. This fundamental assumption is violated for complex environments containing reflections and semi-transparent surfaces. Since the feature residue error, sometimes called feature dissimilarity, qualifies how much the appearance of a feature changes, it has to be well measured so that "bad" features can be properly removed during tracking. Shi and Tomasi [84] pointed out that the pure translation mode is not adequate for image motion when measuring dissimilarity, but affine warping is adequate. Their approach is briefly described as follows.

Consider an affine motion model, the warping matrix A becomes:

$$A = I + D \tag{A.16}$$

where I is the identity matrix and D is the deformation matrix:

$$D = \begin{bmatrix} D_{xx} & D_{xy} \\ D_{yx} & D_{yy} \end{bmatrix} \tag{A.17}$$

Then equation (A.3) that measures the residue error can be replaced by

$$\epsilon = \int_W \left[I(A\mathbf{x} + \mathbf{d}) - J(\mathbf{x}) \right]^2 w(\mathbf{x}) d\mathbf{x}, \tag{A.18}$$

Differentiate it with respect to $D_{xx}, D_{xy}, D_{yx}, D_{yy}$ and $\mathbf{d}$ and set the result to zero, we have:

$$T\mathbf{z} = a, \tag{A.19}$$

where T is the following coefficient matrix:

$$T = \int_W \begin{bmatrix} x^2 g_x^2 & x^2 g_x g_y & xy g_x^2 & xy g_x g_y & x g_x^2 & x g_x g_y \\ x^2 g_x g_y & x^2 g_y^2 & xy g_x g_y & xy g_y^2 & x g_x g_y & x g_y^2 \\ xy g_x^2 & xy g_x g_y & y^2 g_x^2 & y^2 g_x g_y & y g_x^2 & y g_x g_y \\ xy g_x g_y & xy g_y^2 & y^2 g_x g_y & y^2 g_y^2 & y g_x g_y & y g_y^2 \\ x g_x^2 & x g_x g_y & y g_x^2 & y g_x g_y & g_x^2 & g_x g_y \\ x g_x g_y & x g_y^2 & y g_x gy & y g_y^2 & g_x g_y & g_y^2 \end{bmatrix} w(\mathbf{x})\, d\mathbf{x}, \qquad \text{(A.20)}$$

and e is the following error vector:

$$a = \int_W (J(\mathbf{x}) - I(\mathbf{x})) \begin{bmatrix} x g_x \\ x g_y \\ y g_x \\ y g_y \\ g_x \\ g_y \end{bmatrix} w(\mathbf{x})\, d\mathbf{x}, \qquad \text{(A.21)}$$

and $\mathbf{z} = (D_{xx}, D_{xy}, D_{yx}, D_{yy}, d_x, d_y)^T$

Is affine motion model more reliable to apply for tracking? Many people have made that observation that it's actually worse than pure translation model. In fact, the reason is that affine tracking requires to estimate a very large number of parameters: 6 instead of 2 for the pure translation model, therefore more error would be introduced. Another reason might lie in the size of the feature window. The quality of the tracking depends on the size of the feature window. Small windows are preferable for tracking because they are more likely to contain features at similar depths. However, when the window is small, the deformation matrix D is harder to estimate, because the variations of motion within it are smaller and therefore less reliable.

Since motion between adjacent frames is small during tracking, the affine deformation D of the feature window is likely to be the zero matrix. A pure translation model is thus good enough for tracking while affine motion should only be considered for building a reliable rejection scheme. During tracking, the equation (A.19) is solved and the results are used for calculating the dissimilarity by equation (A.18). If the dissimilarity of the tracked feature point is larger than a threshold, the point is declared "lost".

A.4 Pyramidal Implementation

Tracking feature by minimizing the residue error is an ill-posed problem, since the optimum might be attained by many dissimilar displacement fields. When motions between two successive frames are larger than one pixel, the minimization algorithm could easily be trapped in a local minimum.

In order to find the global minimum to support large motion and for improved accuracy, it is useful to apply multiscale coarse-to-fine approach: displacement can be estimated at the coarsest level of a pyramid, where the image is significantly blurred, and the velocity is much slower. The coarse solution is then used as initial guess for the pixel displacement at a finer level of the pyramid. This coarse-to-fine estimation continues until the finest level of the pyramid (the original image) is reached. The pyramid height L_m should be picked appropriately according to the maximum expected optical flow in the image. Each level L of the pyramid is the downsampling by 2 from the beneath level $L-1$ after a low pass filter used for image anti-aliasing.

In 1999, Bouguet [15] proposed a implementation which can be found in the OpenCV library. Let $I^0 = I$ be the 0th level image, the highest resolution image, $L = 1, 2, ...L_m$ be a pyramidal level. Denote I^L the image at level L. The image I^L is then defined as

$$\begin{aligned} I^L(x,y) &= \frac{1}{4} I^{L-1}(2x,2y) + \\ & \frac{1}{8}\left(I^{L-1}(2x-1,2y) + I^{L-1}(2x+1,2y)\right) + \\ & \frac{1}{8}\left(I^{L-1}(2x,2y-1) + I^{L-1}(2x,2y+1)\right) + \\ & \frac{1}{16}\left(I^{L-1}(2x-1,2y-1) + I^{L-1}(2x+1,2y+1)\right) + \\ & \frac{1}{16}\left(I^{L-1}(2x+1,2y-1) + I^{L-1}(2x-1,2y+1)\right). \end{aligned} \tag{A.22}$$

Let $\mathbf{d}^L$ be the displacement computed at level L, $\mathbf{d}^{L-1} = 2\mathbf{d}^L$. The solution of the displacement $\mathbf{d}$ for the original image is therefore:

$$\mathbf{d} = \sum_{L=0}^{L_m} 2^L \mathbf{d}^L, \tag{A.23}$$

A.5 Summary

The entire KLT tracking algorithm are summarized in a form of pseudo-code

.

Algorithm: `The Lucas-Kanade Algorithm:  detecting features`

Input: A grayscaled image I.
Output: A set of good feature points for tracking.

```
1. Calculate the gradient $\mathbf{g}$ of image $I$.
2. Calculate the $2 \times 2$ coefficient matrix $G$ for each pixel over a $5 \times 5$ window in $I$ by equation (A.8).
3. Calculate eigenvalues of $G$ by equation (A.15).
4. Select good features $\mathbf{x}$ by equation (A.14).
5. Enforcing a minimum distance (5-10 pixels usually) between features to avoid overlap.
```

Algorithm: `The Lucas-Kanade Algorithm:  tracking feature`

Input: Two successive grayscaled images I and J, a good feature point $\mathbf{x}$ in I.
Output: A corresponding feature point $\mathbf{x}'$ on J.

```
1. Build pyramid representations of images $I$ and $J$: $I^L, J^L, L = (0, 1, ...L_m)$, by equation (A.22).
2. Initialize $\mathbf{x}^L = \mathbf{x}/2^{L_m}$
3. For each level $L$ from $L_m$ down to 0,
   (a) Calculate the $2 \times 2$ coefficient matrix $G$ at $\mathbf{x}^L$ using pyramid $I^L$ by equation (A.8).
   (b) For iteration $K$ from 0 to $K_{max}$
       i. Calculate $I(\mathbf{x}^L)$, $J(\mathbf{x}^L)$ by bilinear interpolation using pyramid $I^L$ and $J^L$ by equation (A.13).
       ii. Calculate the 2 X 1 error vector $e$ at $\mathbf{x}^L$ by equation (A.9).
       iii. Solve equation (A.7) to compute the displacement $\mathbf{d}_k$.
       iv. Update $\mathbf{x}^L \Leftarrow \mathbf{x}^L + \mathbf{d}_k$.
       v. End iteration if $\mathbf{d}_k <$ accuracy threshold,
   (c) Calculate $\mathbf{x}^{L-1} = 2\mathbf{x}^L$ for the initial guess of next level.
4. Final location of point $\mathbf{x}'$ on $J$ is $\mathbf{x}^0$
5. Check residue error by equation (A.18). Declare "lost" if residue error is greater than a threshold.
```

Figure A.1:

Appendix B

Line Detection

To detect lines, intensity edges are first detected throughout the image using the Canny edge detector [20]. To group the edges into straight line segments, many existing approaches apply the Hough transform, but in our experiments we found this approach to be quite sensitive to the window size: Small windows cause unwanted splitting of lines, while large windows cause unwanted merging of lines.

Instead, we employ a modified form of the split-and-merge algorithm developed by Douglas and Peucker [28], which is shown as the algorithm `LineDetection`. In the first step, edge pixels are searched in order to label connected edges. Edges are divided by junction points, which are defined as edge pixels that are connected to more than two other pixels in their 8-neighborhood. Small isolated edges and spurs (short sequences of pixels jutting to the side of the main branch of the edge) are eliminated.

The second step divides the connected edges into sequences of straight line segments using a divide-and-conquer strategy. A straightness test is recursively applied to the edge, stopping when all segments pass the test. In Douglas and Peucker's algorithm, the threshold for the maximum allowed deviation $d_{allowed}$ is a constant, which mistakenly absorbs short line segments into long line segments and mistakenly divides long line segments into multiple short segments. Our modified version of the algorithm solves this problem by determining $d_{allowed}$ using a half-sigmoid function:

$$d_{allowed}(s) = \delta \left(\frac{\beta - e^{-|s|}}{\beta + e^{-|s|}} \right), \tag{B.1}$$

where $\mid s \mid$ is the length of segment s, δ is a constant specifying the value of $d_{allowed}$ for long segments, and $\beta > 1$ is a constant to increase the slope of the half-sigmoid function. This function is shown in Figure B.2, and the improvement from the modification is shown in Figure B.3.

Figure B.4a shows a typical result from this algorithm. Although straight line segments are found, several problems remain. For example, vertical lines corresponding to the door frame are often broken by door hinges or knobs. In addition, the reflection of the door creates spurious lines on the floor, often with a gap between the spurious lines and the true lines. To overcome these problems, we merge vertical lines separated by a small gap, discard lines that do not extend above the vanishing point, discard short lines, and retain only lines whose orientation is nearly vertical. The result of these tests is shown in Figure B.4b.

Algorithm: `LineDetection`

Input: Intensity edges of an image
Output: A set of straight line segments

1. *Edge labeling:* For each unlabeled edge pixel
    (a) Track edge to find the rest of the connected edge points and label them, stopping if a junction point is encountered
    (b) Eliminate isolated edges and spurs that are below the minimum length
2. *Line segmenting:* For each labeled edge
    (a) Create a virtual straight line by connecting the start and end points of labeled edge
    (b) Calculate the deviation (perpendicular distance to the virtual line) of each point on the labeled edge
    (c) Divide the virtual line in half at the point of maximum deviation if the maximum deviation is greater than a threshold $d_{allowed}$
    (d) Repeat above process until the maximum deviation of all the line segments is less than $d_{allowed}$
3. *Line merging:* For each line segment
    (a) Merge with another line segment if the maximum tolerated angle deviation between them and the maximum distance between their end points are within a limit

Figure B.1:

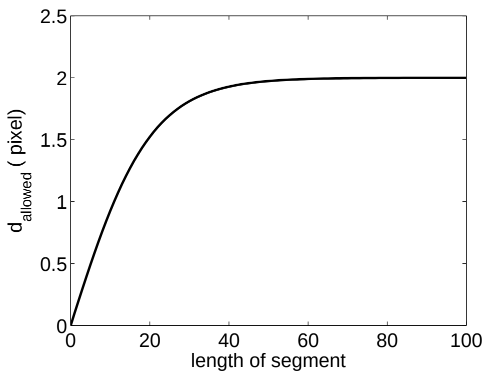

Figure B.2: The half-sigmoid function of $d_{allowed}$, which makes the threshold dependent upon the length of the segment. $\delta = 2$ and $\beta = 10$.

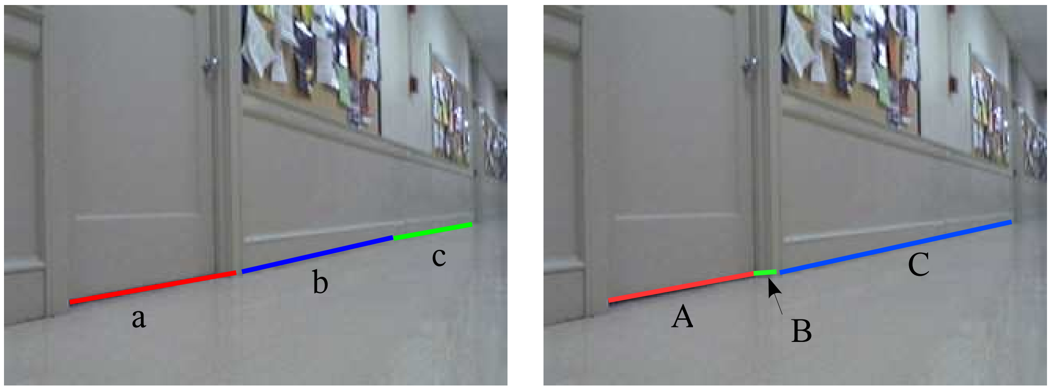

Figure B.3: Modified Douglas-Peucker algorithm. LEFT: The original algorithm mistakenly absorbs the door recession into segment `a`, and it mistakenly divides the single wall/floor line into `b` and `c`. RIGHT: With our modification, the recession is detected separately as segment `B`, and the segments `b` and `c` are correctly detected as a single segment `C`. Note that the recession segment `B` is important for the concavity test described in Section 5.3.6.

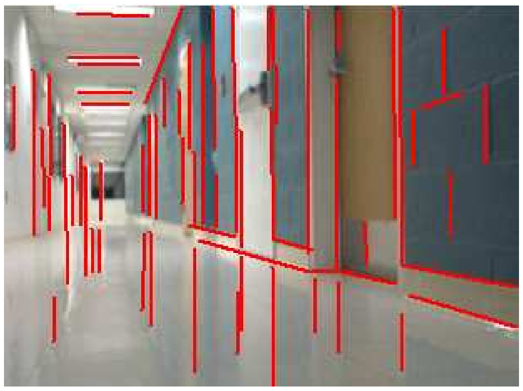
(a)

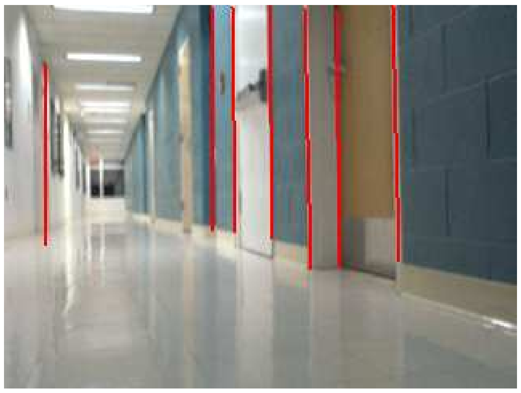
(b)

Figure B.4: Line segments and Candidate door. (a) Line segments detected by Canny edge detector followed by line detection. (b) Candidate door segments retained after applying multiple tests to the segments.

Bibliography

[1] OpenCV library, http://sourceforge.net/projects/opencvlibrary/files/.

[2] C. Ackerman and L. Itti. Robot steering with spectral image information. *IEEE Transactions on Robotics*, 21(2):247–251, Apr. 2005.

[3] G. Adorni, S. Cagnoni, M. Mordonini, and A. Sgorbissa. Omnidirectional stereo systems for robot navigation. In *Proceedings of the Fourth Workshop on Omnidirectional Vision (Omnivis)*, 2003.

[4] D. Anguelov, D. Koller, E. Parker, and S. Thrun. Detecting and modeling doors with mobile robots. In *Proceedings of the IEEE International Conference on Robotics and Automation*, 2004.

[5] G. C. Anousaki and K. J. Kyriakopoulos. Simultaneous localization and map building for mobile robot navigation. *IEEE Robotics and Automation Magazine*, 6(3):42–53, Sept. 1999.

[6] S. Atiya and G. D. Hager. Real-time vision-based robot localization. *IEEE Transactions on Robotics and Automation*, 9(6):785–799, Dec. 1993.

[7] S. Baker and I. Matthews. Optimal landmark configuration for vision-based control of mobile robots. *International Journal of Computer Vision*, 56(3):221–255, 2004.

[8] R. Barber, M. Mata, M. Boada, J. Armingol, and M. Salichs. A perception system based on laser information for mobile robot topologic navigation. In *The 28th Annual Conference of the IEEE Industrial Electronics Society*, 2002.

[9] R. Barnes. *Motion and time study: design and measurement of work*. John Wiley and Sons Inc, 7th edition, 1980.

[10] G. L. Barrows, J. S. Chahl, and M. V. Srinivasan. Biomimetic visual sensing and flight control. In *Bristol Conference on UAV Systems*, 2002.

[11] D. Beymer and K. Konolige. Tracking people from a mobile platform. *International Joint Conference on Artificial Intelligence*, 2001.

[12] S. Birchfield, 1997. KLT: An implementation of the Kanade-Lucas-Tomasi feature tracker, http://www.ces.clemson.edu/˜stb/klt/.

[13] S. T. Birchfield and S. J. Pundlik. Joint tracking of features and edges. *Proceedings of the IEEE Conference on Computer Vision and Pattern Recognition (CVPR)*, 2008.

[14] J. Borenstein, H. R. Everett, L. Feng, and D. Wehe. Mobile robot positioning: Sensors and techniques. *Journal of Robotic Systems*, 14(4):231–249, Apr. 1997.

[15] J.-Y. Bouguet. Pyramidal implementation of the Lucas Kanade feature tracker. OpenCV documentation, Intel Corporation, Microprocessor Research Labs, 1999.

[16] W. Burgard, A. B. Cremers, D. Fox, D. Hähnel, G. Lakemeyer, D. Schulz, W. Steiner, and S. Thrun. Experiences with an interactive museum guide-robot. *Artificial Intelligence*, 114(1-2):3–55, 1999.

[17] W. Burgard, D. Fox, D. Hennig, and T. Schmidt. Estimating the absolute position of a mobile robot using position probability grids. In *Proceedings of the National Conference on Artificial Intelligence*, 1996.

[18] D. Burschka and G. Hager. Vision-based control of mobile robots. In *Proceedings of the International Conference on Robotics and Automation*, pages 1707–1713, May 2001.

[19] D. Burschka and G. D. Hager. V-GPS (SLAM): Vision-based inertial system for mobile robots. In *Proceedings of the International Conference on Robotics and Automation*, pages 409–415, Apr. 2004.

[20] J. F. Canny. A computational approach to edge detection. *IEEE Transactions on Pattern Analysis and Machine Intelligence*, 8(6):679–698, 1986.

[21] B. Cartwright and T. Collett. Landmark maps for honeybees. *Biological Cybernetics*, 57(1).

[22] F. Chaumette and E. Malis. 2 1/2-D visual servoing: A possible solution to improve image-based and position-based visual servoings. In *Proceedings of the International Conference on Robotics and Automation*, pages 630–635, Apr. 2000.

[23] Z. Chen and S. T. Birchfield. Qualitative vision-based mobile robot navigation. In *Proceedings of the IEEE International Conference on Robotics and Automation (ICRA)*, pages 2686–2692, May 2006.

[24] Z. Chen and S. T. Birchfield. Visual detection of lintel-occluded doors from a single image. In *Workshop on Visual Localization for Mobile Platforms (in association with CVPR)*, June 2008.

[25] G. Cicirelli, T. D'Orazio, and A. Distante. Target recognition by components for mobile robot navigation. *Journal of Experimental & Theoretical Artificial Intelligence*, 15(3):281–297, 2003.

[26] S. Crawford, M. Cannon, D. Letourneau, P. Lepage, and F. Michaud. Performance evaluation of sensor combinations on mobile robots for automated platoon control. In *ION GNSS Conference*, pages 706–717, 2004.

[27] G. N. DeSouza and A. C. Kak. Vision for mobile robot navigation: A survey. *IEEE Transactions on Pattern Analysis and Machine Intelligence*, 24(2):237–267, Feb. 2002.

[28] D. Douglas and T. Peucker. Algorithms for the reduction of the number of points required to represent a digitized line or its caricature. *The Canadian Cartographer*, 10(2):112–122, 1973.

[29] E. Dubrofsky and R. J. Woodham. Combining line and point correspondences for homography estimation. *Proceedings of the 4th International Symposium on Advances in Visual Computing*, pages 202–213, 2008.

[30] J. M. Evans. HelpMate: An autonomous mobile robot courier for hospitals. In *Proceedings of the IEEE/RSJ International Conference on Intelligent Robots and Systems (IROS)*, pages 1695–1700, 1994.

[31] P. Felzenszwalb and D. Huttenlocher. Efficient graph-based image segmentation. *International Journal of Computer Vision*, 59(2):167–181, 2004.

[32] M. A. Fischler and R. C. Bolles. Random sample consensus: A paradigm for model fitting with applications to image analysis and automated cartography. *Communications of the ACM*, 24(6):381–395, 1981.

[33] Y. Freund and R. E. Schapire. A decision-theoretic generalization of on-line learning and an application to boosting. *Computational Learning Theory: Eurocolt*, pages 23–37, 1995.

[34] Y. Freund and R. E. Schapire. A short introduction to boosting. *Journal of Japanese Society for Artificial Intelligence*, 14(5):771–780, Sept. 1999.

[35] P. Fua. A parallel stereo algorithm that produces dense depth maps and preserves image features. *Machine Vision and Applications*, 6(1):35–49, 1993.

[36] A. S. G. Chivilò, F. Mezzaro and R. Zaccaria. Follow-the-leader behaviour through optical flow minimization. *IEEE International Conference on Intelligent Robots and Systems (IROS)*, 2004.

[37] P. Gaussier, C. Joulain, S. Zrehen, J. P. Banquet, and A. Revel. Visual navigation in an open environment without map. In *Proceedings of the IEEE/RSJ International Conference on Intelligent Robots and Systems (IROS)*, pages 545–550, Sept. 1997.

[38] C. Giovannangeli, P. Gaussier, and G. Désilles. Robust mapless outdoor vision-based navigation. In *Proceedings of the IEEE/RSJ International Conference on Intelligent Robots and Systems*, pages 3293–3300, 2006.

[39] J. J. Guerrero and C. Sagüés. Uncalibrated vision based on lines for robot navigation. *Mechatronics*, 11(6):759–777, 2001.

[40] C. G. Harris and M. Stephens. A combined corner and edge detector. In *Proceedings of the 4th Alvey Vision Conference*, pages 147–151, 1988.

[41] R. Hartley and A. Zisserman. *Multiple View Geometry in Computer Vision*. Cambridge University Press, second edition, 2003.

[42] J. Hensler, M. Blaich, and O. Bittel. Real-time door detection based on AdaBoost learning algorithm. In *International Conference on Research and Education in Robotics (Eurobot)*, 2009.

[43] I. D. Horswill. Polly: A vision-based artificial agent. In *Proceedings of the National Conference on Artificial Intelligence*, pages 824–829, 1993.

[44] S. Hutchinson, G. Hager, and P. Corke. A tutorial on visual servo control. *IEEE Transactions on Robotics and Automation*, 12(5):651–670, 1996.

[45] S. D. Jones, C. S. Andersen, and J. L. Crowley. Appearance based processes for visual navigation. In *Proceedings of the IEEE/RSJ International Conference on Intelligent Robots and Systems (IROS)*, pages 551–557, 1997.

[46] C. S. Kenney, M. Zuliani, and B. S. Manjunath. An axiomatic approach to corner detection. In *Proceedings of the IEEE Conference on Computer Vision and Pattern Recognition (CVPR)*, pages 191–197, 2005.

[47] D. Kim and R. Nevatia. A method for recognition and localization of generic objects for indoor navigation. In *ARPA Image Understanding Workshop*, 1994.

[48] J. Kittler, M. Hatef, R. Duin, and J. Matas. On combining classifiers. *IEEE Transactions on Pattern Analysis and Machine Intelligence*, 20(3):226–239, 1998.

[49] J. Kittler, A. Hojjatoleslami, and T. Windeatt. Weighting factors in multiple expert fusion. In *Proceedings of the Eighth British Machine Vision Conference*, 1997.

[50] A. Kosaka and A. C. Kak. Fast vision-guided mobile robot navigation using model-based reasoning and prediction of uncertainties. *CVGIP: Image Understanding*, 56(3):271–329, Nov. 1992.

[51] J. Košecká, L. Zhou, P. Barber, and Z. Duric. Qualitative image based localization in indoors environments. In *Proceedings of the IEEE Conference on Computer Vision and Pattern Recognition (CVPR)*, pages 3–8, 2003.

[52] D. J. Kriegman, E. Triendl, and T. O. Binford. Stereo vision and navigation within buildings for mobile robots. *IEEE Transactions on Robotics and Automation*, pages 792–803, 1989.

[53] B. Kröse, N. Vlassis, R. Bunschoten, and Y. Motomura. A probabilistic model for appearance-based robot localization. *Image and Vision Computing*, 19(6):381–391, 2001.

[54] E. Krotkov. Mobile robot localization using a single image. In *Proceedings of the IEEE International Conference on Robotics and Automation (ICRA)*, volume 2, pages 978–983, May 1989.

[55] H. Kwon, Y. Yoon, J. B. Park, and A. C. Kak. Person tracking with a mobile robot using two uncalibrated independently moving cameras. *Proceedings of IEEE International Conference on Robotics and Automation (ICRA)*, 2005.

[56] X. Lebegue and J. K. Aggarwal. Generation of architectural CAD models using a mobile robot. In *Proceedings of the International Conference on Robotics and Automation*, pages 711–717, 1994.

[57] Y. LeCun, U. Muller, J. Ben, E. Cosatto, and B. Flepp. Off-road obstacle avoidance through end-to-end learning. In *Advances in Neural Information Processing Systems (NIPS)*, pages 739–746, 2005.

[58] Y. Li and S. T. Birchfield. Image-based segmentation of indoor corridor floors for a mobile robot. In *Proceedings of the IEEE Conference on Intelligent Robots and Systems (IROS)*, 2010.

[59] B. Liang and N. Pears. Visual navigation using planar homographies. In *Proceedings of the International Conference on Robotics and Automation*, volume 1, pages 205–210, 2002.

[60] C. López-Franco and E. Bayro-Corrochano. Omnidirectional vision for visual landmark identification using p^2-invariants. In *Proceedings of the International Conference on Robotics and Automation*, pages 545–550, May 2006.

[61] B. D. Lucas and T. Kanade. An iterative image registration technique with an application to stereo vision. In *Proceedings of the 7th International Joint Conference on Artificial Intelligence*, pages 674–679, 1981.

[62] Y. Matsumoto, M. Inaba, and H. Inoue. Visual navigation using view-sequenced route representation. In *Proceedings of the International Conference on Robotics and Automation*, volume 1, pages 83–88, 1996.

[63] Y. Matsumoto, K. Sakai, M. Inaba, and H. Inoue. View-based approach to robot navigation. In *Proceedings of the IEEE/RSJ International Conference on Intelligent Robots and Systems (IROS)*, volume 3, pages 545–550, 2000.

[64] W. Meeussen, M. Wise, S. Glaser, S. Chitta, C. McGann, P. Mihelich, E. Marder-Eppstein, M. Muja, V. Eruhimov, T. Foote, J. Hsu, R. Rusu, B. Marthi, G. Bradski, K. Konolige, B. Gerkey, and E. Berger. Autonomous door opening and plugging in with a personal robot. In *IEEE International Conference on Robotics and Automation*, 2010.

[65] J. Michels, A. Saxena, and A. Y. Ng. High-speed obstacle avoidance using monocular vision and reinforcement learning. In *Proceedings of the Twenty-second International Conference on Machine Learning*, pages 593–600, 2005.

[66] T. Miyashita, M. Shiomi, and H. Ishiguro. Multisensor-based human tracking behaviors with Markov chain Monte Carlo methods. *Proceedings of IEEE-RAS/RSJ International Conference on Humanoid Robots*, 2004.

[67] I. Monasterio, E. Lazkano, I. Rano, and B. Sierra. Learning to traverse doors using visual information. *Mathematics and Computers in Simulation*, 60(3):347–356, Sept. 2002.

[68] R. Munoz-Salinas, E. Aguirre, M. Garcia-Silvente, and A. Gonzalez. Door-detection using computer vision and fuzzy logic. In *Proceedings of the 6th WSEAS International Conference on Mathematical Methods & Computational Techniques in Electrical Engineering*, 2004.

[69] V. N. Murali and S. T. Birchfield. Autonomous navigation and mapping using monocular low-resolution grayscale vision. In *Workshop on Visual Localization for Mobile Platforms (in association with CVPR)*, June 2008.

[70] S. K. Nayar, H. Murase, and S. A. Nene. Learning, positioning, and tracking visual appearance. In *Proceedings of the International Conference on Robotics and Automation*, pages 3237–3244, May 1994.

[71] S. Negahdaripour and C. H. Yu. A generalized brightness change model for computing optical flow. In *Proceedings of the International Conference on Computer Vision*, pages 2–11, 1993.

[72] R. C. Nelson and J. Aloimonos. Using flow field divergence for obstacle avoidance towards qualitative vision. In *Proceedings of the International Conference on Computer Vision*, pages 188–196, 1988.

[73] I. Nourbakhsh, R. Powers, and S. Birchfield. Dervish: an office navigating robot. *AI Magazine*, 16(2):53–60, 1995.

[74] I. Nourbakhsh, R. Powers, and S. Birchfield. Dervish: An office-navigating robot. *AI Magazine*, 16(2):53–60, 1995.

[75] M. Piaggio, P. Fornaro, A. Piombo, L. Sanna, and R. Zaccaria. An optical-flow person following behaviour. *Proceedings of the IEEE ISIC/CIRNISAS Joint Conference*, 1998.

[76] M. Rossetti, R. Felder, and A. Kumar.

[77] M. Rous, H. Lupschen, and K.-F. Kraiss. Vision-based indoor scene analysis for natural landmark detection. In *Proceedings of the IEEE International Conference on Robotics and Automation (ICRA)*, 2005.

[78] E. Royer, M. Lhuillier, M. Dhome, and J.-M. Lavest. Monocular vision for mobile robot localization and autonomous navigation. *International Journal of Computer Vision*, 74(3):237–260, 2007.

[79] C. Sagüés and J. J. Guerrero. Visual correction for mobile robot homing. *Robotics and Autonomous Systems*, 50(1):41–49, 2005.

[80] J. Santos-Victor, G. Sandini, F. Curotto, and S. Garibaldi. Divergent stereo in autonomous navigation: From bees to robots. *International Journal of Computer Vision*, 14(2):159–177, Mar. 1995.

[81] C. Schlegel, J. Illmann, M. S. H. Jaberg, and R. Worz. Vision based person tracking with a mobile robot. *The British Machine Vision Conference*, 1998.

[82] C. Schmid, R. Mohr, and C. Bauckhage. Evaluation of interest point detectors. *International Journal of Computer Vision*, 37(2):151–172, 2000.

[83] A. L. Shelton and J. D. E. Gabrieli. Neural correlates of encoding space from route and survey perspectives. *The Journal of Neuroscience*, 22(7):2711?2717, Apr. 2002.

[84] J. Shi and C. Tomasi. Good features to track. In *Proceedings of the IEEE Conference on Computer Vision and Pattern Recognition (CVPR)*, pages 593–600, 1994.

[85] Y. Shimizu and J. Sato. Visual navigation of uncalibrated mobile robots from uncalibrated stereo pointers. In *Proceedings of the IAPR International Conference on Pattern Recognition*, volume 1, pages 1346–1349, 2000.

[86] H. Sidenbladh, D. Kragik, and H. I. Christensen. A person following behaviour of a mobile robot. *Proceedings of IEEE International Conference on Robotics and Automation (ICRA)*, 1999.

[87] R. Sim and G. Dudek. Learning environmental features for pose estimation. *Image and Vision Computing*, 19(11):733–739, 2001.

[88] M. Sridharan and P.Stone. Color learning and illumination invariance on mobile robots: a survey. *Robotics and Autonomous Systems (RAS) Journal*, 57:629–644, 2009.

[89] S. A. Stoeter, F. L. Mauff, and N. P. Papanikolopoulos. Real-time door detection in cluttered environments. In *Proceedings of the 15th IEEE International Symposium on Intelligent Control*, 2000.

[90] M. Tarokh and P. Ferrari. Robotic person following using fuzzy control and image segmentation. *Journal of Robotic Systems*, 20(9):557–568, Sept. 2003.

[91] M. Tarokh and P. Ferrari. Robotic person following using fuzzy control and image segmentation. *Journal of Robotic Systems*, 20(9), 2003.

[92] D. M. J. Tax, M. van Breukelen, R. P. W. Duin, and J. Kittler. Combining multiple classifiers by averaging or multiplying? *Pattern Recognition*, 33:1475–1485, 2000.

[93] S. Thrun. Robotic mapping: A survey. In G. Lakemeyer and B. Nebel, editors, *Exploring Artificial Intelligence in the New Millenium*. Morgan Kaufmann, 2002.

[94] S. Thrun, D. Fox, and W. Burgard. A probabilistic approach to concurrent mapping and localization for mobile robots. *Machine Learning*, 31:29–53, 1998. also appeared in *Autonomous Robots*, 5, 253–271 (joint issue).

[95] C. Tomasi and T. Kanade. Detection and tracking of point features. Technical Report CMU-CS-91-132, Carnegie Mellon University, Apr. 1991.

[96] E. Trucco and A. Verri. *Introductory Techniques for 3D Computer Vision*. Upper Saddle River, NJ: Prentice Hall, 1998.

[97] I. Ulrich and I. Nourbakhsh. Appearance-based place recognition for topological localization. In *Proceedings of the International Conference on Robotics and Automation*, pages 1023–1029, May 2002.

[98] P. Viola and M. J. Jones. Robust real-time face detection. *International Journal of Computer Vision*, 57(2):137–154, 2004.

[99] J. Weng and S. Chen. Incremental learning for vision-based navigation. In *Proceedings of the IAPR International Conference on Pattern Recognition*, pages 45–49, 1996.

[100] J. Wolf, W. Burgard, and H. Burkhardt. Using an image retrieval system for vision-based mobile robot localization. In *Proceedings of the International Conference on Image and Video Retrieval (CIVR)*, pages 108–119, 2002.

[101] Z. Zhang and O. D. Faugeras. A 3D model builder with a mobile robot. *International Journal of Robotics*, 11(4):269–285, 1992.

[102] C. Zhou, Y. Wei, and T. Tan. Mobile robot self-localization based on global visual appearance features. In *Proceedings of the International Conference on Robotics and Automation*, pages 1271–1276, Sept. 2003.